Stony Brook
University

JUCER

Journal of Undergraduate Chemical Engineering Research
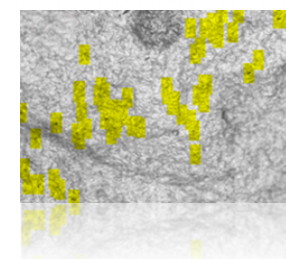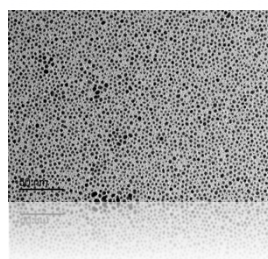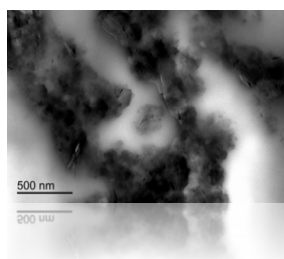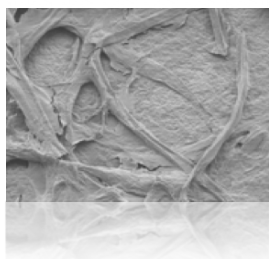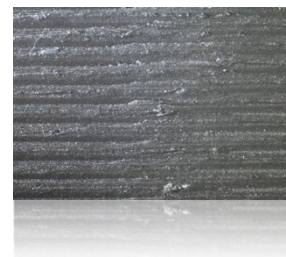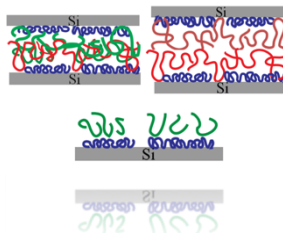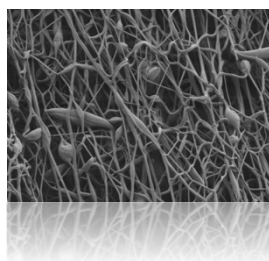
JUCER

Chemical&
Molecular
Engineering

AT STONY BROOK UNIVERSITY

Cover Art (*1st row/2nd row, left to right*):

SEM images captured using RBSD of PS with 0.15% surfactant at 1000x magnification (see page 46)

Model of PMP polymer adhesion and substrate surface diffusion diminishment effects (see page 21)

A half lumen composed of gelatin with a fibrin coating (see page 50)

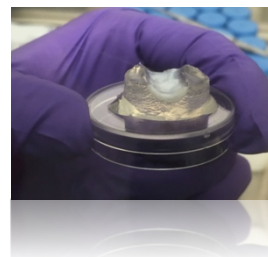Optical microscopy of 5 weight% parallel printed sample (see page 35)

SEM image of nitro-oxidized agave fibers suspended in 500 ppm of Pb water (see page 64)

TEM image of 20/80/15 EVA/PP/GNP blend (see page 40)

TEM image of Au-Ag nanoparticles (see page 13)

Light microscopy picture (100X) of collagenous membrane with pollution (see page 8)

Staff

Editors
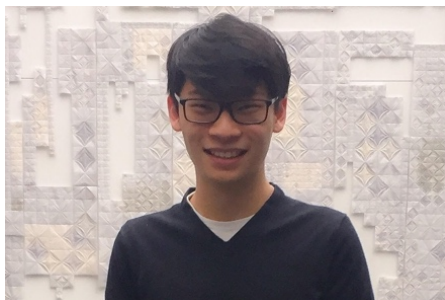
Jessica Hofflich	Justin Cheung	Jenna Mallon
Timothy Hart	Arthur Ronne	Arthur Rozario

Advisors

Miriam Rafailovich
Faculty Advisor

Yuval Shmueli
Graduate Advisor

A Letter From the Editors

We, the editorial board, are proud and honored to present the latest edition of the Journal of Undergraduate Chemical Engineering Research (JUCER). JUCER Volume VII represents a culmination of the work of all the graduating seniors in Stony Brooks Chemical and Molecular Engineering (CME) Program, Class of 2018. In this volume, you will find peer-reviewed articles which highlight the yearlong research conducted by all of the graduating CME students.

Since its conception, JUCER has strived to be a showcase of the breadth of chemical engineering research that can be achieved by undergraduate students. But, more importantly, it has been a tool of learning for all those involved. The authors of all the papers you will find below have been immersed in the scientific research process for the past year where they have learned skills and concepts that have extended beyond what is taught in the classroom. These authors have also undergone a rigorous peer review process where their work is scrutinized by experts in their field. As such, all those published in JUCER have gained leadership and communication skills that prepare them not only for future academic rigor but also the vast array of fields in which chemical engineers are employed.

From vascular grafts to polymer coatings and hydrogen fuel cells, the work that is showcased in JUCER Volume VII truly captures the breadth of chemical engineering in the 21st century. In many ways the diversity of the research published in this volume parallels the diversity of our graduating class. While united by our experiences as chemical engineers we all come from a wide array of backgrounds and will be pursuing a wide array of careers upon graduation, from finance to medicine to chemical industry. This is an illustration of the versatility of what it means to be a chemical engineer: the ability to adapt, problem solve, and apply skills to problems both within and beyond the traditional scope of chemical engineering.

We would like to extend our thanks to all of the students who have submitted their research for publication in JUCER and acknowledge the hard work that each author has put into the final article. Moreover we extend our gratitude and appreciation to Miriam Rafailovich and Yuval Shmueli, JUCERs faculty and graduate student advisors, respectively. The success of JUCER today would not be possible without their guidance. We are incredibly excited to now publicly showcase the work of the Stony Brook CME Class of 2018 and we wish them all the best. We are very proud that a publication in JUCER will be among their many future accomplishments.

Sincerely,

Jessica Hofflich, Justin Cheung, Jenna Mallon, Timothy Hart, Arthur Ronne, Arthur Rozario

Editors of JUCER

Table of Contents

In Vitro Characterization of the Mineral-Rich Magnetic Mud Mask

Olivia Holmes[a], Nina Zeng[a], Samantha Rosen[a], Tzu-Chi Kao[a], Anthony Salonia[a]

[a]*Department of Materials Science and Chemical Engineering, Stony Brook, NY 11794, USA*

Abstract

Modern research findings have connected skin exposure to air pollution with premature skin aging. The $SEACRET^{TM}$ Mineral-Rich Magnetic Mud Mask, is a cosmetic product currently focused on cleansing and improving the quality of the skin by the use of a colloid of oils, iron powder, and Dead Sea mud components. The mud mask should be applied to the surface of skin and magnetically removed after five minutes, resulting in facial skin rejuvenation. Product exploration began with characterization of the mask content including oil, iron powder, and minerals by X-ray Fluorescence, Fourier-Transform Infrared Spectroscopy, and Ultraviolet Spectroscopy. Further, to study the ability of the mud mask to remove ambient particulate matter of air pollution from skin, we collected particles from a car exhaust pipe and applied them on a lamb collagenous membrane as a skin model. To evaluate the efficiency of iron-based mask pollution removal after the completed procedure, particle counting and size identification on the skin model were quantified using ImageJ. The components of the mask remaining on the membranes led to an in vitro study of the effect on skin cells. Considering the possibility of components penetrating the skin, experimentation using extracted oils and iron powder in a water base was conducted on dermal fibroblasts and keratinocyte skin cells. Conclusively, the results found that the oil extracts with and without iron were able to sustain the cell environment of dermal fibroblasts and further support cell proliferation of keratinocytes. We propose that after application of the $SEACRET^{TM}$ Mineral-Rich Magnetic Mud Mask, existing air pollution particles will attach to the oil phase of the mask, due to their hydrophobic property, and will be removed magnetically along with the iron encapsulated in the oil of colloid.

Keywords: Pollution, Dead Sea Minerals, Cosmetic Mask

1. Introduction

In recent years, the connection between air pollution and premature aging has been intensively studied. Due to high levels of air contaminants around the world, particularly in Asia, cosmetic companies have been researching anti-pollution formulations. Air pollution is categorized into two types, primary and secondary pollution, where primary pollution consists of particulate matter (PM) and toxic gases. When primary pollutants react due to heat or UV radiation, secondary pollutants are formed [1].

Emissions from motor vehicles are one major source of concern for air pollution. The particulate matter emitted from motor vehicles, consisting of approximately 20% heavy metals and carbon-based materials, varies in size between 2.5 and 10 microns [2]. These metals, from greatest to least, include: calcium, iron, magnesium, zinc, chromium, nickel, lead, and barium [3]. For this reason, continuous urbanization has increased the demand for pollution removing cosmetic products. When metal pollutants encounter the skin, they can cause dryness, cellular damage, and pigmentation change, which indicate premature skin aging [4]. Skin pigmentation changes can include aggravation of acne as well [5]. Skin damage is caused by the ability of pollution to penetrate the skin [6]. Pollution removal is possible by washing with soap and water; however, the excessive use of soap can dry out skin because it is an astringent. Skin care products can aid in short-term skin health by forming a temporary shield against pollution. Research is ongoing for an anti-pollution cosmetic product that shields all types of skin. Varying skin type is a direct result of ethnicity differences, seasonal weather changes, differences in personal care, and so on [5].

The Mineral-Rich Magnetic Mud Mask from $SEACRET^{TM}$ is a colloid of oils, Dead Sea minerals, and iron listed with the following ingredients: propylene glycol, glycerin, dimethicone, isopropyl myristate, cyclomethicone, panthenol, capric triglyceride, grapeseed oil, jojoba seed oil, shea butter, fragrance, beeswax, phenoxyethanol, kaolin, rosehip oil, microcrystalline wax, vitamin E, and chamomile oil. The Mineral-Rich Magnetic Mud Mask claims to relax and rejuvenate the skin [7]. For centuries, Dead Sea minerals have been known for their therapeutic effects on human skin [8]. But, only a few cleansers currently on the market are capable of reducing pollution.

The use of existing magnetic mud masks, such as the Mineral-Rich Magnetic Mud Mask from $SEACRET^{TM}$, to remove pollution from facial skin have not been explored. Mechanistically, the mask is applied to facial skin in a thin layer and removed with a magnet after five minutes. The iron present in the mask allows for magnetic

removal. It is suggested to rub in the residue of oils left behind, allowing them to seep into the epidermis and dermis layers of the skin [8]. In this study, we demonstrate the successful removal of air pollution with the use of the $SEACRET^{TM}$ Mineral-Rich Magnetic Mud Mask. We propose a mode of action for the ability of applied colloid magnetic masks on polluted skin to dissolve the hydrophobic pollution particles by the lipid fraction. Pollutants are removed magnetically along with the iron-based mud masks.

2. Experimental

2.1. Materials

The Mineral-Rich Magnetic Mud Mask was obtained from SEACRETTM. The NaturaLamb collagenous membrane, manufactured by Church & Dwight Co., Inc., was used as a skin model. Car exhaust particles were collected directly from several tailpipes of cars to serve as model air pollution.

Primary keratinocyte and dermal fibroblast cell lines were supplied by the Skin Bank at the Dental School of Medicine (Isolated under IRB exemption 20076778). Keratinocytes were cultured in KGMTM-2 Growth Medium (Lonza). Fibroblasts were cultured in DMEM, 10% FBS, and Pen/Strep media (Gibco). $AlamarBlue^{TM}$ cell viability reagent was purchased from Thermo Fisher Scientific. Fine iron powder was acquired from Sigma Aldrich.

The X-ray Fluorescence (XRF) was detected using a Niton XL3t GOLDD+ handheld XRF from Thermo Scientific, for the pollution particles and mud mask on MYLAR thin 0.00024- 6.0 X-ray film.

The mud mask was analyzed using X-ray Diffraction (XRD) by the Philips Diffractometer with copper X-rays of 1.54184 .

2.2. Collagenous Membrane Treatment

To prepare the skin model, the collagenous membranes were stretched over 35 mm petri dishes and secured with Parafilm. The volume underneath was filled with DI water by a needle and syringe to maintain a damp construct. Air pollution was lightly patted onto the collagenous membrane surfaces. A thin layer of the mud mask was applied to all membranes and removed after five minutes using the magnet provided with the mask.

Images were taken of the collagenous membranes at 100x magnification before pollution, after pollution, and after application of the mud mask with an Olympus Light Microscope (BH2-UMA, f=180). Particle count and size identification were performed using ImageJ.

2.3. Keratinocyte and Dermal Fibroblast Cell Culture

A water-based extract of the mask was created in a 1:1 ratio of DI water: mud mask by vigorously mixing with a strong magnet for five minutes. Ultraviolet (UV) spectroscopy of the water-mask extract was obtained by the Thermo Scientific UV Spectrophotometer (Evolution 220).

The keratinocytes and dermal fibroblasts were plated on 96 well plates at a density of 104 cells/well, in their respective media, and incubated for 24 hours in a 37°C, 5% CO2 incubator. The water-mask extracts, with and without 1% iron powder, and DI water as a control, were applied to the cells in double dilutions from 10 to 160 times in media. The wells containing iron powder were incubated for five minutes before the iron was removed by a strong magnet and all the cells were incubated for another 24 hours. Afterwards, the media of each well was aspirated and replaced with 10% AlamarBlue in fresh media. After four hours of incubation in 37°C, 5% CO2 incubator, the BioTek microplate reader (FLx800; Excitation: 555 nm, Emission: 585 nm) was used to obtain optical density values of each well.

3. Results and Discussion

3.1. Pollution and Mask Characterization

Before applying the air pollution to collagenous membranes, they were examined by XRF. The elemental composition is presented in Table 1. The metals identified in our pollution model are comparable to the composition of car exhaust pollution determined by previous literature, including calcium, iron, zinc, and chromium [3].

Table 1: Elements Detected in the Collected Pollution Samples by XRF

Elements Found	Pollution (ppm)	Error (+/-)
Bal	932077	239
Fe	50120	239
Cr	4332	53
Ca	2766	215
W	249	30
Zn	188	7
Mn	131	41
Cu	79	8
V	54	28
Zr	49	2

To understand the content of the Mineral-Rich Magnetic Mud Mask, the elemental composition was tested by XRF. The most abundant element of the mask is iron, making up about 60% of the mud mask, as seen in Table 2, and is added to allow magnetic removal of the mud mask. All other metals identified are from the Dead Sea mud. Like the mud mask, the Jordan Dead Sea mud contains silicon in the greatest composition [9].

To identify the form of iron present in the mask, XRD testing was completed. It was concluded that the mud

Table 2: Elements Detected in the Mineral-Rich Magnetic Mud Mask by XRF

Elements Found	Pollution (ppm)	Error (+/-)
Fe	594768	6197
Bal	217548	7488
Si	177359	1708
P	5460	266
Co	2351	430
Ca	1529	303
Cr	230	58
Ba	217	90
S	188	64
V	127	60
Cu	98	50
Pb	64	28

mask contains pure iron rather than an ore of iron, such as the oxides magnetite and hematite. This is represented by the mud mask peaks, which occur at the iron ticks on the XRD spectra, as shown by Figure 1.
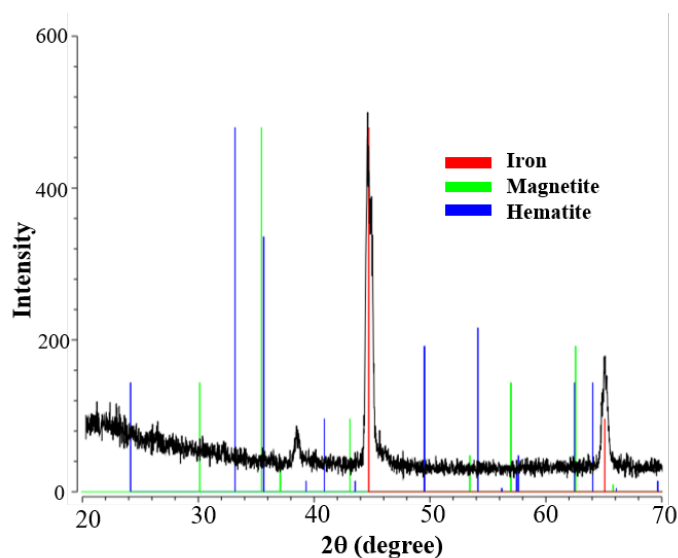
Figure 1: XRD Spectra of the Mineral-Rich Magnetic Mud Mask against Magnetite and Hematite Oxides

3.2. Pollution Removal Experiment

Collagenous membranes were used to study the efficiency of the mud mask to remove air pollution particles. Before pollution application, the original clean collagenous membrane did not contain particles, as seen by Figure 2(a). After the application of pollution, particles ranging from 5-50 micrometers (μm) in length were identified and are shown highlighted in yellow on Figure 2(b). Most of the pollution particles were 10-20 μm long, as shown by Figure 2(d). After proper application of the mud mask, the number of particles identified decreased, as shown by Figure 2(c). Pollution particles up to 50 μm in size were able to be removed.
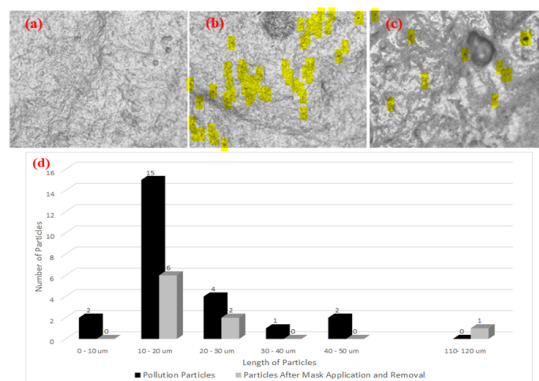
Figure 2: Light microscopy pictures (100X) of: (a) Clean Collagenous Membrane; (b) Collagenous Membrane with Pollution; (c) Collagenous Membrane after Mud Mask Application and Removal; (d) Number of Particles with Different Length Detected on Collagenous Membranes Measured by ImageJ

3.3. Effects of Mask on Keratinocyte and Dermal Fibroblast Cell Proliferation
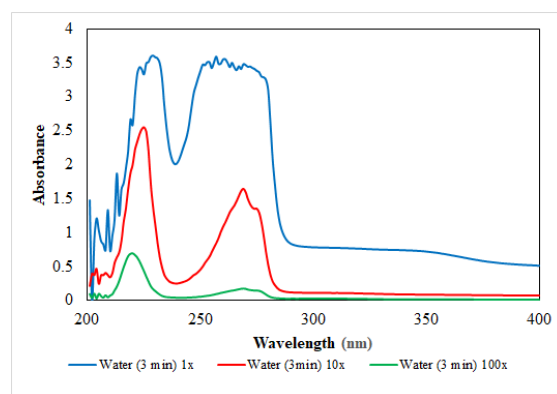
Figure 3: UV Spectra of Extract 1:1, Mud Mask: DI Water with 1x, 10x, and 100x Dilution

The experiment was done in triplicate and on average, the mud mask removed 65% of the air pollution particles originally identified. Of the 35% remaining, each trial contained one particle left behind that was greater than 50 m in length. These particles are most likely not part of the pollution applied because pollution particles this size were not detected before treatment with the mud mask. The particles could also be pollution particles encapsulated by lipids of the mud mask, making them appear larger, or a

component of the mud mask left behind, such as iron in the oils.
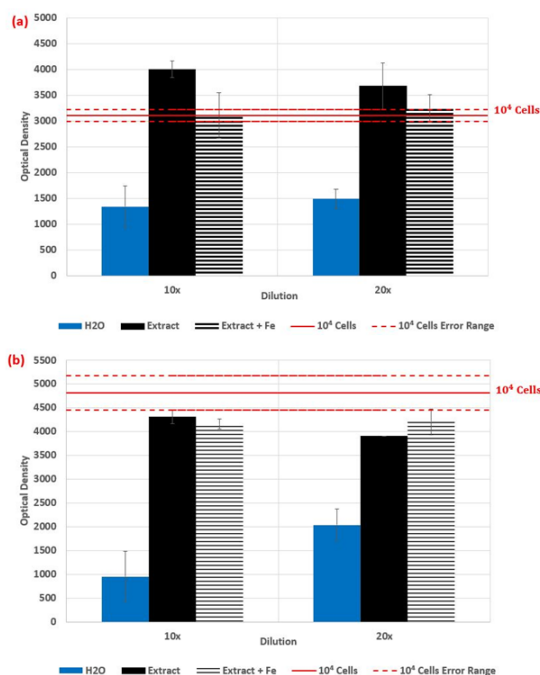
Figure 4: Cells Viability after Extract Application Measured as Optical Density (a) Keratinocytes and (b) Dermal Fibroblasts

Lipids are left behind after the removal of the mud mask with the magnet. To understand the effects of the lipids left behind by the mud mask, we tested the effect of the water-mask extracts on keratinocyte and dermal fibroblast cell proliferation. Because the mask cannot directly be applied on the cells, we began with the characterization of the water extracts of the mud mask using UV spectroscopy. The UV spectra, shown in Figure 3, has a large peak at approximately 220 nm and a smaller peak at roughly 270 nm. The large peak represents glycerol, one of the main ingredients of the mud mask [10]. The smaller peak was most likely caused by cera alba (beeswax), another ingredient the mask contains [11]. The UV spectra of the dilution shows oils of the product were successfully extracted.

Keratinocytes were chosen because the organics of the mask most likely have the greatest effect on the epidermis, the upper layer of the skin that is made up of keratinocyte cells. However, the lipids can penetrate through the keratinocytes to the dermis, made up of dermal fibroblast cells; consequently, we decided to treat these cells as well. To determine the toxicity of iron on the skin, if left behind, we also treated the cells with the water-mask extract with 1% iron powder added after extraction. The effects these water-mask extracts had on keratinocytes and dermal fibroblasts proliferation are shown in Figure 4(a) & (b).

As expected, the water control caused an inhibition of cell growth, due to the reduced osmotic pressure from the 10% diluted media with water, as shown in Figure 4(a) & (b). For comparison, the solid and dashed red lines represent cells plated at 104 and 0.5104 untreated in media, respectively. Treatment with the water-mask extracts stimulates the proliferation of keratinocytes, compared to untreated cells, as shown in Figure 4(a). Dermal fibroblasts that were treated with the water-mask extract and the extract with iron were able to maintain their viability at about 80-90%, as shown in Figure 4(b).

4. Conclusion

In this paper, we present a study on the Mineral-Rich Magnetic Mud Mask from $SEACRET^{TM}$. The capabilities of this mask, and masks of comparable composition, include the removal of air pollution and the support of keratinocytes and dermal fibroblasts cell proliferation by the organics remaining after product removal. The Mineral-Rich Magnetic Mud Mask was able to remove about 65% of pollution particles between 5-50 μm long, including the complete removal of particles less than 10 μm. We propose that the application of magnetic mud masks on polluted skin dissolves the hydrophobic pollution particles in the lipids within the five minutes of application. Then pollutants may be removed magnetically along with the iron-based mud mask. Minerals and oils deposited on the skin after the mud mask removal are contained in the water-mask extracts used to stimulate the keratinocytes proliferation. This suggests the capability of the mask to rejuvenate skin and improve dryness.

5. Acknowledgments

6. References

[1] M Portugal-Cohen, M Oron, D Cohen, and Z Maor. Antipollution skin protection- a new paradigm and its demonstration on two active compounds. *Clinical, Cosmetic and Investigational Dermatology*, 10:185 – 193, 2017.

[2] G Lough, J Schauer, J Park, M Shafer, J Deminter, and J Weinstein. Emissions of metals associated with motor vehicle roadways. *Environmental Science & Technology*, 39(3):826 – 836, 2005.

[3] K Bharathi, D Dwivedi, A Agarwal, and M Sharma. Diesel exhaust particulates characterization for heavy metals. *Indian Institute of Technology*, 16:1–4, 2004.

[4] P Puri, S Nandar, S Kathuria, and V Ramesh. Effects of air pollution on the skin: A review. *Indian J Dermatol Venereol Leprol*, 8(4):15–23, 2017.

[5] N Mistry. Guidelines for formulating anti-pollution products. *Cosmetics*, 4(4):57, 2017.

[6] M Portugal-Cohen, M Oron, D Cohen, and Z Ma'or. Antipollution skin protection a new paradigm and its demonstration on two active compounds. *Cosmetic, and Investigational Dermatology*, 10:185 – 193, 2017.

[7] Seacret: Dead sea skin care & best natural beauty products. *SEACRET: Dead Sea Skin Care & Best Natural Beauty Products*.

[8] F Levi-Schaffer, J Shani, Y Politi, E Rubinchik, and S Brenner. Inhibition of proliferation of psoriatic and healthy fibroblasts in cell culture by selected dead-sea salts. *Pharmacology*, 52:321 – 328, 1996.

[9] S Abdallah, S Ahmed, S Abayazeed, A El-Taher, and O Abd-Elkader. Quantitative elemental analysis and natural radioactivity levels of mud and salt collected from the dead sea, jordan. *Microchemical Journal*, 133:352 – 357, 2017.

[10] M Sohrabi, A Nouri, A Adnani, and H Masoumi. Determination of nonionic surfactant in liquid detergent by uv-vis spectrophotometry and multivariate calibration method. *Journal of Applied Sciences*, 7(1):148 –150, 2007.

[11] A Pan, S Chiussi, P Gonzalez, J Serra, and B Leon. Comparative evaluation of uvvisir nd:yag laser cleaning of beeswax layers on granite substrates. *Applied Surface Science*, 257(13):5484 5490, 2011.

JU$^{\text{U}}$CER

PEMFC Power Output Enhancement by Au-Ag Alloy Nanoparticle Membrane Coating

Dana Capitano[a], Nicole Cortes[a], Everett Hansen[a], Angela Kowaleski[a], James Puglisi[a], Ai Tai Zhen Wu[a], Lei Wang[a], Miriam Rafailovich[a]

[a]*Department of Materials Science and Chemical Engineering, Stony Brook, NY 11794, USA*

Abstract

Considering rising greenhouse gas emissions, a large-scale alternative to the internal combustion engine has become necessary to reduce further irreversible environmental damage. Polymer Electrolyte Membrane Fuel Cells (PEMFCs), which take advantage hydrogen oxidation electron transport, offer a promising alternative to traditional fossil fuel-burning engines as they produce only water as a byproduct. PEMFCs are not yet practical for commercial application due to inferior performance caused by operational cathode degradation. The current paper seeks investigate the improvement of PEMFC power output by applying a gold/silver alloy nanoparticle coating to the PEM to reduce membrane degradation by carbon monoxide catalyst poisoning. PEMFC power output was measured for PEMs coated with 2 nm 1:1 gold-silver alloy nanoparticles at varying coating surface pressures. When compared to an uncoated control cathode, Au-Ag coated membranes better resisted degradation, which enhanced PEMFC power output by 18% independent of nanoparticle concentration. When tested for carbon monoxide poisoning, coating the PEM in gold-silver alloy nanoparticles resulted in a 60% power increase over the control membrane under these catalyst poisoning conditions. The enhanced power output of Au-Ag coated PEMs suggests that more research should be performed to determine if these laboratory results are seen in full-scale application.

Keywords: PEMFC, hydrogen fuel cell, nanoparticles, gold, silver, alloy, power output, cathode degradation, polymer electrolyte membrane

1. Introduction

Every year, the average passenger vehicle outputs 4.6 metric tons of CO2, significantly contributing to worldwide environmental degradation [1]. To prevent increasing emissions, a global search for green energy solutions aims to find clean energy alternatives for future generations. One well-known alternative to the polluting combustion engine is the Proton Exchange Membrane Fuel Cell (PEMFC), commonly known as the hydrogen fuel cell.

PEMFCs convert chemical potential of gaseous hydrogen into electrical potential, producing only water and heat as byproducts. Furthermore, they may take advantage of current infrastructure utilized by their petroleum-based counterparts, since fuel cells also operate on an injected fuel. The versatility of this power source lends to their use in transportation and backup energy generation.

The PEMFC functions by taking in hydrogen gas and splitting the molecules into protons and electrons at the anode according to Reaction 1:

$$H_2 \rightarrow 2H^+ + 2e^- \tag{1}$$

The electrons travel through an external wire, creating electrical power. The protons are carried across a Polymer Electrolyte Membrane (PEM) situated between the

anode and cathode. When the proton crosses the PEM and reaches the cathode, a reaction occurs, described by Reaction 2, to create water as a byproduct:

$$\frac{1}{2}O_2 + 2H^+ + 2e^- \rightarrow H_2O \tag{2}$$
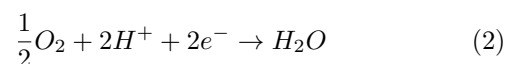
The electrodes consist of a porous carbon support with a thin layer of platinum. This platinum, known as the catalyst layer (CL), serves to catalyze both of the aforementioned reactions. With repeated use, these reactions slow down in the fuel cell as the CL degrades over time in the catalyst due to a variety of factors. Young, A. P. et al. note that PEMFCs are not yet commercially viable due to their cathode durability and, as a result, power output. PEMFC performance is diminished by CL cathode degradation, primarily because of the unzipping of weak links in Nafion polymer chains by hydroxyl radical, loss of CL effective surface area, and catalyst deactivation by unfiltered carbon monoxide [2, 3].

Carbon monoxide cathode poisoning is one of the most detrimental mechanisms by which the CL degrades. The CO adsorbs to the Pt active sites and blocks H_2 from accessing the catalyst [4]. Therefore, a carbon monoxide content of <20 ppm is preferable to guarantee stable fuel cell output [5]. Due to the traditional hydrogen synthesis method known as dry reforming, H_2 gas used in fuel cells

can contain small concentrations of CO and a significant amount of CO_2, which can be converted to CO during fuel cell operation by Reaction 3 [6, 7]:

$$H_2 + CO_2 \rightarrow H_2O + CO \qquad (3)$$
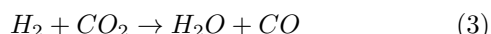
The cell performance can decrease even in CO concentrations as low as 2 ppm [8]. In order to meet fuel cell durability targets of 40,000 hours and 5,000 hours with less than a 10% performance loss for stationary and transportation applications, a solution is needed to mitigate these detrimental effects [9, 10].

Prior literature has shown CO in a hydrogen rich stream can be oxidized using gold alloys. Qwabe et al. studied this effect and concluded Au-Ni nanoparticle catalysts could convert 97% of CO in a hydrogen rich stream at 40°C [11]. Incorporating a gold-based alloy catalyst in the membrane electrode assembly (MEA) of the fuel cell therefore may assist in the prevention of cathode poisoning.

Furthermore, the addition of nanoparticle catalysts to coat the PEM has been proven to successfully increase fuel cell power output. In an experiment performed by Bennett, Adam et al., alloy nanoparticles of Au-Pd were coated on the surface of a Nafion 212 membrane to be incorporated into the MEA. This experiment showed this coating caused a 14% increase in power output [12]. Other research, solely focusing on the CO oxidation potential, concluded that 1:1 Au-Ag nanoparticles were shown to oxidize around 60% of CO in a 1% CO stream [13]. This shows promise in mitigating CL poisoning since when CO is oxidized, the resulting CO_2 does interfere with the Pt catalyst at the cathode.

This paper seeks to improve PEMFC power output by reducing cathode degradation, particularly by mitigating CO poisoning of the cathode using a Au-Ag nanoparticle coating on the PEM. Nanoparticles are applied to reduce the negative effects of CO by oxidizing it before its adsorption to the CL. We hypothesize this will improve PEMFC power output in the absence and presence of carbon monoxide.

2. Methodology

2.1. Chemicals and Materials

Toluene (99%), tetrachloroaurate (98-100%), tetraoctylammonium bromide (98%), dodecanethiol (98%), sodium borohydride (98.5%), and silver nitrate (99%) were purchased from Sigma Aldrich. Nafion 117 membranes and 0.1 mg/cm^2 Pt Loading Electrode Catalyst Paper were purchased from Fuel Cell Store. Hydrogen (>99.9%) gas cylinders were used for fuel cell testing.

2.2. Experimental Methods

2.2.1. Synthesis of Nanoparticles

The gold-silver nanoparticles were synthesized using a 1:1 ratio of both tetrachloroaurate ($HAuCl_4$) and silver nitrate ($AgNO_3$) as gold and silver precursors respectively. To make 0.6 mmol of silver-gold nanoparticles, 118.149 mg of $HAuCl_4$ and 50.961 mg of $AgNO_3$ were dissolved in a round bottom flask with 21.6 mL of deionized water. 1574.75 mg of Tetraoctylammonium bromide (TOABr) was dissolved into a beaker with 57.6 mL of toluene, and this solution was added to that containing the gold and silver precursors. This was stirred vigorously with a magnetic stirrer for 20 minutes until the solution separated into two layers. Then 120 L of dodecanethiol was added to that solution. 272.376 mg of Sodium Borohydride ($NaBH_4$) was dissolved in a separate beaker with 18 mL of deionized water. The solution was immediately mixed with the precursor solution (the sodium borohydride mix must be used immediately). This solution was covered with aluminum foil and mixed at room temperature for 3 hours with a magnetic stirrer. The solution separated into two layers: an aqueous layer and an organic layer. After the solution mixed, it was transferred into a separatory funnel to remove the aqueous layer and keep the organic one. The top (organic) layer was transferred into a different round bottom flask and subjected to a rotary evaporator until 5 mL of solution was left. 120 mL of ethanol was added to the remaining solution, and it was cooled at 4°C overnight, forming a black precipitate. Then the solution was transferred to 50 mL tube and centrifuged at 5,000 rpm for 10 minutes. The top solution was removed and 10 mL ethanol was added to wash the solution. It was centrifuged again for 10 min at 5,000 rpm. This centrifuging process was repeated 3 more times. Finally, the remaining solution was dried in a vacuum desiccator for 2 days.

2.2.2. Creating Au-Ag Solution

Approximately 1.0 mg of powdered Au-Ag nanoparticles was dissolved in a volume of liquid toluene in a ratio of 1 mg nanoparticles to 1 mL toluene. The solution was sonicated using the Branson 3510 sonicator for 30 minutes. The resulting solution had a maroon tint.

2.2.3. Coating Nafion 117

The Au-Ag solution was applied to Nafion 117 membrane with the aid of the Langmuir-Blodgett (LB) Trough. 150 L of the Au-Ag solution was dispensed to each side of the LB Trough with a microsyringe. The nanoparticles were dispensed close to the water surface to create a monolayer. 3 Nafion membranes coated with Au-Ag were made with different surface tensions: 2 mN/m, 5 mN/m and 8 mN/m.

2.2.4. Experimental Methods

The Nafion 117 membranes used in our experiments were coated with the previously synthesized nanoparticles

using a Langmuir-Blodgett (LB) trough run by KSB ResearchLab 3000 software.

The nanoparticle solution discussed in section 2.2.2 was sonicated for 30 minutes prior to use while the LB trough was cleaned and a water test performed. First, the LB trough basin was emptied of water. Once empty, both the trough and the barriers of the machinery are sprayed with ethanol then wiped dry with a paper towel. The arms were then replaced and trough filled with new distilled water.

Once the trough was prepared, the barriers were condensed and vacuum suction was used to remove any dirt on the surface of the water. The barriers were expanded, and then the water test was performed at a rate of 100 mm/min and a target surface tension of 1 mN/m. If the maximum surface tension is above 0.25 mN/m, the trough must be cleaned and refilled again, then another water test performed until the surface tension is less than 0.25 mN/m.

After a positive water test, the nanoparticles were placed into the trough. A 250 L microsyringe was used to disperse 150 L of nanoparticles to each side of the trough (for a total of 300 L for the whole trough). The syringe was gently placed as close to the surface of the water as possible, dropping only one drop at a time onto the water surface while moving the syringe to ensure an even spread of particles across the the trough. The particles are dropped very close to the surface because if they are dropped from a substantial height, they will sink below the surface and the membrane will not be coated. The nanoparticles were allowed to disperse over the water surface for 10 minutes.

Isothermal curves were obtained from the LB software, which provides information about the substances monolayer properties.

The Nafion 117 membrane was then dipped into the trough and held there. The barriers were then condensed at rate of 6 mm/min and a target surface tension was set for 5 mN/m for the first trial, 2 mN/m for the second, and 8 mN/m for the third. The target surface pressure was chosen as 5 mN/m because the TEM particle size analysis demonstrated a desirable size distribution. Surface pressure was also tested 3 mN/m above and below this target value to see if varying surface pressure would affect our results. Once the target surface pressure was reached, the membrane was raised from the trough. This coated a layer of nanoparticles onto the surface.

Once the coating was complete, the membrane was allowed to dry for several minutes before being transferred into a clean, labelled watch glass. The trough was then cleared, cleaned, and refilled again with distilled water.

2.2.5. Fuel Cell Testing Techniques

Once the membrane was coated, it was tested in the fuel cell demonstration kit. H_2 was flowed through the cell at approximately 78 ccm. The software BK 8600˙MDL was used to operate the kit. The current was adjusted from 0 to 0.7 Amps in intervals of 0.05 Amps every 30 seconds. This was repeated for a total of 4 trials for each membrane

tested. When testing the membrane for carbon monoxide poisoning, the same procedure described was used, with the only difference being that the gas stream used included 0.1% carbon monoxide in H_2.

3. Results and Discussion

3.1. Au-Ag Nanoparticle Characterization
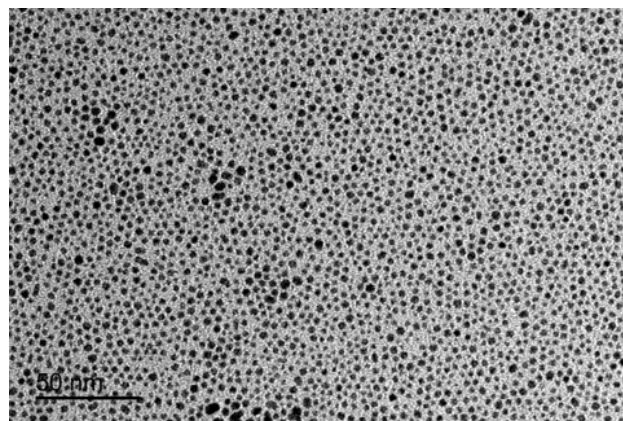
Figure 1: TEM image of Au-Ag nanoparticles. Surface pressure at 5 mN/m.

Figure 1 depicts TEM image of the Au-Ag alloy nanoparticles tested on the membranes. Figure 1 shows the particles dispersed with a surface pressure of 5 mN/m.
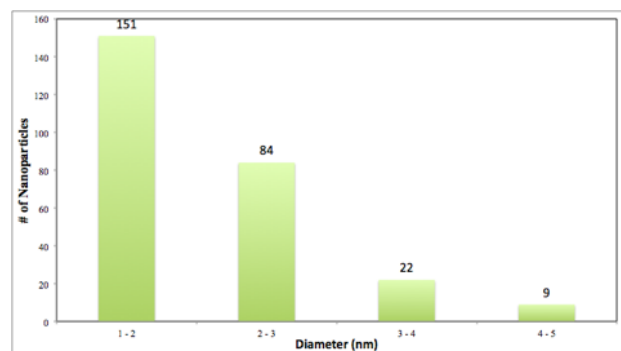
Figure 2: Particle Size Distribution of Au-Ag Nanoparticles.

The size distribution of the nanoparticles shown in Figure 1 was calculated using the software program ImageJ. The scale in the bottom left of Figure 1 was used for a pixel to nanometer conversion. This resulted in a scale of 4.48 pixels per nanometer. The feret diameter, an average of each particles maximum x and y distance were given for each particle the system counted. From this, the results in Figure 2 were obtained.

Using ImageJ, the nanoparticles obtained by our synthesis were determined to have an average diameter of 2.0 nm. The largest reached approximately 5.0 nm in diameter.

3.2. Au-Ag Nanoparticle Membrane

Table 1: Maximum power output of fuel cell tested with Au-Ag nanoparticle coating at different surface pressures

Au-Ag Catalyst (mN/m)	Max Power Output (Watts)
0 (control)	0.11
2	0.13
5	0.13
8	0.13

When tested using pure H_2 and open air as an oxygen source, the fuel cell had a higher power output when a Au-Ag coated membrane was used. Table 1 shows the maximum power output of the fuel cell when tested with the various coated membranes. The control data showed a maximum power output of 0.11 W, whereas the Au-Ag coated membrane peaked at 0.13 W for each PEM. This is about an 18% increase in power output.

The membranes tested were prepared via the LB trough with different surface pressures achieved in the nanoparticle layer. These surface pressures ranged from 2-8 mN/m. Nevertheless, these varied coating surface pressures all resulted in PEMs the same maximum power output. Therefore, the concentration of the nanoparticle catalyst on the membrane does not appear to proportionally correlate with PEMFC performance enhancement for the Au-Ag alloy. Figures 3 and 4 depict the polarization and power curves obtained from running the different membranes. It is clear from both graphs that regardless of the surface pressure, all three coated membranes performed about the same, and consistently performed better than the uncoated membrane.
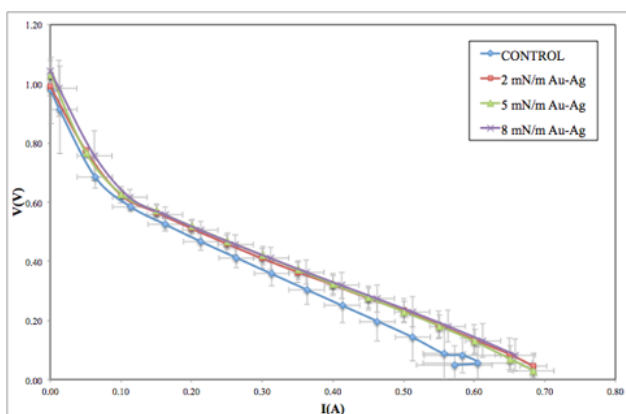
Figure 3: Power versus current from open-air tested Nafion 117 membrane and Au-Ag nanoparticle coated membranes. Pt catalyst loading of 0.1 mg/cm^2.

3.3. CO Testing

To test the Au-Ag coated membranes performance in the presence of CO, the fuel cell was operated using 0.1%
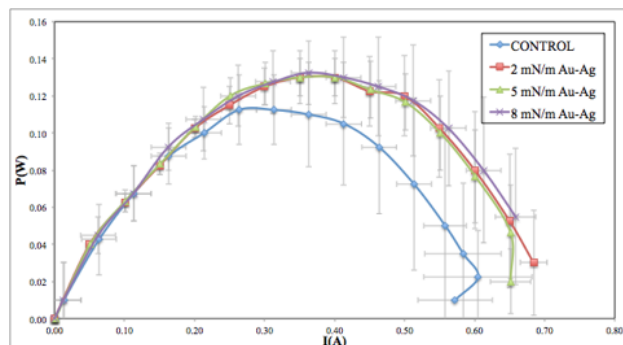
Figure 4: Polarization curves from open-air tested Nafion 117 membrane and Au-Ag nanoparticle coated membranes. Pt catalyst loading of 0.1 mg/cm^2.
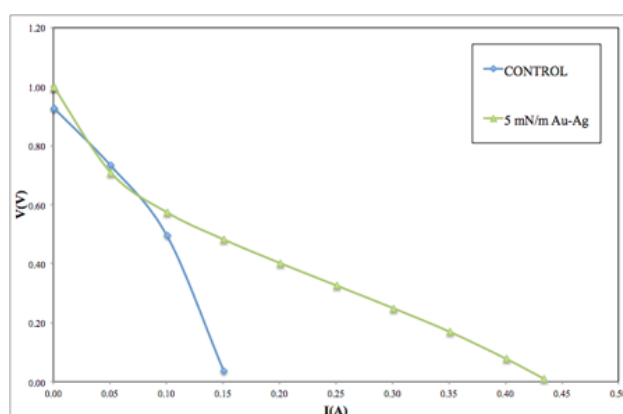
Figure 5: Polarization curves from tests with 0.1% CO in H_2.
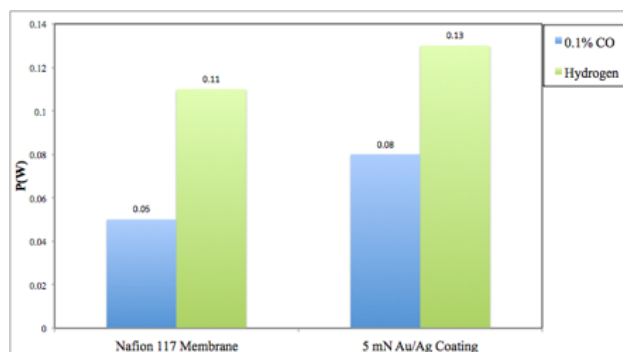
Figure 6: Maximum power output for both coated and uncoated membranes obtained from CO testing compared to pure H_2.

CO in H_2 instead of pure H_2. The results, shown in Figure 5, indicated that in the presence of CO, the PEMFC only reached a maximum power output of 0.5 W, an over 50% decrease in power output when compared to the pure hydrogen gas stream.

To mitigate this effect, a Au-Ag coated membrane with 5 mN/m of surface pressure was tested with the same CO concentration. The results of this trial indicated a 60% maximum power increase when compared to the uncoated

control membrane, reaching a maximum power output of 0.8 W.

Figure 6 shows that the power output of the fuel cell dramatically decreased when carbon monoxide was introduced to the system, regardless of which membrane was used. But with the presence of the Au-Ag nanoparticles on the membrane, the power output improved both with and without CO present when compared to a cell without these nanoparticles present.

4. Conclusion

Because of rising greenhouse gas emissions, a societal conversion to fossil fuel alternatives is becoming necessary to slow down irreversible environmental degradation. PEMFCs offer a promising alternative to traditional petroleum-burning engines, utilizing hydrogen oxidation electron transport only producing water as a byproduct. In order for hydrogen fuel cells to be commercially successful, fuel cell operation cost must be reduced. The current factors prohibiting cost-effective hydrogen fuel cell operation are cell durability and, as a result, power output. PEMFC performance is limited by platinum cathode degradation, primarily caused by formed hydroxyl radical attacks on weak links in Nafion polymer chains, loss of platinum effective surface area, and catalyst deactivation by unfiltered carbon monoxide from hydrogen gas formation [2, 3]. The current paper sought to evaluate the efficacy of a Au-Ag alloy nanoparticle membrane coating in augmenting PEMFC power output by diminishing these negative degradative effects.

The findings of this paper indicate that 1:1 Au-Ag alloy nanoparticles successfully improved PEMFC power output. The Au-Ag catalyst used to coat the PEM had an average size of 2 nm. The data collected by demonstration kit trials indicates that PEMs coated in Au-Ag alloy nanoparticles increased fuel cell maximum power output by 18% using 0.1 mg/cm^2 Pt-loaded cathode. This improvement was found to be independent of coating surface pressure for 2-8 mN/m. While this does confirm the hypothesis that adding these nanoparticles would help catalyze the reaction, it was expected that an increase in nanoparticle concentration would correspond to a higher maximum power output. In testing for carbon monoxide CL poisoning, membrane coating with Au-Ag alloy nanoparticles with a surface pressure of 5 mN/m caused a 60% maximum power increase over the control membrane under these conditions.

With respect to previous studies, the results of the current paper seem consistent with Trogadas, Panagiotis et al., which exhibited significantly reduced Nafion membrane degradation by gold and silver nanoparticle membrane coating [3]. Future studies could be performed to determine if greater improvement can be achieved at higher nanoparticle concentrations. Additionally, further research should investigate whether the enhanced power

output of Au-Ag coated PEMs is reproducible in full-scale fuel cell application.

5. Acknowledgments

6. References

[1] United States Environmental Protection Agency. *Greenhouse Gas Emissions from a Typical Passenger Vehicle*, 2018.

[2] A. P. Young, J. Stumper, and E. Gyenge. Characterizing the Structural Degradation in a PEMFC Cathode Catalyst Layer: Carbon Corrosion. *Journal of The Electrochemical Society*, 156(8):B913 − B922, 2009.

[3] Panagiotis Trogadas, Javier Parrondo, Federico Mijangos, and Vijay Ramani. Degradation mitigation in PEM fuel cells using metal nanoparticle additives. *Journal of Materials Chemistry*, 21(48):19381, 2011.

[4] Shengsheng Zhang, Xiao-Zi Yuan, Jason Ng Cheng Hin, Haijiang Wang, K. Andreas Friedrich, and Mathias Schulze. A review of platinum-based catalyst layer degradation in proton exchange membrane fuel cells. *Journal of Power Sources*, 194(2):588 − 600, 2009.

[5] Titilayo Shodiya, Oliver Schmidt, Wen Peng, and Nico Hotz. Novel nano-scale Au/α-Fe2O3 catalyst for the preferential oxidation of CO in biofuel reformate gas. *Journal of Catalysis*, 300:63 − 69, 2013.

[6] Gaby Janssen and N P Lebedva. Carbon dioxide poisoning on proton-exchange-membrane fuel cell anodes.

[7] Qingfeng Li, Ronghuan He, Ji-An Gao, Jens Oluf Jensen, and Niels. J. Bjerrum. The CO Poisoning Effect in PEMFCs Operational at Temperatures up to 200°C. *Journal of The Electrochemical Society*, 150(12):A1599 − A1605, 2003.

[8] International Journal of Energy Research. *International Journal of Energy Research*, 25(8):695713.

[9] United States Office of Energy Efficiency & Renewable Energy. *Fuel Cells*, 2018.

[10] United States Department of Energy. *Fuel Cell Technical Team Roadmap*, 2013.

[11] Lindelani Q. Qwabe, Venkata D.b.c. Dasireddy, Sooboo Singh, and Holger B. Friedrich. Preferential CO oxidation in a hydrogen-rich stream over gold supported on NiFe mixed metal oxides for fuel cell applications. *International Journal of Hydrogen Energy*, 41(4):2144 − 2153, 2016.

[12] Adam Bennett, Helen Liu, Allen Tran, Likun Wang, and Miriam Rafailovich. Synthesis and Characterization of Gold-Palladium Nanoparticles Catalyst For Improved Hydrogen Fuel Cell Performance. *Journal of Undergraduate Chemical Engineering Research*, 6:92 − 101.

[13] Jun-Hong Liu, Ai-Qin Wang, Yu-Shan Chi, Hong-Ping Lin, and Chung-Yuan Mou. Synergistic Effect in an AuAg Alloy Nanocatalyst: CO Oxidation. *The Journal of Physical Chemistry B*, 109(1):40 − 43, 2005.

JUCER

Nanoconfined Polymethylpentene Thin Films: A Model for Interpolymer Adhesion and Substrate Polymer Interactions

Justin Cheung[a], Pablo Henriquez[a], Jessica Hofflich[a], Jian Huang[a], Nafiul Jami[a], Yuma Morimitsu[a], Maya K. Endoh[a], Tadanori Koga[a]

[a]Department of Materials Science and Chemical Engineering, Stony Brook, NY 11794, USA

Abstract

Polymer thin films play a crucial role in adhesive materials as well as protective industrial coatings. One of the great challenges in developing industrially applicable polymer film coatings has been the issue of understanding their macroscopic behavior on solid substrates. In particular, polymethylpentene (PMP) has been reported for its lightweight nature and high resistance to heat and chemical exposure. We chose to utilize PMP thin films as a model to understand the mechanism and role of crystallinity in inter-polymer film adhesion, an important industrial property. It was found that there exists a physisorbed polymer layer of several nanometers thickness (adsorbed nanolayer) at the polymer-substrate interface. We adopted a strategy to study the role of the nanoconfined polymer chains in the adsorbed nanolayer. As a first step, we isolated and characterized the polymer chains at the substrate surface using atomic force microscopy and wide angle X-ray scattering. PMP samples were prepared by spin casting and then annealed at 150°C (Tg = 90°C). The films were then leached with chloroform to unveil the adsorbed chains. The adhesive properties of these adsorbed layers were tested via a custom-built adhesion test device. We prepared bulk PMP film samples of 200 nm thickness atop an adsorbed nanolayer to determine the layers role in adhesion. As a control, we also prepared bulk 200 nm thick PMP films which were pressed against one another instead of an adsorbed layer. Interestingly, a weak adhesion strength of 154 Pa was measured for the control sample, but there was no measurable film adhesion strength detected for the adsorbed layer sample. We hypothesized that the lack of adhesion at the adsorbed layer surface was due to substrate surface effects minimizing polymer chain diffusion, while the minimal bulk adhesion was due to the crystalline structure of the PMP. As a comparison, a series of similar experiments were conducted using poly(ethylene oxide), another crystalline polymer. We have demonstrated that it is the reptation of polymer chains across an interface that yields adhesive properties and that crystalline polymers do not heal easily unless their crystalline structure has been broken. This is a finding which provides important insight into the viability of polymer film adhesives and expands on the mechanistic understanding of nanoscale polymer behavior.

Keywords: Polymer Thin Films, Substrate-Polymer Interactions, Polymer Film Adhesion

1. Introduction

Owing to their unique properties when confined at the nanoscale, polymer thin films have grown in prominence in recent decades for their applicability in a variety of fields ranging from medical device coatings [1] to drug delivery [2]. The rising potential for novel and more durable technologies that is offered by the production and implementation of polymer thin films on an industrial scale has made them of particular interest to researchers. Specifically, the versatility of polymer thin films as industrial level coatings for a wide array of applications underscores the importance of being able to control and tailor their properties and behavior on a nanoscale level.

In particular, the adhesivity of polymer thin films is a key element in a polymers industrial applicability [3]. As such, our group was interested in characterizing and understanding the mechanism of adhesion of polymer thin films on solid supported substrates. To explore this topic, we

have chosen to use polymethylpentene (PMP) thin films on silicon wafer substrates as our model system. Mitsui Chemicals has recently developed the novel PMP polymer, brand named TPX. PMP has been found to have a wide array of very promising properties such as high heat tolerance (melting point, Tm = 240°C) and resistance to a variety of both inorganic and organic chemicals [4]. These properties make PMP a robust candidate for use in industrial coatings.

Historically, polymer thin films have been defined as having a thickness of less than 100 nm and can be characterized by the differing of their physical properties compared to their bulk counterparts [5]. In the case of solid-supported polymer thin films, the role of the substrate surface on the physical characteristics of the film has been well characterized. For instance in 1997, Zheng and coworkers demonstrated that the propagation of substrate surface effects in polymer thin films results in greatly diminished

chain diffusion and mobility near the substrate surface [6]. In 2012, Gin and coworkers described the presence of an adsorbed layer of polymer in solid supported, thermally annealed polymer thin films as shown in Fig. 1. The formation of these irreversibly adsorbed polymer chains was driven by the total enthalpic loss of the polymer chain adsorption onto the silicon substrate outweighing the loss of entropy of that same action [7].
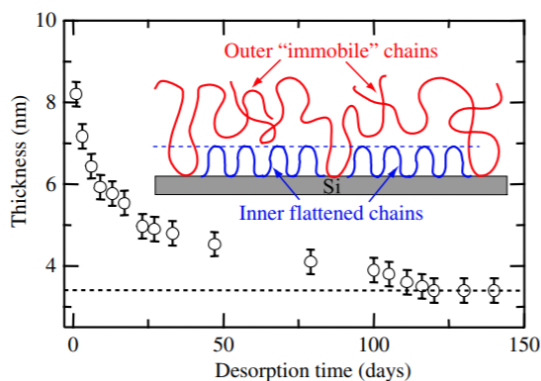

Figure 1: Adsorbed polymer layer on solid substrate [7].

It has been reported by a number of both experimental and computational groups that the interfacial region between polymer and substrate plays a crucial role in governing the adhesion behavior of polymer films, largely as a result of chain dynamics and behavior in highly confined nano-environments [8–10]. More recently, Jiang and coworkers have outlined a framework where they demonstrate the critical role the substrate adsorbed polymer layer plays in ensuring film stability [11]. This work, in particular, has shown that the entanglement between adsorbed polymer chains and the free polymer chains above them are crucial for ensuring the stability of a bulk polymer film on a solid substrate. These same interactions between substrate bound polymer and free polymer above it have also been shown have been shown to play critical roles in interpolymer film adhesion as well [12].

The existing literature in the field strongly indicates the importance that both solid substrate properties and polymer crystallinity play in governing the adhesive properties of a polymer thin film. If polymer thin films are to be applied more widely as industrial coatings, these are facets of thin film adhesion that must be further investigated and characterized. Thus, it is the goal of this investigation to take this a step further and extend on previous research by utilizing PMP as a model system to: (a) characterize and study the PMP adsorbed layer, (b) determining the role of polymer crystallinity on the adhesive properties of PMP thin films, and (c) compare the adhesive behavior of PMP thin films with a similar semi-crystalline polymer system, such as poly(ethylene oxide) (PEO), in order to gain insight into the overarching parameters which affect polymer thin film adhesion.

We hypothesize that the crystallinity of PMP may diminish its adhesive properties. Furthermore, we believe that the adsorbed PMP layer may have little to no adhesion with a bulk film owing to diminished chain mobility near the substrate surface.

This hypothesis was supported by several experiments which will be outlined later in this paper: (1) adhesion experiments that demonstrate PMP adsorbed films non-adhesivity, (2) adhesion experiments which demonstrate PMP bulk films non-adhesivity under thermal annealing conditions below the melting point, and (3) usage of a comparative PEO system which validated that breaking the polymer crystal structure through thermal annealing is sufficient to induce polymer thin film adhesion at the polymer-polymer interface. To further facilitate the translation of polymer thin films into industrial applications, it is imperative to thoroughly characterize the adhesive properties of the films themselves and to elucidate the mechanisms for their behavior. The results of this study will help shed light on thin film adhesion through this PMP model system.

2. Experimental

As described in the introduction, in order to study the structures of the irreversibly adsorbed polymer nanolayers of PMP and determine their role in PMP film adhesion, it was necessary to first isolate these adsorbed layers. To do so, we used a Guiselin brush approach as has been outlined by Gin and coworkers [7]. Silicon substrate wafers (UniversityWafer) were cleaned in a piranha solution (hydrogen peroxide and sulfuric acid were obtained from BDH Chemicals) and subsequently treated with hydrofluoric acid (HF) (BDH Chemicals) to remove the native oxide layer. Next, chloroform dissolved PMP (Mw = 514,000 Da, Crystallinity = 37 %, Mitsui Chemicals) was spin-cast on top of the substrate surface at an initial thickness 50 nm. The spin-cast PMP thin film was thermally annealed in an ultra-high vacuum oven at 150°C for 48 hours to allow for the formation of the irreversibly adsorbed layer. This is a temperature far above the glass transition (Tg = 90°C) of PMP but below the melting point (Tm = 240°C). Due to technical constraints it was not possible to anneal the samples under vacuum at a higher temperature than what was used. Subsequently, the PMP film was leached in chloroform (BDH Chemicals), a strong solvent for PMP, at 60°C until the film thickness no longer decreased. This was done in order to strip away the bulk film and leave behind only the residual irreversibly adsorbed chains. The film was then annealed for another 24 hours to remove any remaining solvent molecules. This process is illustrated in Fig. 3a. It should be noted that all measurements of film thickness were made using an ellipsometer.

In order to characterize the isolated PMP adsorbed layers, atomic force microscopy (AFM) imaging (Agilent 5500, Bruker Bioscope Catalyst and Digital Nanoscope III)

was used to obtain an understanding of the features of the surface structure of the PMP adsorbed layers and the bulk film. Understanding the specific surface architectures of the irreversibly adsorbed polymer layer allowed us to draw hypotheses on the specific parameters of the adsorbed layer (i.e. roughness, homogeneity) which may have a governing influence on the PMP films adhesive properties. Furthermore, to characterize the crystallinity of the bulk and adsorbed films of PMP, wide angle X-ray scattering (WAXS) was used and conducted at the National Synchrotron Light Source II (NSLS II) at Brookhaven National Laboratory.

To quantitatively measure the adhesion between two PMP thin films or between a PMP thin film and the adsorbed layer, a custom-made thin film adhesion testing device, shown in Fig. 2, was developed. PMP films were sandwiched on top of one another and annealed for 48 hours at 150°C with a 1 kg metal weight compressing the sandwich. After this compression process, the sandwiched films were attached at the interface between the spring and the bottom arm of the caliper (Mitsutoyo, with 0.02 mm accuracy) using glue (Loctite Super Glue, Henkel Corporation). This allowed for the sandwiched polymer sample to be anchored in place on the adhesion testing device with the spring firmly attached to it. As the caliper was pulled open, the spring would extend and apply a constant stress on the sandwiched sample until fracture occurred. Using Hookes Law (F = kx), where both the caliper displacement (x) as well as the spring constant (k) are known, the total stress required to break apart two films was calculated, allowing us to directly measure thin film adhesion via fracture stress. We used this device to test adhesion between bulk and adsorbed PMP films.
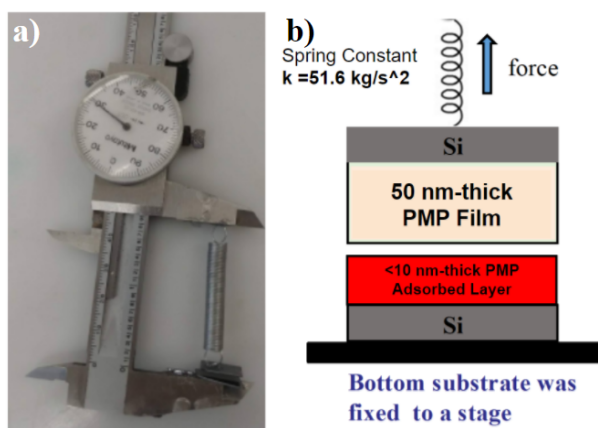

Figure 2: (a) Custom built adhesion testing device, (b) Proposed experiment to measure adhesive properties of the PMP adsorbed layer.

In an attempt to break the crystalline structure of the PMP films, additional PMP sandwiches were prepared and annealed at 290°C (T >>Tg and Tm) using a non-vacuum ceramic oven (Thermolyne Furnace). However, annealing times were no greater than 1 hour to prevent polymer oxidation degradation at such high temperatures. The sandwiched films adhesion under this condition was tested using the same apparatus.

Lastly, the crystallinity of PMP is 37 % according to WAXS experiments done by Mitsui Chemicals. To provide a standard of comparison with another crystalline polymer system, a similar set of adhesion experiments was conducted using poly(ethylene oxide) (PEO) of Mw = 100,000 Da (Sigma-Aldrich). Specifically, PEO sandwiches were annealed under two conditions: (1) at a temperature greater than Tg but below Tm as in the case of the PMP experiments and (2) at a temperature greater than both Tg and Tm . This was done in order to demonstrate the role of polymer crystallinity in influencing PMP thin film adhesion.

3. Results

3.1. Characterization of PMP Bulk and Adsorbed Layer Properties

As described in Fig. 3a, PMP adsorbed layers were fabricated through an annealing - solvent leaching, twostep process. AFM images were taken of both the initial 50 nm thick PMP film (bulk) and the final adsorbed layer of the PMP film after the chloroform leaching process (final thickness: 2.1 nm). Thicknesses of the bulk and adsorbed layers were measured using ellipsometry.

As is evident from the AFM data in Fig. 3b, the bulk PMP film prior to leaching had an inhomogeneous surface with height fluctuations >4 nm in some regions, likely due to the PMPs crystallinity. Interestingly, the surface of the adsorbed PMP nanolayer (post-leaching) had an extremely homogeneous surface with height fluctuations mostly less than 1 nm (Fig. 3c). WAXS experiments were conducted to verify the crystallinity of both the bulk and nanolayer PMP films, as shown below in Fig. 4. It was found that the bulk PMP exhibited significant crystalline properties as is evident from the Bragg peaks in Fig. 4A and from the scattering profile in Fig. 4B whereas the PMP nanolayer exhibited distinctly amorphous properties seen in Fig. 4C.

3.2. Adhesion Testing of PMP Films

Adhesion testing was conducted between sandwiched PMP thin films using the method outlined in Fig. 2. The fracture stress was calculated for each of the film sandwich combinations.

From the series of trials that were conducted, there are two noteworthy findings. Firstly, there was no measurable adhesion seen in the compressed sandwiches between bulk film and the adsorbed layer (Table 1, Column 1). In order to mimic the adsorbed layer conditions with a spin-cast film, we prepared a 5 nm spin-cast film (without leaching) and found that there was also no adhesion under this condition as well (Table 1, Column 2). Secondly, adhesion was only detected in the bulk films under the condition where two, 200 nm thick PMP films were compressed (Table 1,
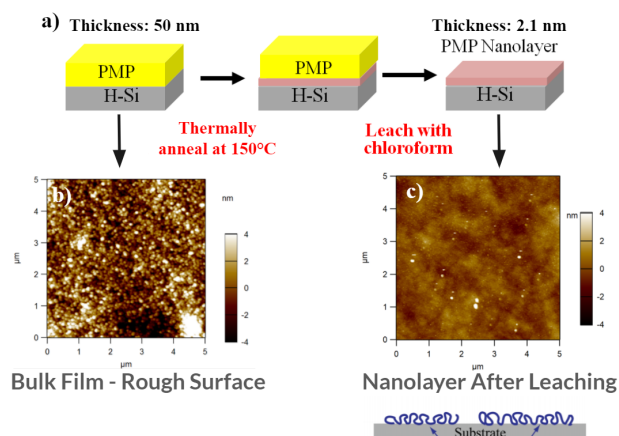
Figure 3: (a) Schema of process to selectively isolate the adsorbed PMP chains at the substrate surface. (b) AFM image of bulk 50 nm thick PMP film shows an inhomogeneous surface structure. (c) AFM image of adsorbed PMP chains at the substrate surface after chloroform leaching shows a very smooth surface structure.

Figure 4: (a) Graph of I (q) vs. q obtained from WAXS on bulk and nanolayer PMP. (b) Scattering profile of the bulk PMP film indicates crystalline structure. (c) Scattering profile of the PMP nanolayer indicates amorphous structure.

Column 6). And even then, the adhesion was relatively weak (¡ 1 kPa) as compared to typical polymer film adhesions reported in the literature [12]. Any bulk films of lesser thickness exhibited no adhesion whatsoever. Furthermore, it was verified that all fractures listed in Table 1 occurred at the polymer polymer interface since ellipsometry on post-adhesion experiment samples showed no change in the overall thickness of either of the two sandwiched films.

Subsequently, AFM images were taken of the bulk PMP 200 nm thick film after the adhesion experiment to characterize the films post-fracture surface structure (Fig. 5).

In the post fracture image (Fig. 5, right) there is evidence of diminished crystallinity as compared to the pre-adhesion film (Fig. 5, left). This suggests that breaking the polymer crystal structure is necessary to achieve a measurable degree of adhesion. As a control experiment, AFM images were taken of the surface of the PMP adsorbed layer before and after the adhesion experiment (data not shown). It was found that there were no significant surface morphology changes in the PMP adsorbed layer before and after the adhesion experiment. Given that the PMP adsorbed layer exhibits no adhesion whatsoever, this control experiment serves to verify that the surface morphology change in Fig. 5 is not an artifact of the adhesion test compression, but rather is due to actual adhesion at the polymer-polymer interface.

One of the primary reasons that there was no measurable degree of adhesion between PMP films below 200 nm in thickness may be due to the annealing temperature. The sandwiched films were annealed at 150°C which is above the glass transition temperature of PMP (90°C) but below the melting point (240°C). As a result, it is unlikely that the used annealing temperature was sufficient to
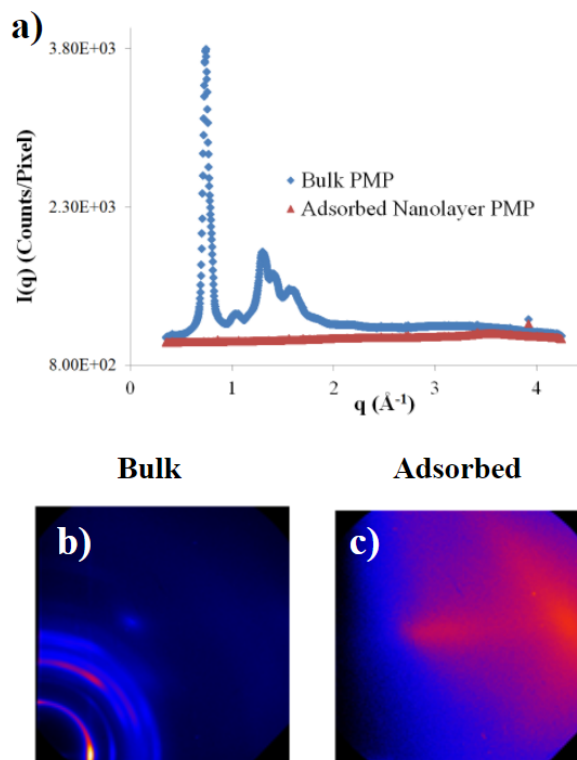
break the crystal structure sufficiently to induce adhesion, particularly in the case of thinner PMP films (¡200 nm). Unfortunately, due to technical constraints, the ultra-high vacuum oven that was utilized does not allow for temperatures above 150°C.

In an attempt to circumvent this, we conducted the same PMP compressed sandwich experiments shown in Table 1 again but using a non-vacuum ceramic oven capable of reaching temperatures far above the ultra-high vacuum oven. The PMP sandwiches were annealed at 280°C for no more than 1 hour in the ceramic oven. Only a short annealing time was used for these experiments since annealing for longer times at such high temperature and under non-vacuum conditions risked inducing oxidation and degradation of the polymer.

Despite this additional measure, no measurable degree of adhesion was found for any PMP sandwich annealed at 280°C in the ceramic oven (data not shown), regardless of film thickness. This is likely due to the fact that 1 hour annealing may not have been enough time to break the PMP crystalline structure, particularly given the polymers high Mw (514,000 kDa) and thus high viscosity. This is supported by previous work by Jiang and coworkers which found that achieving polymer chain relaxation and adsorption during thermal annealing processes at substrate sur-

Table 1: The pairings for the individual adhesion test trials that were conducted along with the resulting fracture stress that was measured for each situation. Replicates of all the samples shown in Table 1 were performed at least 3 times with no variability between trials with the exception of the final column (200nm 200nm PEO sandwich), which was only performed once.

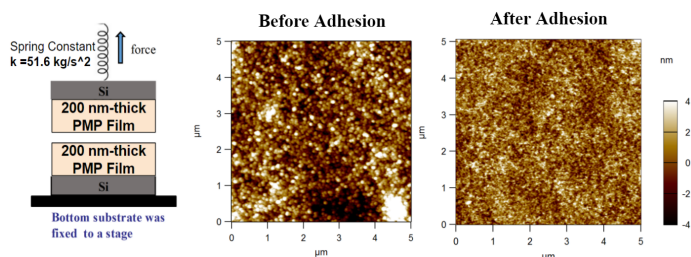| Top Layer Thickness (nm)	200	200	50	70	200	200
Bottom Layer Thickness (nm)	2.1 (ads.)	5	50	70	70	200
Fracture Stress (Pa)	0	0	0	0	0	154

Figure 5: AFM images of the bulk 200 nm thick PMP film before and after the fracture adhesion experiment.

faces required annealing times of at least 10 hours [13].

We hypothesized that previous attempts using thermal annealing were not successful in inducing PMP film adhesion because they failed to break the crystalline structure of the polymer. In an alternative approach, an experiment using solvent treatment to temporarily break the PMP crystalline structure was conducted in order to confirm that the lack of adhesion in the PMP films is due to the polymers crystallinity. Heated chloroform at 60°C was dropped onto 70 nm thick bulk PMP films which were then immediately sandwiched on one another and compressed using the 1 kg weight at room temperature. This process is illustrated in Fig. 6.

The use of hot solvent was expected to be a more effective method to induce rapid breakage of the PMP crystalline structure as compared to thermal annealing. Fracture stress adhesion tests on the samples produced in the Fig. 6 process indicated that interfilm adhesion did take place when treated first with hot solvent. Evidence of adhesion in this experiment is seen in the fact that the films did not separate when flipped or handled when being mounted on the adhesion testing device. However, once the adhesion test began to pull the sandwiched films, they immediately fell apart with negligible change in caliper width. Thus, the actual fracture stress was very low (¡100 Pa) and was out of the accurately measurable range of our stress test equipment (data not shown). This experiment provides evidence that the PMP crystalline structure is a major cause of the films failure to adhere to one another
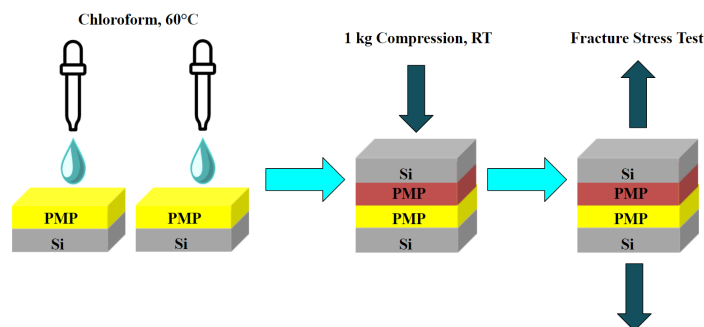

Figure 6: Process diagram of experiment to break PMP crystallinity using heated chloroform solvent. The heated solvent was intended to break the crystalline structure of the PMP thin film more quickly than conventional thermal annealing would. This was done in order to verify that it is in fact the crystalline structure that is the barrier to PMP thin film adhesion.

and suggests that a more effective way at breaking the crystallinity of the high Mw PMP chains would allow for a greater degree of interpolymer adhesion.

3.3. Comparative Semi-Crystalline Polymer System, PEO

PEO 100 kDa sandwiches of 50 nm thickness were annealed with 1 kg weight compression at 40°C for 48 hours. This annealing temperature for PEO is greater than the polymers Tg but less than the polymers Tm, a situation that mimics annealing the PMP layers at 150°C (as seen in Table 1). No measurable adhesion occurred between PEO sandwiched films that were annealed at this temperature. Conversely, a second identical group of PEO film sandwiches were annealed at 90°C, a temperature far above both Tg and Tm for PEO. The adhesion for this film sandwich was found to be 86 kPa, orders of magnitude greater than what was seen for the PMP samples of the PEO samples annealed below melting point temperature. These experiments with a comparative PEO system serve to verify that breaking the crystalline structure of the polymer film system is crucial to inducing a strong interpolymer adhesion (Fig. 7).

The semi-crystalline properties of PEO make it a comparable polymer system to PMP. As such, PEO sandwiched samples (prepared in the same way as PMP) were utilized to verify that PMP crystallinity is the primary reason for the failure of bulk films to adhere to one another under thermal annealing conditions. PEO 100 kDa has a glass transition temperature (Tg) of −67°C and a melting point (Tm) of 65°C. Both PMP and PEO have similar degrees of crystallinity.

4. Discussion

Technical constraints prevented thermal annealing the PMP films under high vacuum at temperatures higher than 150°C, and a ceramic oven was subsequently used

$$\mathbf{T_{an} \gg T_m \gg T_g} \qquad \mathbf{T_m \gg T_{an} \gg T_g}$$

Inter-chain entanglement at
polymer interface,
adhesion

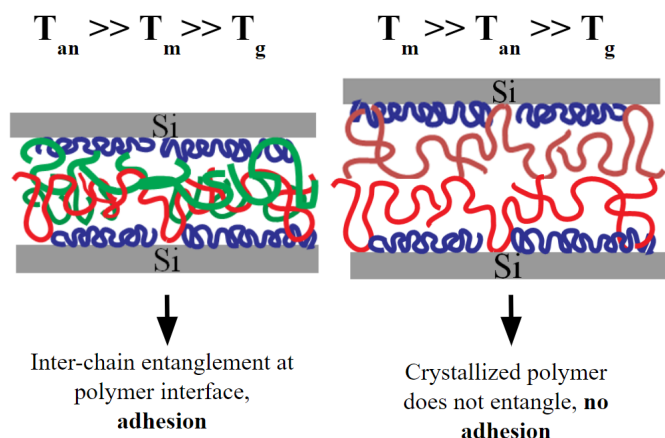Crystallized polymer
does not entangle, **no
adhesion**

Figure 7: Illustration showing the polymer adhesion model proposed in this investigation: (1) Annealing at temperatures above the melting and glass transition temperature ensures polymer crystalline structure is broken and entanglement happens at the interface, leading to film adhesion, (2) Annealing at temperatures above the glass transition temperature but below the melting point results in polymer crystal structure being maintained and failure of film adhesion due to lack of chain entanglement at the polymer-polymer interface.

to anneal the films at 280°C. However, due to concerns over oxidizing the polymer under non-vacuum conditions in the ceramic oven, high temperature annealing was limited to 1 hour, which was unlikely to be long enough to break the crystalline structure of the high Mw polymer.

A final attempt to break the PMP crystalline structure and verify its role in film adhesion was conducted using heated solvent treatments of the film prior to sandwich compression (Fig. 6). While this experiment succeeded in yielding adhesion between the PMP films, it was not to an order of magnitude measurable by the fracture test equipment. However, the results indicated that successfully breaking the PMP films crystalline structure would induce greater interpolymer film adhesion.

Lastly, the comparison of PMP against a PEO polymer system confirmed that breaking the crystal structure of a polymer is one of the most critical elements in inducing bulk interpolymer film adhesion. When the PEO sandwiches were annealed at temperatures above Tg but below Tm (mimicking the situation of annealing the PMP films at 150°C) no adhesion occurred. However, when the annealing temperature was raised far above the melting point, there was a strong adhesion between PEO films, orders of magnitude larger than what was seen with the PMP sandwiches. This provides strong evidence to suggest that breaking the polymer films crystalline structure is the most crucial element in inducing bulk film adhesion and failure to do so due to technical constraints was likely why little to no bulk PMP adhesion was achieved during this investigation.

Thus, it has been demonstrated that breaking a polymer films crystallinity is crucial in obtaining interpolymer

bulk film adhesion. This can be achieved either through thermal annealing or via solvent treatment of the film. Secondly, within the highly confined regime near the substrate surface, adsorbed polymer chains are highly averse to diffusion as a result of long range substrate effects and thus exhibit nonexistent adhesive properties. These findings shed light not only on to the specific nanoconfined properties of the PMP polymer system but can be generalized in describing adhesive properties in a variety of other crystalline and semi-crystalline polymer systems (e.g. PEO).

This investigation determined that neither PMP bulk films nor PMP adsorbed layers exhibited adhesive properties when sandwiched and thermally annealed at 150°C. Interestingly, the reasons for the lack of adhesion from these two different substrate conformations arise from two distinct mechanisms. It was shown through WAXS experiments that the PMP adsorbed layers are amorphous in structure whereas the bulk films have a crystalline structure (Fig. 4). The adsorbed PMP layers demonstrated a lack of adhesion likely due to the propagation of long range substrate effects. As reported by Zheng and coworkers in 1997, polymer chain mobility exponentially decreases near the substrate surface as a result of the enhanced entanglement [6]. These effects can propagate several nanometers into the film interior from the substrate surface and result in a dead layer of polymer near the substrate surface that greatly reduce chain diffusivity. Since interpolymer chain diffusion at the polymer-polymer interface is crucial towards creating adhesion [12], it is likely that the long range substrate effects on the adsorbed PMP chains reduced their diffusivity and prevented them from diffusing into the free polymer chains above them, despite their amorphous properties (Fig. 8).

Bulk Overlaying Chains
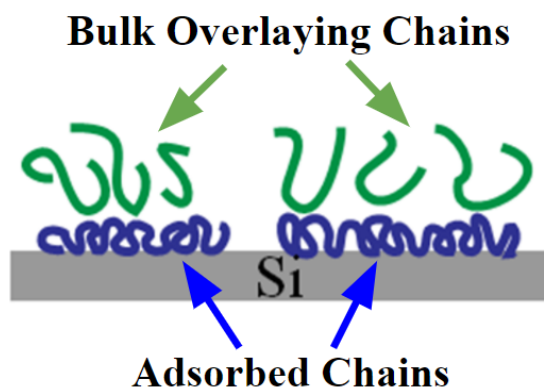
Adsorbed Chains

Figure 8: Illustration showing the amorphous adsorbed chains failing to entangle with the bulk chains above them as a result of substrate surface diffusion diminishment effects   the mechanism behind the lack of adsorbed layer adhesion.

On the other hand, the lack of adhesive properties of the bulk PMP films can be attributed to technical constraints of the investigation that were unable to break the PMP films crystalline structure. The initial anneal-

ing temperature of 150°C highlighted that even bulk PMP films do not adhere to one another unless at great thicknesses of 200 nm or above (Table 1). In the case of the 200 nm PMP sandwich which did demonstrate adhesion, there was a noticeable decrease in polymer surface crystallinity according to post-adhesion test AFM imaging (Fig. 5), further suggesting that breaking the crystallinity of the polymer film is crucial to developing interpolymer adhesion. However, given that 150°C (while above Tg) is well below the melting point of PMP (240°C), it is unsurprising that the PMP crystalline structure was not broken under these annealing conditions.

Technical constraints prevented thermal annealing the PMP films under high vacuum at temperatures higher than 150°C, and a ceramic oven was subsequently used to anneal the films at 280°C. However, due to concerns over oxidizing the polymer under non-vacuum conditions in the ceramic oven, high temperature annealing was limited to 1 hour, which was unlikely to be long enough to break the crystalline structure of the high Mw polymer.

A final attempt to break the PMP crystalline structure and verify its role in film adhesion was conducted using heated solvent treatments of the film prior to sandwich compression (Fig. 6). While this experiment succeeded in yielding adhesion between the PMP films, it was not to an order of magnitude measurable by the fracture test equipment. However, the results indicated that successfully breaking the PMP films crystalline structure would induce greater interpolymer film adhesion.

Lastly, the comparison of PMP against a PEO polymer system confirmed that breaking the crystal structure of a polymer is one of the most critical elements in inducing bulk interpolymer film adhesion. When the PEO sandwiches were annealed at temperatures above Tg but below Tm (mimicking the situation of annealing the PMP films at 150°C) no adhesion occurred. However, when the annealing temperature was raised far above the melting point, there was a strong adhesion between PEO films, orders of magnitude larger than what was seen with the PMP sandwiches. This provides strong evidence to suggest that breaking the polymer films crystalline structure is the most crucial element in inducing bulk film adhesion and failure to do so due to technical constraints was likely why little to no bulk PMP adhesion was achieved during this investigation.

Thus, it has been demonstrated that breaking a polymer films crystallinity is crucial in obtaining interpolymer bulk film adhesion. This can be achieved either through thermal annealing or via solvent treatment of the film. Secondly, within the highly confined regime near the substrate surface, adsorbed polymer chains are highly averse to diffusion as a result of long range substrate effects and thus exhibit nonexistent adhesive properties. These findings shed light not only on to the specific nanoconfined properties of the PMP polymer system but can be generalized in describing adhesive properties in a variety of other crystalline and semi-crystalline polymer systems (e.g. PEO).

5. Conclusion

In this investigation, we have characterized the nanoconfined properties of a new type of polymer, PMP. Using this polymer as a model system to study nanofilm adhesion, we have demonstrated that film crystallinity and surface substrate effects play dominant roles in governing the adhesivity of polymer nanofilms.

This investigation has also yielded industrially relevant findings. We have demonstrated that crystalline polymers do not heal easily unless they have been sufficiently raised above the melting point temperature and annealed for enough time for the entirety of the crystalline structure to be broken. We have also demonstrated that it is the reptation of polymer chains across an interface that yields adhesive properties and that such reptation is often dependent on annealing temperatures or conditions that break the crystalline structure in crystallizing polymers. This is a finding which provides important insight into the structural-mechanical properties of polymers being used as adhesives.

Specifically, industrial applications of our findings include the future development of PMP as a non-adhesive polymer coating. It has been demonstrated that PMP films at the nanoscale are still extremely robust and are highly resistant to dewetting at high temperatures, chemical treatment with organic solvents, and compression stress. Moreover, the adsorbed layer of the PMP films (2.1 nm thickness) demonstrated very high slippability owing to its non-interactive and non-adhesive nature, making it ideal for chemically resistant and adhesively inert industrial coatings. Furthermore, the ease of the preparation of these PMP adsorbed films (i.e. a simple annealing and leaching process) makes their industrial implementation highly facile and highlights the versatility of their future applications.

6. Acknowledgments

7. References

[1] Z Iqbal, W Moses, S Kim, EJ Kim, WH Fissell, and S Roy. Sterilization effects on ultrathin film polymer coatings for silicon-based implantable medical devices. *Journal of Biomedical Materials Research Part B: Applied Biomaterial*, 2017.

[2] VK Vendra, L Wu, and S Krishnan. Polymer thin films for biomedical applications. *Nanotechnologies for the Life Sciences*, 2011.

[3] M Uddin, W Ho, C Chow, and H Chan. Interfacial adhesion of spin-coated thin adhesive film on silicon substrate for the fabrication of polymer optical waveguide. *Journal of Elec Materi*, 35(7):1558 − 1565, 2006.

[4] MitsuiChemicalsAmerica. Tpx polymethylpentene (pmp) characteristics. 2017.

[5] G Reiter. Probing properties of polymers in thin films via dewetting. glass transition, dynamics and heterogeneity of polymer thin films. *Advances in Polymer Science*, pages 29 – 63, 2012.

[6] X Zheng, M Rafailovich, J Sokolov, Y Strzhemechny, S Schwarz, B Sauer, and M Rubinstein. Long-range effects on polymer diffusion induced by a bounding interface. *Physical Review Letters*, 79(2):241 –244, 1997.

[7] P Gin, N Jiang, C Liang, T Taniguchi, B Akgun, S Satija, M Endoh, and T Koga. Revealed architectures of adsorbed polymer chains at solid-polymer melt interfaces. *Physical Review Letters*, 109(26), 2012.

[8] J Carrillo, S Cheng, R Kumar, M Goswami, A Sokolov, and B Sumpter. Untangling the effects of chain rigidity on the structure and dynamics of strongly adsorbed polymer melts. *Macromolecules*, 48(12):4207 – 4219, 2015.

[9] W Xia, D Hsu, and S Keten. Dependence of polymer thin film adhesion energy on cohesive interactions between chains. *Macromolecules*, 47(15):5286 – 5294, 2014.

[10] B Balzer, S Mucciula, S Dodoo, M Zerball, M Gallei, M Rehahn, R Klitzing, and T Hugel. Adhesion property profiles of supported thin polymer films. *ACS Appl. Mater. Interfaces*, 5(13):6300 – 6306, 2013.

[11] N Jiang, J Wang, X Di, J Cheung, W Zeng, M Endoh, T Koga, and S Satija. Nanoscale adsorbed structures as a robust approach for tailoring polymer film stability. *Soft Matter*, 12:1801 – 1809, 2016.

[12] N Jiang, M Sen, W Zeng, Z Chen, J Cheung, M Morimitsu, M Endoh, T Koga, M Fukuto, G Yuan, S Satija, J Carrillo, and B Sumpter. Structure-induced switching of interpolymer adhesion at a solidpolymer melt interface. *Soft Matter*, 14:1108 – 1119, 2018.

[13] N Jiang, J Shang, X Di, M. K Endoh, and T Koga. Formation mechanism of high-density, flattened polymer nanolayers adsorbed on planar solids. *Macromolecules*, 47(8):2682 – 2689, 2014.

JᴜCER

Purification of Wastewater from Brewery Using Hydrate Approach

Jasmine Parmar[a], Adrian Laus[a], Aixin Yu[a], Jeremiah Pan[a], Jorge Velasco[a], Arthur Rozario[a], Devinder Mahajan[a]

[a]*Department of Material Science and Chemical Engineering, Stony Brook, NY 11794, USA*

Abstract

In a recent report in the Water Futures Partnership, a collaboration between the SABMiller Brewing Company and the World Wildlife Fund (WWF), reported that the water footprint of SABMillers operations in the countries of Peru, Tanzania, Ukraine and South Africa accounted for at least 89% of the total water usage. That amounts to 181 liters of water per liter of beer produced. Therefore, it takes roughly five liters of water to produce one liter of beer. This paper discusses a novel method to treat wastewater effluent. Our approach utilizes formation of clathrate propane hydrate by mixing propane at 400-500 kPa pressure with wastewater in a windowed reactor, and then using a cooling bath to lower the temperature to +1-2 °C. The collected clean water is achieved by separating the hydrates, and then decomposing these by warming it to room temperature. The water purity is then tested using Total Suspended Solids (TSS). The formation of propane hydrates reduces the number of suspended solids in brewery wastewater and therefore increases water purity. In one sample, the wastewaters initial average TSS was 630 mg/L, and after treatment, it was 413 mg/L. It was found that this decrease did not meet the literature TSS EPA standards for wastewater of 45 mg/L. This change in TSS is partially also due to the sedimentation of the particulate solids during the duration of the experiment. We noted that the experiments were somewhat sensitive to conditions. For example, the pressure of the reactor decreased during the experiment suggesting hydrate formation though hydrates were not visible in certain cases. If the temperature of the reactor was kept stable below 2 °C and it were fully submerged into the water bath to ensure good insulation, then the formation of propane hydrates would have been clearer.
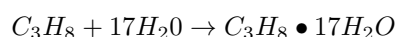
Keywords: Graphene nanoplatelets, Propane hydrates, Water Activated Sludge (WAS), Total Suspended Solids (TSS)

1. Introduction

1.1. Background

Gas hydrates are ice-like clathrate structures composed of lattices containing hydrogen-bonded water molecules. The water in these hydrates have a strong affinity towards guest molecules through Van Der Waals forces. The guest molecules are small gas molecules such as $CH_4, C_2H_6, C_3H_8, CO_2$, and volatile liquid molecules, such as tetrahydrofuran (THF) [1]. Gas hydrates are typically studied for their formation in natural gas pipelines that results in blockage [2]. In current studies, there are theories on the formation and decomposition of hydrates.

Figure 1: Possible Clathrate Hydrate structures.

Figure 1 displays possible structures that clathrate hydrates can form [3]. The chemical equation for propane hydrate formation from water and propane can be shown by the following equation [4]:

$$C_3H_8 + 17H_20 \rightarrow C_3H_8 \bullet 17H_2O$$

Propane molecules form structure II hydrates (shown in middle of Figure 1) which are body centered and cubic, containing 136 water molecules. Propane has the ability to stabilize the water lattice since it occupies the empty cavities. The more empty cavities that become occupied, the more stable the structure will be due to Van Der Waals forces [5]. Although there are studies on the kinetics of propane hydrates, there are no studies on their possible use in clean-up of wastewater breweries.

It is hypothesized that the formation of propane hydrates will separate pure water from contaminants in wastewater collected from a brewery and the treated water could be disposed of if it met the EPAs published secondary treatment standards for a TSS of 45 mg/L [6]. Propane was chosen since it has an equilibrium pressure lower than other gases. Previous research from our group was done on a dewatering process on a waste activated sludge (WAS) sample based on propane hydrate forma-
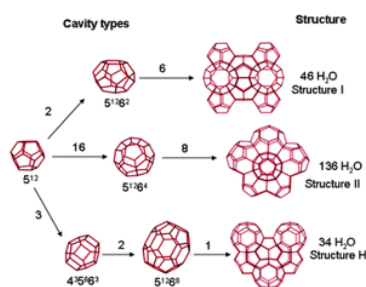
tion, whereby water extracted from the wastewater was up to 48.1%. This led to the idea that this method could similarly treat brewery wastewater [7]. The hydrate approach offers a sustainable green process for the disposal of wastewater and does not require the need for additional conditioning reagents [1].

1.2. Hydrate Formation

The formation is an exothermic crystallization process. Generally, there are three steps when forming hydrates: dissolution, nucleation, and growth. The following equations indicate the principle of hydrate formation process. where G represents gas molecule, N represents nucleus,

$$G(g) \underset{k_{-1}}{\overset{k_1}{\rightleftharpoons}} G(aq)$$

$$m \cdot G(aq) + n \cdot H_2O \underset{k_{-2}}{\overset{k_2}{\rightleftharpoons}} N$$

$$N \overset{k_3}{\longrightarrow} H$$

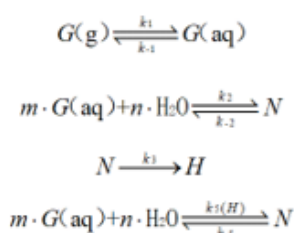$$m \cdot G(aq) + n \cdot H_2O \underset{k_{-5}}{\overset{k_{5(H)}}{\rightleftharpoons}} N$$

Figure 2: Hydrate Formation.

and H represents hydrates.

A typical plot for a hydrate kinetic experiment is shown in Figure 2 [1]. The first stage is the dissolution stage, where gas dissolves into the water until the saturate condition. The second stage is the nucleation stage, where further dissolution leads to the supersaturated condition that causes nuclei formation. As shown in Figure 2, the nucleation stage is the slowest stage of hydrate formation. When the turbidity point is reached, the growth stage is initiated, which is a relatively fast process. In earlier reported studies [1], it was successfully determined that the reaction rate constant for propane hydrate (sII) formation was $2.15 \times 10^7 mol/s$ at 274.2 K.
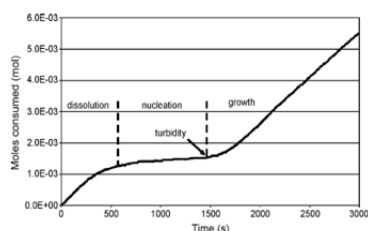
Figure 3: Kinetic Process of Hydrate Formation

2. Methodology

2.1. Materials

The materials used in this experiment consisted of propane gas, ethylene glycol, and wastewater. The ma-

terials used in the TSS measurement consisted of deionized water, a suction flask, crucible, glass-fiber filter disk, aluminum dish, desiccator, oven, 50 ml graduated cylinder, and analytical balance ($\pm 0.0001g$). Propane was the source of gas for the experiment. Additionally, the wastewater sample was obtained from Port Jefferson Brewery. This sample was high in carbohydrates and protein, as well as alcohol and dissolved sugar. Based on calculations, water percentage of the brewery wastewater sample was 93%. Ethylene glycol was used as the coolant since it is stable and generally used for antifreeze formulations. The ethylene glycol served to cool the system to attain the desired temperature to form hydrates [8]. Both pressure transducer and thermocouple were used in the set up. The OMEGA Engineering, Inc., USA pressure transducer had a measurement accuracy of $\pm 5kPa$ and the Extech Instruments, Inc., USA thermocouple had a measurement accuracy of $\pm 0.1K$ [9].
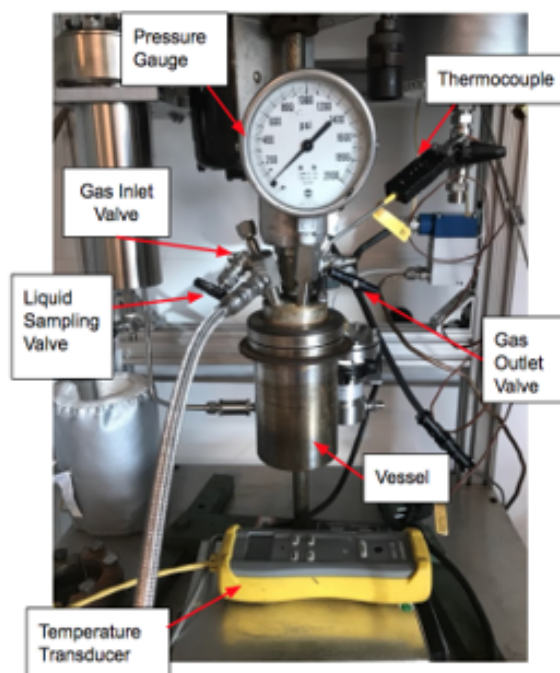
2.2. Experimental Set-Up

Figure 4: Batch Reactor Setup with key labeled components.

A bench-top batch reactor, shown in Figure 4, was initially used to promote kinetics of hydrate formation [5]. However, there was no visual method to analyze the hydrates growth process. Though the reactors stainless-steel vessel created optimal insulation, proper calculations regarding the sludge phases separation and formation could not be made without visual observation. A switch to a reactor with see-through windows of 30 cm high and 1.5 cm wide, shown in Figures 5 and 6, allowed for observations in the separation of phases and the formation process of propane hydrate. The total volume of the reactor

was 750 mL. This windowed reactor approach allowed for visual representation of the hydrate formation as well as the ability to measure the percentage of hydrates formed. With this switch from a stainless-steel vessel, new insulation techniques as shown in Figure 6 were required as well. Figure 5 offers a schematic diagram of the window reactor
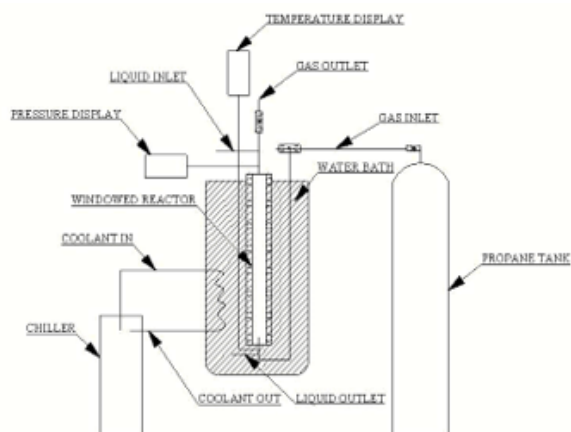

Figure 5: Schematic of Windowed Reactor.

used, and below is an actual picture of the window reactor. The reactor was designed before being implemented to offer the advantage to observe hydrate formation. The
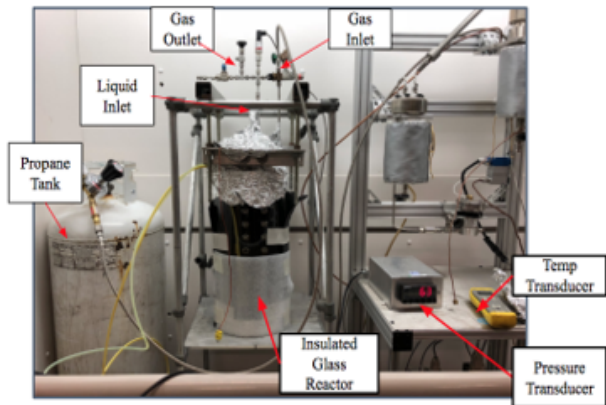

Figure 6: Schematic of Windowed Reactor.

reactor is submerged in a water bath that is necessary to attain the desired operating temperature for hydrate formation. A thermocouple is installed at the bottom of the reactor for temperature reading. Since a glass container was used to hold the water bath, ceramic fiber insulation and ThermoTec adhesive backed heat barrier insulation was used to surround the glass water bath to maintain an internal reactor temperature of 274.85 K. Polystyrene foam peanuts were placed on the surface of the water bath to provide more means for insulation as well. The chiller used contained ethylene glycol and was used to control the temperature of the water bath and the reactor. Because

the density of propane hydrate is $0.78 \times 10^{-3} kg/cm^3$, the hydrate formation should happen at the liquid-gas interface [10].

2.3. Upsurge Method

Propane gas was pumped through the gas inlet using the gas upsurge method to agitate the wastewater. Agitating wastewater in this way breaks the surface tension and helps adhere some of the liquid to the sides of the reactor. This will aid in the formation of propane hydrates at the liquid/gas interface as it allows contact with the gaseous propane, similar to stirring [2].

2.4. Hydrate Purity Analysis

The total suspended solid (TSS) was crucial in this study. It was hypothesized that the formation of propane hydrates would reduce the number of suspended solids in brewery wastewater and therefore purify the water to meet the EPA disposal standard. TSS in the wastewater sample was tested before and after the experiment in Stony Brook Universitys Water Center in the Heavy Engineering building to determine the before and after treatment values.

To measure TSS of initial wastewater, deionized water was used as a blank. 25 mL of wastewater was filtered by in an apparatus consisting of a suction flask, crucible, glass-fiber filter disk, and aluminum dish. The residue on the filter was dried overnight in the oven at 105 °C and was cooled down in the desiccator for 15 minutes. To make the result of the measurement more exact, we conducted the TSS test twice on the initial sample and calculated the average TSS and standard deviation.

We also considered possible sedimentation of the solid particulates in the WAS when measuring the TSS of the wastewater. Besides deionized water, we also used the untreated wastewater as a control. The wastewater after treatment was extracted from the top of the reactor with a needle. Likewise, the sample of untreated wastewater was collected from the liquid layer, which would be partially separated from the bottom solid layer even without treatment. Following the same procedure, the TSS measurement was conducted twice for each wastewater sample.

3. Results

3.1. Phase Diagram

To predict the equilibrium conditions of hydrates formation, we used the CSMHYD program developed by Prof. E. Dendy Sloan, Colorado School of Mines, Golden, Co, USA to draw the phase diagram. As shown in Figure 6, the equilibrium pressure of hydrates is 232 kPa (33.6 psi) at 274.65 K (1.5 °C). Based on the phase diagram, it can be predicted when the system will reach equilibrium.
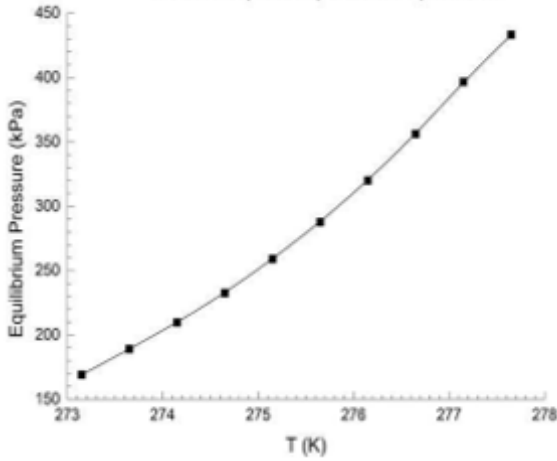
Figure 7: Theoretical Equilibrium Pressure with Propane Water.

3.2. Mass Balance Analysis

Mass balance analysis of the propane hydrate WAS was viewed in terms of changes in the water content between the sludge phase and the hydrate phase. The amount of propane from the reactor being converted into the hydrate phase can be calculated by using the ideal gas law. Since the density of propane hydrates ($\sim 0.78 \times 10^{-3} kg/cm^3$) is lower than that of water, the conversion of water from the WAS into hydrates would cause volume expansion of the solid phase, decrease in the liquid phase, and a decrease of the gas phase [10].

For each batch run i, the initial gas volume V_i, at the beginning of each run should be equal to the final gas volume V_{i-1} of the of batch run $i-1$. The amount of propane converted into the hydrate phase:

$$\Delta n_i = n_i - n_i' = \frac{PV_i - P'V_i'}{RT} \quad (1)$$

Where n_i and n_i are the initial and final number of moles of propane gas in batch run i, respectively; R is the universal gas constant ($8.314 \ J/molK$), T is the experimental temperature, P and P are the initial and final partial pressure of each batch run, respectively. The final gas volume of the ith batch run:

$$V_i' = V_i - (\frac{(n_i - n_i')M_p ropanehydrates}{\rho} \quad (2)$$

Where $M_{propanehydrates}$ is the molar mass of propane hydrates ($44 \ g/mol$) and $_{propanehydrates}$ is the density of propane hydrates [11].

The relationship between the initial and final volumes of each batch run was calculated by solving equation (1) and (2) simultaneously such that:

$$V_i' = 0.998V_i \quad (3)$$

The mass of the water converted from the sludge phase into hydrates was calculated using the stoichiometric relationships of the reaction that states that for every propane molecule there would be 17 attached water molecules. Therefore, the mass of the water trapped in the hydrates in batch run i is:

$$m_i = 17\Delta n_i * M_{H_2 0} \quad (4)$$

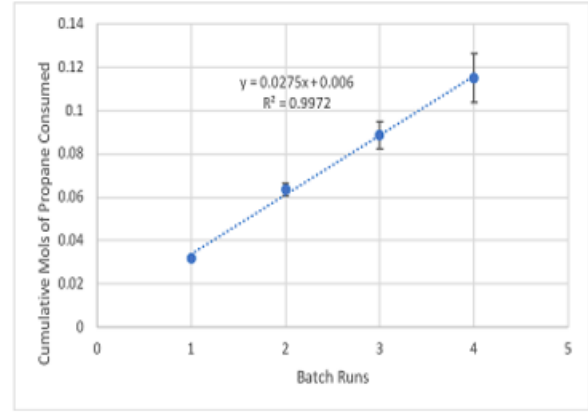Where M_{H_2O} is the molar mass of water ($18 \ g/mol$).

Figure 8: Propane consumption by the hydrates with successive batch runs.

The calculated results of the amount of propane used in hydrates formation was summarized in Figure 8. The error was determined using the accuracy of the instruments used. It is shown that as more batch runs occur, the amount of propane being trapped in the hydrate phase increases. After each consecutive batch run, the moles of propane being converted into hydrates decreases, indicating that as more batch runs occur, the amount of hydrates being formed would also decrease since the amount of available water decreases in each subsequent run.
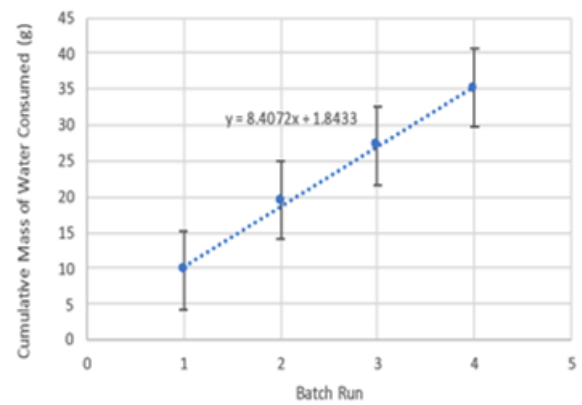

Figure 9: Mass of water being consumed by hydrates with successive batch runs.

Considering that the water percentage of the wastewater was 93%, there was 279 g of water in the original wastewater. Using the amount of propane consumed and

27

Equation (4), the water content in the WAS was calculated to decrease from 93% to 81%, after 4 batch runs. This amounts to 35 g of water removed as seen in Figure 10. Further batch runs would be needed to test the limit to which the water content could be reduced.
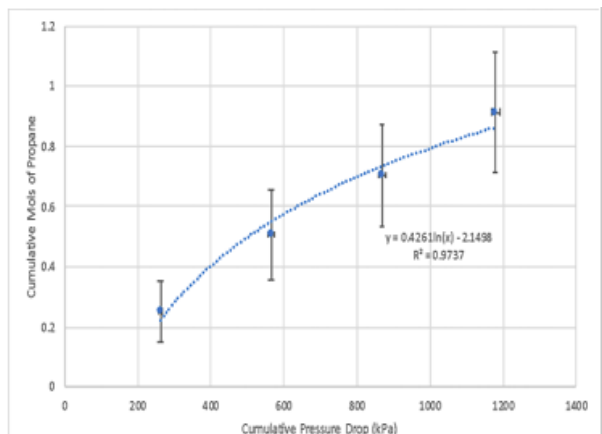

Figure 10: Propane consumption by hydrates as a function of successive pressure drops for successive batch runs.

Figure 10 shows the number of moles consumed by the hydrates as a function of the cumulative pressure drop of the reactor for each batch run. As seen on the graph, the amount of propane being consumed decreases as the batch runs continue. This suggests that the formation of hydrates becomes more difficult as more hydrates form.
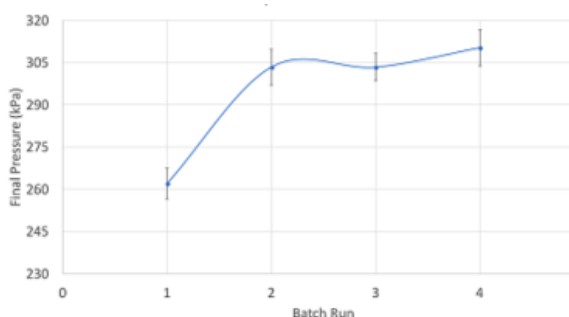
3.3. Temperature and Pressure Analysis

Figure 11: Final pressure of the system after propane and water consumption for successive batch runs.

Figure 11 shows the final pressure of the system after each batch run. Based on the general curve of the line, the final pressure of the reactor was increasing, and will continue to increase as more runs are conducted. This is in accordance to the suggestion that the formation of hydrates for each run gets more difficult as more batch runs are conducted.

The optimal temperature that the we tried to achieve was 274.85 K. Figure 12 shows the temperature fluctua-
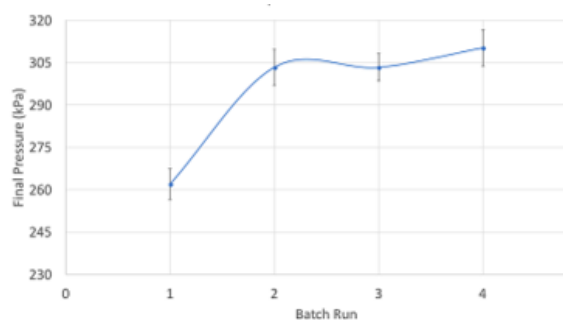

Figure 12: Temperature fluctuation of the reactor for successive batch runs.

tions of the reactor. This is due to the insufficient insulation and the changing weather conditions. Since hydrates are very temperature and pressure dependent, the fluctuations in temperature could have caused propane hydrate decomposition during the batch runs. This decomposition could have affected the accuracy numbers for propane gas in the hydrates and therefore mass of water consumed.

3.4. TSS Measurement

TSS measurements were conducted in Stony Brook Universitys Heavy Engineering building. Using deionized water as a blank sample, the TSS measurements were conducted twice, and the average was taken for each.
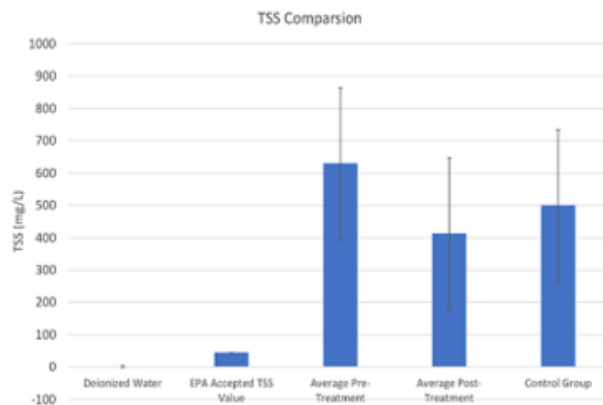
Figure 13: Total Suspended Solids Comparison.

Figure 12 shows the average values for the TSS measurements taken pre- and post- treatment, which was inconsistent with reported values [11]. Considering that the TSS value for pre-treatment was higher than that of the post-treatment, we can conclude that some purification of water occurred. However, the control group shown in Figure 12 suggests that some of the purification of the wastewater was due to sedimentation of the particulates to the bottom of the beaker. Since the purification was due to hydrate formation, the sedimentation of the solids, or a combination of both, further testing is required.

4. Conclusion

A brewery wastewater dewatering process using propane hydrates was studied in this experiment. The constructed phase diagram based on pure water was used to help determine the preliminary temperature and pressure conditions for the reactor. The TSS results show that water remaining after hydrate formation contained less TSS, thus pointing to water purification. This could be due to either the formation of propane hydrates or the sedimentation of the solids at the bottom due to the density difference.

Although the pressure drop during each batch run indicates hydrate formation to some degree, no visual hydrates could be seen through the window of the reactor. This could be due to the fluctuation in temperature causing the decomposition of the propane hydrates. Since hydrate formation is sensitive to temperature fluctuation, any future endeavor should focus on temperature stability. Once propane hydrates become visible, the effect on the TSS of the wastewater should be clearer. The results show promise, but further testing is required to investigate the effects of propane hydrates on brewery wastewater.

5. Acknowledgement

6. References

[1] Sebastien Bergeron and Phillip Servio. Reaction rate constant of propane hydrate formation. *Fluid Phase Equilibria*, 265(1-2):3036, 2008.

[2] Carlo Giavarini, Filippo Maccioni, and Maria Laura Santarelli. Formation kinetics of propane hydrates. *Industrial & Engineering Chemistry Research*, 42(7):15171521, 2003.

[3] Andrea Perrin, Osama M. Musa, and Jonathan W. Steed. Cheminform abstract: The chemistry of low dosage clathrate hydrate inhibitors. *ChemInform*, 44(24), 2013.

[4] Cludio P. Ribeiro and Paulo L.c. Lage. Modelling of hydrate formation kinetics: State-of-the-art and future directions. *Chemical Engineering Science*, 63(8):20072034, 2008.

[5] Jeffery B. Klauda and Stanley I. Sandler. Phase behavior of clathrate hydrates: a model for single and multiple gas component hydrates. *Chemical Engineering Science*, 58(1):2741, 2003.

[6] Environmental Protection Agency. Npdes permit writers' manual, Nov 2016.

[7] Jong-Ho Cha and Yongkoo Seol. Increasing gas hydrate formation temperature for desalination of high salinity produced water with secondary guests. *ACS Sustainable Chemistry & Engineering*, 1(10):12181224, 2013.

[8] 8. NOAA Office of Response. Ethylene glycol.

[9] Inc. FLIR Systems. Extech instrument manual, 2014.

[10] V Buleyko, B Grigoryey, V Istomin, and V Yanovskaya. Determination of hydrate number and density of propane hydrate by means of precision adiabatic calorimetry., 2015.

[11] Enitan, Adeyemo, Kumari, Swalaha, and Bux. Characterization of brewery wastewater composition. *International Journal of Environmental and Ecological Engineering.*, 9(9), 2015.

JᵁCER

Effects of 3D printing direction and graphene content in PLA/GNP nanocomposites

Tomasz Filipkowski[a], Marija Iloska[a], Noriko Taira[a], Christopher Corbo[a], Chengfeng Gao[a], Cem Civelek[a], Yuval Shmueli[a]

[a]*Department of Materials Science and Chemical Engineering, Stony Brook, NY 11794, USA*

Abstract

Fused deposition modeling (FDM) is a method of additive manufacturing, commonly referred to as 3D printing, which can create physical objects in a layer by layer manner, from a variety of materials. It provides a wide range of applications from houses, mechanical building parts to bone grafts, dental products and other. Polymers such as polylactic acid (PLA) and acrylonitrile butadiene styrene (ABS) are often used as filament for FDM 3D printers, due to their distinct thermal properties and cost effectiveness. However, depending on the utility purpose of the printed object, the object may require different, suitable properties (e.g. high tensile strength and thermal conductivity). Here we hypothesize two ways to amend them in a cost efficient manner: by controlling the printing direction; and by adding graphene fillers in the polymer to create polymer-graphene nanocomposites. Given the flexibility of the printers, the direction of printing can be instructed by modifying the numerical control programming language - G-code, which dictates the printing nozzle movements and the filament extrusion. We created composite samples with a content of 0 wt%, 5 wt% and 10 wt% graphene nanoplatelets (GNP) for each direction. Dynamic mechanical analysis (DMA) properties were measured by 3-point bending tests. Thermal conductivity of the different compositions were measured by FLIR IR thermal camera. The vertical samples consistently showed the highest storage modulus, due to the more difficult crack propagation between filaments in that direction, whereas for graphene content, the highest modulus varied between 0 wt% and 5 wt% sample. Optimal microscopy images were developed to characterize the samples and revealed the possible phenomena of shear thinning. To account for shear thinning, two more samples were created with increased nozzle temperature, and modified G-code.

Keywords: 3D printing, fused deposition modeling, nanocomposites, polylactic acid, graphene

1. Introduction

Fused Deposition Modeling (FDM), commonly referred to as 3D printing, is the simplest form of additive manufacturing (AM) which prints physical objects layer by layer. Its capability to produce high complex geometries with a simpler and more inexpensive approach, has caught the attention of both industry and academia [1, 2]. FDM has spread its application range in a great deal of fields such as mechanical and electrical engineering by providing building parts, biomedical engineering by creating scaffolds for implants, microfluidic devices, physical and analytical chemistry, and many others [1–6]. Despite its general printing purpose, its flexibility is prominent with the option to control the layer thickness, time delay, and printing direction, simply by modifying the numerical control programming language, renowned as the G-code. Zhu et al. [7] reported that the printing direction can increase the tensile strength of the sample. Theyve conducted a study using polyamide 12 (PA12) and graphene nanoplatelets (GNP) composites, where theyve printed samples with horizontal (0°), vertical (90°) and diagonal (45°) directions, and found that the horizontal (0°) provides the highest mechanical reinforcement. This feature can prove useful when dealing with the mechanical properties of the desired sample. FDM commonly uses thermoplastics such as polylactic acid (PLA), acrylonitrile butadiene styrene (ABS), and polypropylene (PP), [2, 6, 8, 9] because of their amenability at relatively low temperatures (180-260 °C) and low cost. Additionally, the FDM printer can accept any material with a melting point within its range of temperature [4], including various polymer composites, which help manipulate both the thermal and mechanical properties of the sample, compared to using a pure polymer filament. In their paper, Zhu et al. [7] also studied the optimal GNP content in the polymer (PA12) matrix that achieves high thermal conductivity and increased elastic modulus, which they reported to be 6 wt%, based on tensile strength between compression molded samples. They found that by combining the optimal graphene content and printing in the horizontal (0°) direction, the thermal conductivity and elastic modulus improved by 51.4% and 7%, respectively. However, they only compared the storage modulus for the printing directions for the 6 wt% GNP, based on the assumption that direction and content do not have any synergistic effects.

Graphene has been known to be one of the strongest materials, with a high thermal conductivity [10, 11]. Its

an allotrope of carbon, and comprises a one layer sheet of hexagonal carbons. The C-C covalent bonds are firm and able to conduct heat rapidly, which is what makes graphene thermally resistant, as opposed to polymers, in which case heat is dissipated in the rotational energy of the loose hydrogen - carbon bonds, preventing it from travelling much further in the chain [8]. The graphene sheets, however, are weakly bonded by van der waals forces, making graphene a good thermal conductor only in one direction. Given graphenes properties, it is deemed to be suitable nanofiller for polymers to provide a quality sample of increased strength and conductivity.

In this study, three different materials were created by adding a varied concentration of graphene nanoplatelets (GNPs) (0 wt%, 5 wt% and 10 wt%) into a PLA matrix. The pure PLA and two nanocomposites were extruded into separate 3D printer filaments, and used to print three samples per composite (total of 9), in a parallel (x), vertical (y) and diagonal direction. The printing direction of the 3D printer was specified by creating a program in MAT-LAB which generated the desired G-code. The mechanical properties of all samples were compared by performing dynamic mechanical analysis (DMA), which gives the storage modulus as a function of strain (amplitude) at constant temperature [12]. The thermal conductivity of all samples was measured and compared as well. Optical microscopy was utilized to measure diameter thickness of all printed samples and observe the extent of fusion between filament layers. An additional test sample was produced with 2 varied parameters: temperature, and G-code, to adjust for the phenomena of shear thinning.

2. Materials and Methods

2.1. Composites preparation

In order to test the effects of graphene in a polymer (PLA) matrix, and the direction of printing, filaments for the 3D printer need to be created. Filaments of 3 mm diameter were utilized to print a 41.9 mm x 10.4 mm x 2.1 mm rectangular prism which corresponds to the size and shape required for DMA testing. The PLA/GNP nanocomposites were created by adding 2.5 grams of GNPs to 47.5 grams of PLA, and 5.0 g GNPs to 45.0 g of PLA, resulting in a 5 wt% and 10 wt% nanocomposite, respectively. All samples were weighed with an Ohaus brand, CS200 series scale. The appropriate amounts of GNP and PLA are mixed and heated using the Intelli-Torque Plasti-Corder® Torque Rheometer or C.W. Brabender. The C.W. Brabender was operated at a temperature of 160°C and set to an RPM of 100 during mixing. Initially, the mixing speed was set to 20 RPM as the materials are being poured. After 20 minutes, the polymer nanocomposite is considered thoroughly mixed.

2.2. Filament extrusion

The resulting melted and mixed polymer was then inserted into the pelletizer, and fully pelletized once the grinding noise, which occurs while the instrument is in function, stopped. Additional 5 minutes were given to ensure that the pellets have been fully formed. These pellets were collected from the bottom of the machine for further processing. The resulting nanocomposite pieces were extruded into filament form using the Filabot Extruder, to be then finally used in the 3D printer. The extruder was set to a temperature of 170°C and filled with the premade pellets. The pellets are ground down by the rotating gear and forced out as a 4 mm diameter filament. This filament is spooled onto a plastic spool and labeled accordingly.

2.3. Testing techniques

DMA Q800, TA Instruments was used to perform DMA, the 3-point bending test [12] in particular, to acquire the storage modulus, to further compare the optimal printing direction and graphene content. The test conditions were: frequency - 1 Hz, amplitude - 0.01-20%, 5 seconds sampling time, and temperature was held constant a 100°C. Digital microscope ADSM302 was used to observe the printed samples, and compare the extent of fusion from one filament layer to the next when printing. FLIR IR thermal camera was used to determine the thermal conductivity of the parallel sample for each GNP content. IR data was analyzed using the program Research IR. A temperature profile was created which allowed the transfer of heat to be monitored over a set period of time, thus, allowing the conductivity of each sample to be calculated.

3. Results & Discussion

3.1. Sample printing

All 9 samples with varying GNP content and different directions were printed successfully. The direction of printing is visible to the naked eye on the samples, and labeled as parallel, diagonal, and vertical, shown in Figure 1. To clarify, the direction of printing is in reference to the clamps of the DMA set up for the 3-point bending test. The sample dimensions are equal for all and were designed to be 41.9 mm x 10.4 mm x 2.8 mm. As of here, the PLA samples will be denoted with 0P, 0D, and 0V, the 5 wt% as 5P, 5D, and 5V, and the 10 wt% as 10P, 10D and 10V.

3.2. Dynamic Mechanical Analysis

The results of DMA are compartmentalized by content and by direction, to allow for a better visualization of the effect from each parameter individually. Figure 2 shows the storage modulus as a function of amplitude (strain) for each direction with varying GNP content. The printing direction is labeled at the top left corner of the graph.

Surprisingly, the 10 wt% sample steadily shows lower storage modulus for all directions, whereas the 5 wt% and the 0 wt% display some inconsistency. In the vertical direction, the 5 wt% showed higher storage modulus than the 0 wt%, and the opposite was observed for the diagonal direction. The weakness in the 10 wt% sample is
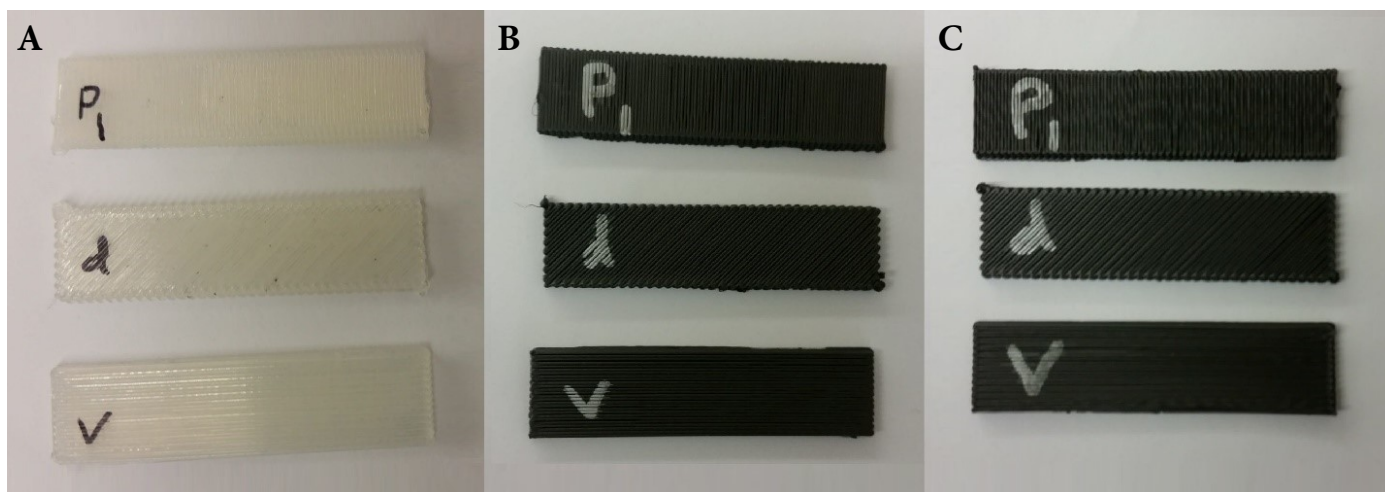
Figure 1: Printed samples: horizontal, diagonal & vertical. A) Pure PLA. B) 5 wt%. C) 10 wt%.

suspected to be due to the phenomena of shear thinning [13, 14], which affects the filament extrusion at the nozzle during printing and causes irregular (decreased) gaps.

Additionally, the GNPs are able to form some connectivity and confine the PLA chains, which also affects printing. Shear thinning is also exhibited in the 5 wt%, but more emphasized in higher GNP concentration composites. The inconsistency in the 0 and 5 wt% samples is believed to be a result of several factors, such as shear thinning, and varying extents of fusion, which depend on the 3D printing method.

Figure 3 shows the storage modulus as a function of amplitude for each GNP content with different printing direction. The GNP content is labeled in the top left corner of the graph. While it may slightly compete in the case of pure PLA, the vertical samples consistently show the highest storage modulus. For the 10 wt%, its evident that the parallel sample is lower than the diagonal, and the opposite is observed for the 5 wt% sample.

The stress is imposed on the surface filaments, which creates a crack in weaker areas nearby, especially within the gaps (between filaments) where the fusion is lowest. The crack continues to propagate along the printing direction. In the case of the vertical samples, the filaments are long and bonded further on (the edges) from where the crack begins. The long filaments prevent the crack from propagating too far, which leads to testing the strength of one bulk filament. Essentially, their length and mechanical polymer strength makes it harder to bend and break the sample. In the case of the parallel samples, the filament layer is shorter, and the crack successfully propagates through the gaps between neighboring filaments, demonstrating the diffusive weakness between layers. The parallel samples strength comes solely from the extent of fusion between neighboring filaments, thus imperfect bonding will give consistently lower readings for the storage modulus. The 10 wt% samples are strongly affected by

shear thinning, which decreases fusion. Shear thinning and lack of fusion was not discussed as a possible result of the GNP content in the work by Zhu et al [7]. Since the diagonal direction exhibits qualities of both fusion between layers, and filament strength, its stronger than parallel and weaker than vertical for the 10 wt% sample. However, the behavior of the parallel and diagonal samples for 5 wt% remains unclear. A possible explanation could be the difference in temperature during printing diagonal and parallel samples. The time from one filament to the next is shorter in the parallel sample, which makes the former filament of the parallel sample warmer than the former one on the diagonal. Naturally, if the temperature of the filaments is higher, greater amounts of fusion takes place. While this may be true for both 5 wt% and 10 wt%, its important to note that shear thinning is much more apparent in the 10 wt%, and it overcomes the better temperature induced fusion.

3.3. Optical Microscopy

As speculated in the DMA section, the addition of GNP in the polymer matrix causes shear thinning during the printing, leading to the extrusion of filaments thinner than designed. As a consequence, irregular gaps form between filaments, decreasing fusion. Optical microscopy was used to corroborate the results, shown in figure 4. The PLA sample (figure 4A) clearly shows uniformly, well fused filaments with small, equal gaps, as opposed to the 5 wt% (figure 4B) and 10 wt% (figure 4C) samples which show uneven layer thickness. Gap irregularities are marked with red arrows in figure 4B and C. To account for this phenomena, the G-code was modified to set the distance between the filaments from 0.4 mm to 0.2 mm so that the filaments will be printed closer to each other. Another sample was printed with the modified G-code and increased printing nozzle and bed temperature to assist the fusion process better.
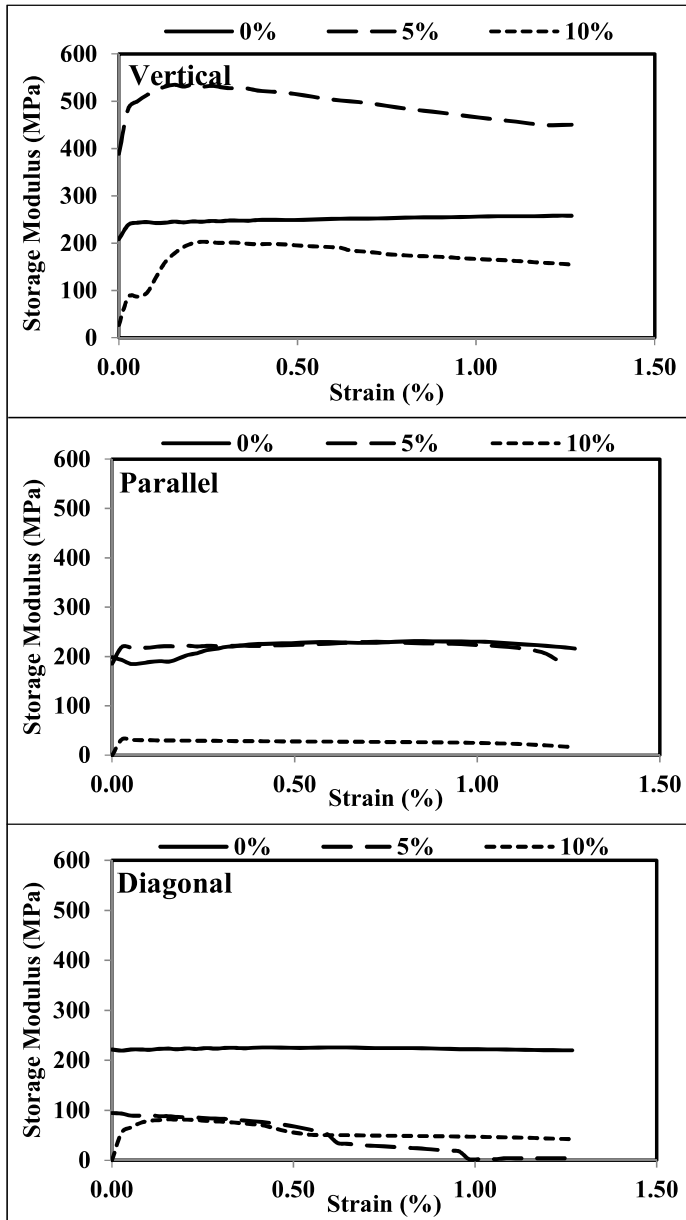
Figure 2: Storage modulus as a function of amplitude based on GNP content in each direction.

Figure 3: Comparing storage modulus as a function of amplitude based on orientation for each PLA/GNP composite.

3.4. Thermal Conductivity

Thermal conductivity measurement was carried out using a hot plate and an FLIR A325sc IR camera of only one sample. The conductivity was only measured along the direction of printing, so the parallel sample was geometrically the most convenient for the setup. Temperature was measured at every 0.1 mm for a total of 136 seconds. Figures 5 and 6 show the thermal propagation at 2 mm and 6 mm away from the starting point (max temperature) as a function of time. The greater temperature difference at a specific time implies that more heat is contained at that point, indicating that the heat travels slowly. From the graphs, its evident that overall the graphs follow an in-
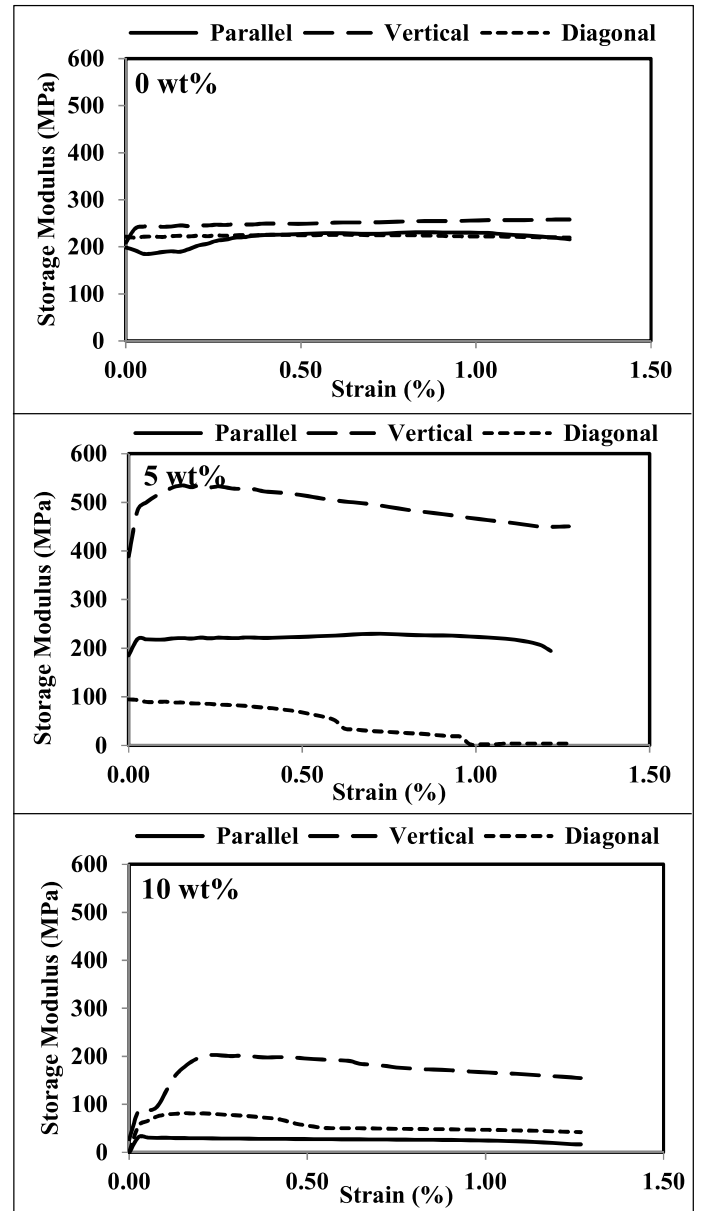
creasing trend. The higher the GNP content in the matrix, the higher thermal conductivity of the sample. Its important to note that this trend is observed because the conductivity is measured along the direction in which GNPs are oriented. Upon extrusion from the nozzle, the rigid GNPs are forced to orient along the printing direction. Scanning electron microscopy (SEM) characterization of the orientation and dispersion of GNPs after FDM 3D printing were previously studied and reported [6–8]. To quantify these results, the thermal conductivity k is expressed in terms of the heat transfer per unit time Q, and found using the equation for heat conduction:
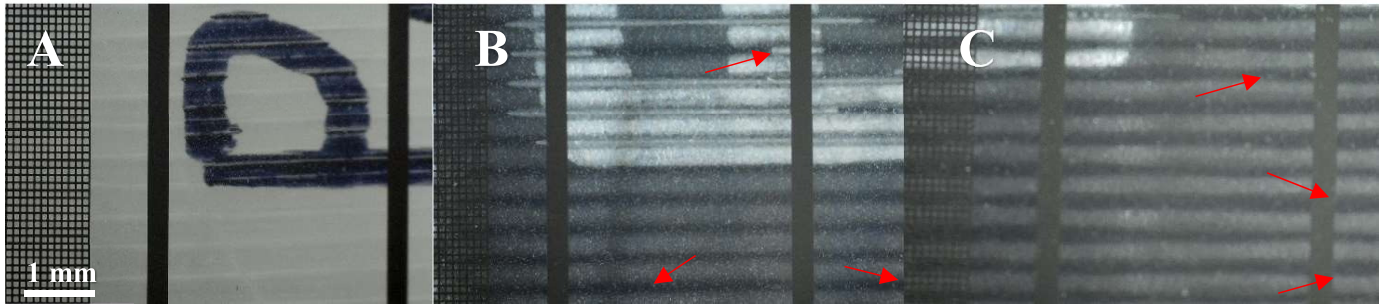
Figure 4: Optical microscopy of parallel samples. A) 0 wt% B) 5 wt%, and C) 10 wt%. Scale bar 1 mm.

$$Q = k \times A \times \frac{\Delta T}{\Delta x} \qquad (1)$$

Where, A is the cross-sectional area of one filament with diameter $= 400$ μm, Δx is the distance the heat travels through and ΔT is temperature difference between the final and the initial distance point. Q is assumed to be constant since the same heat source is used. Rearranging the equation exhibits the inverse proportionality of the thermal conductivity k with $\Delta T/\Delta x$, and supports the behavior of the graphs in figures 5 and 6. For a better visual comparison, k was found at 120 seconds and summarized in a column chart, seen in figures 5 and 6. The distance is labeled on the top left corner of the chart.
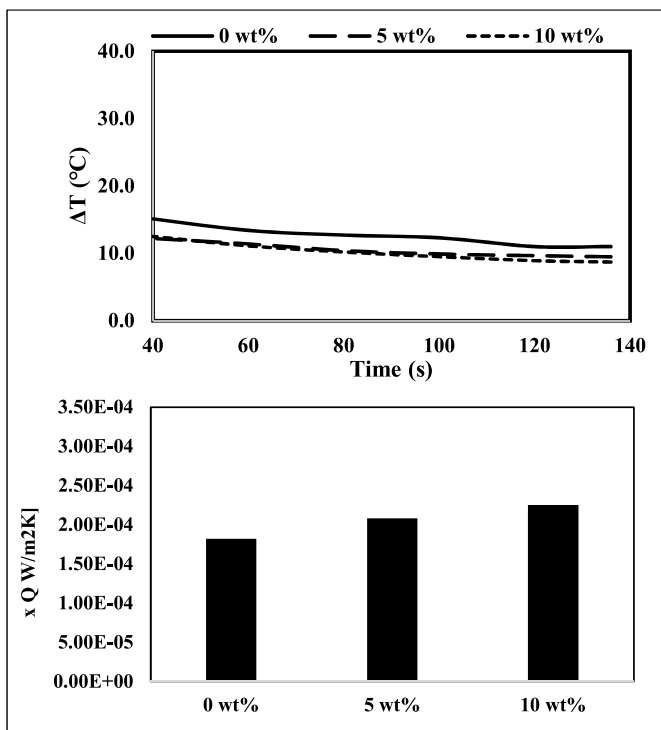

Figure 5: Thermal conductivity of the parallel sample for each GNP content, for 2 mm distance away from highest temperature point.
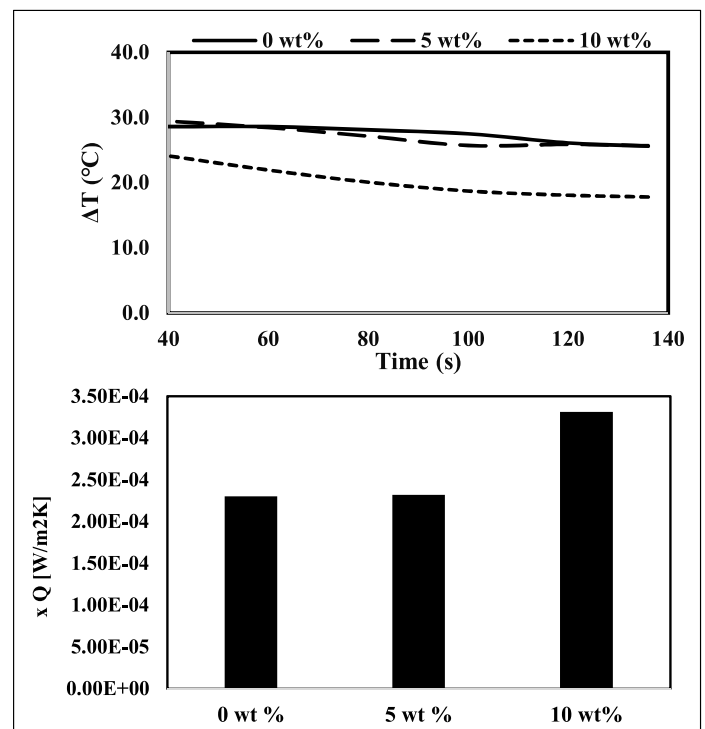

Figure 6: Thermal conductivity of the parallel sample for each GNP content, for 6 mm distance away from highest temperature point.

3.5. Preparation and analysis of new samples

Two new samples with parallel direction and 5 wt% GNP were printed with two varying parameters: G-code and printing temperature. The first sample was only modified in the G-code to decrease the filament gaps from 0.4 to 0.2, and the second was modified in the G-code and printed with an increase in nozzle temperature (260°C) and printing bed (60°C). Optical microscopy was used to observe the extent of fusion between the two and is shown in figure 7. Its evident that the filaments are better and more uniformly fused for both samples. To test the difference in mechanical strength, DMA was performed and compared to the original 5 % parallel sample. Figure 8 proves that modifying the G-code is a dominant factor for increasing storage modulus, whereas the temperature only
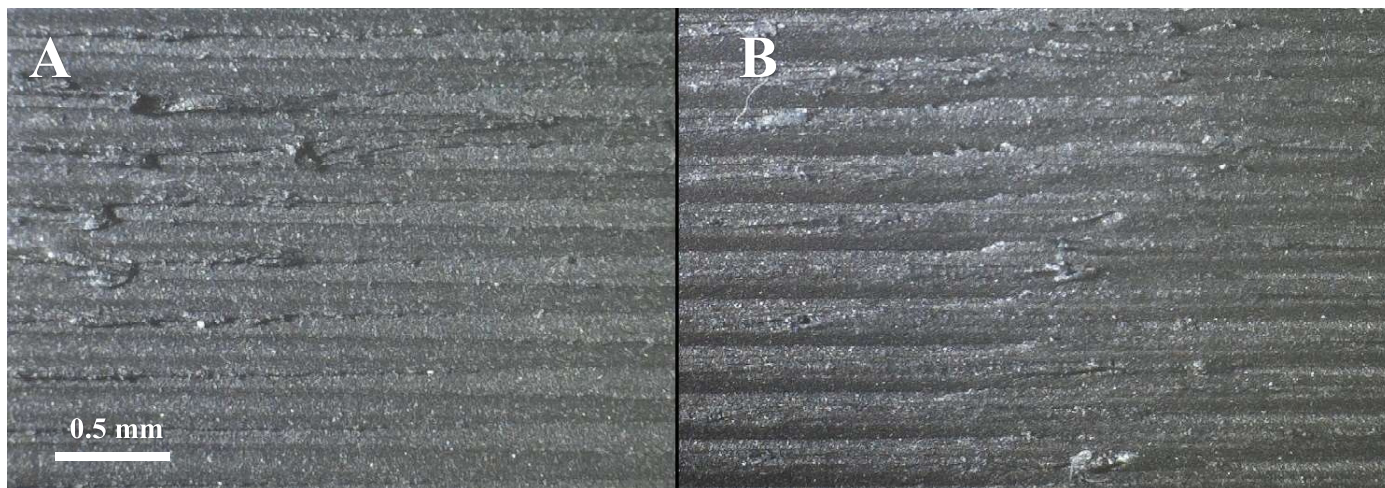
Figure 7: . Optical microscopy of new 5 wt% parallel printed samples: A) modified G-code and B) modified G-code and printing temperature.
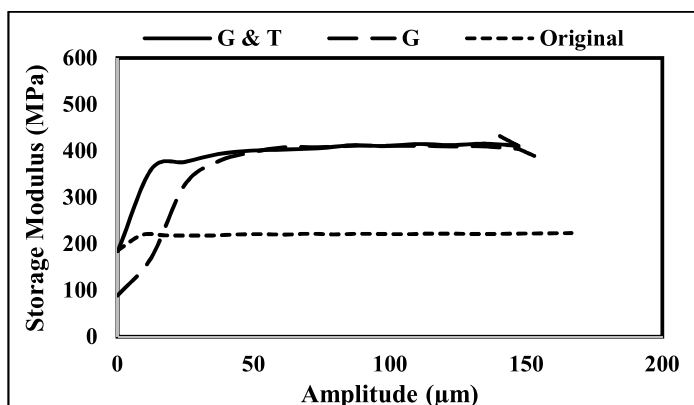
had a small influence.

Figure 8: Storage modulus as a function of amplitude for the new printed samples and the original 5 wt% parallel.

4. Conclusion

This paper focused on studying and mitigating the weakness of the popular 3D printing manufacturing method: lack of fusion, and limited materials choice for filament. Nine samples were successfully printed with 3 different directions (parallel, vertical & diagonal) and 3 different GNP contents (0, 5 and 10 wt%) in a PLA matrix. DMA results revealed that the strength of a sample depends strongly on its geometry and the location, as well as direction of the applied stress. In our case the vertical samples showed the highest storage modulus, and adding GNPs only lowered it. DMA together with optical microscopy revealed the possible phenomena of shear thinning as well as confinement of the PLA chains by the rigid GNPs, which were accounted for by printing two new samples with modified G-code (decreased filament gaps) and increased print-

ing temperature. The storage modulus for the new samples dramatically increased compared to the unmodified sample, and the extent of fusion was visually observed as well. Additionally, the thermal conductivity was measured for the parallel sample (for convenience of direction), and exhibited that increased conductivity corresponds to increased GNP content in the composite. This study shows that manipulation of properties of 3D printed samples can be achieved by small variations in the G-code, and demonstrates the importance of geometry of materials at the molecular level.

5. Acknowledgments

6. References

[1] Vincent F. Scalfani and Thomas P. Vaid. 3d printed molecules and extended solid models for teaching symmetry and point groups. *Journal of Chemical Education*, 91(8):11741180, 2014.

[2] Philip J. Kitson, Ross J. Marshall, Deliang Long, Ross S. Forgan, and Leroy Cronin. 3d printed high-throughput hydrothermal reactionware for discovery, optimization, and scale-up. *Angewandte Chemie*, 126(47):1293712942, 2014.

[3] Kaufui V. Wong and Aldo Hernandez. A review of additive manufacturing. *ISRN Mechanical Engineering*, 2012:110, 2012.

[4] Philip J Kitson, Stefan Glatzel, Wei Chen, Chang-Gen Lin, Yu-Fei Song, and Leroy Cronin. 3d printing of versatile reactionware for chemical synthesis. *Nature Protocols*, 11(5):920936, 2016.

[5] Tahseen Tabassum, Marija Iloska, Daniel Scuereb, Noriko Taira, Chongguang Jin, Vladimir Zaitsev, Fara Afshar, and Taejin Kim. Development and application of 3d printed mesoreactors in chemical engineering education. *Journal of Chemical Education*, 95(5):783790, 2018.

[6] K. Prashantha and F. Roger. Multifunctional properties of 3d printed poly(lactic acid)/graphene nanocomposites by fused deposition modeling. *Journal of Macromolecular Science, Part A*, 54(1):2429, 2016.

[7] Dingchun Zhu, Yuanyuan Ren, Guangxin Liao, Shenglong Jiang, Fenghua Liu, Jianjun Guo, and Gaojie Xu. Thermal and mechanical properties of polyamide 12/graphene nanoplatelets nanocomposites and parts fabricated by fused deposition modeling. *Journal of Applied Polymer Science*, 134(39):45332, Sep 2017.

[8] Sithiprumnea Dul, Luca Fambri, and Alessandro Pegoretti. Fused deposition modelling with absgraphene nanocomposites. *Composites Part A: Applied Science and Manufacturing*, 85:181191, 2016.

[9] Bin Zhang, Baekhoon Seong, Vudat Nguyen, and Doyoung Byun. 3d printing of high-resolution pla-based structures by hybrid electrohydrodynamic and fused deposition modeling techniques. *Journal of Micromechanics and Microengineering*, 26(2):025015, Nov 2016.

[10] Yang-Fei Zhang, Cong Zhang, and An Li. Thermal conductivity of graphene-polymer composites: Mechanisms, properties, and applications. *Polymers*, 9(12):437, 2017.

[11] CamGraph Graphene Powders. Cambridge Nanosystems: Cambridge, UK, Feb 2003. (Accessed 3 Oct 2018).

[12] DMA Q800 Specifications. *Dynamic Mechanical Analysis*. TA Instruments, 2010. (Accessed Dec 2017).

[13] Pradip Kumar, Uday Narayan Maiti, Kyung Eun Lee, and Sang Ouk Kim. Rheological properties of graphene oxide liquid crystal. *Carbon*, 80:453461, 2014.

[14] Marialaura Clausi, M. Gabriella Santonicola, and Susanna Laurenzi. Steady-shear rheological properties of graphene-reinforced epoxy resin for manufacturing of aerospace composite films. 2016.

JUCER

Effect of Graphene Nanoplatelets on Compatibility of Polypropylene and Ethylene Vinyl Acetate

Jason Peng[a], Bei Kai Huang[a], Da Qu[a], Chang Jae Yoo[a]

[a]*Department of Materials Science and Chemical Engineering, Stony Brook, NY 11794, USA*

Abstract

Polyvinyl chloride (PVC) is used worldwide as a cheap, lightweight, and strong construction and insulation material. Unfortunately, due to its need of immiscible phthalate plasticizers to increase flexibility, plasticized PVC poses a serious potential health risk if chemically degraded or improperly disposed. Polymer blends are a possible alternative to PVC, but are generally immiscible, resulting in weak mechanical and thermal stability. To improve the compatibility of immiscible polymers, compatibilizing additives are mixed with the polymers. In recent studies, graphene nanoplatelets (GNPs) have proven to be a viable compatibilizer in polymer blends, showing increases in various properties. In our study, we are examining the effect of GNPs on the compatibility of two commonly used immiscible polymers, polypropylene (PP) and ethylene vinyl acetate (EVA), though mechanical and morphological analysis. Varying compositions of PP and EVA, 20:80 EVA/PP and 30:70 EVA/PP by weight, were melt mixed with varying amounts of GNPs then mechanically tested for impact and tensile strength, followed by observed morphologically using SEM, TEM, and contact angle. For both 20:80 and 30:70 EVA/PP copolymer blends, increasing amounts of GNPs resulted in higher average tensile modulus with 20:80:1 and 30:70:10 EVA/PP/GNP having the highest increase in tensile modulus compared to the controls. For impact strength, after an initial drop in strength with the addition of GNP, the highest increase in average impact strength was observed in the 15 wt% GNP copolymers. When observed under an SEM, the copolymers depict a decrease in domain size with increasing GNP content indicating increased compatibilization between the polymers with increasing GNP. Depending on the percent of GNP added, the tensile and impact strength of our copolymers were comparable to the tensile and impact strength of PVC, proving EVA/PP/GNP copolymers to be a possible replacement to PVC.

Keywords: Electrospinning, Graphene nanoplatelets, Polymer blends, Blend Compatibility

1. Introduction

In recent years, the scientific and industrial communities have focused on developing composite materials from polymer blends in an effort to replace current industry standard of PVC. This is due to PVCs reliance on plasticizers for increased flexibility and potential release of hydrogen chloride gas and dioxin upon combustion. As a potential replacement to PVC, polymer blends have been tested in various compositions and ratios to find a combination of two or more polymers that can match the of PVCs tensile and impact resilience while maintaining flexibility without the need of added plasticizers. Unfortunately, polymer blends are generally immiscible, with reduced mechanical properties due to the phase separation cause by the large, unfavorable enthalpy of mixing [3]. To overcome immiscibility, compatibilizers have been used as a filler to increase the degree of compatibility (DoC), the measure of the strength of interfacial bonding between immiscible polymer blends, by decreasing the sizes of the phase domains, the regions of copolymers that are uniform in composition and state, present in the composite. Previous research has shown that organoclays are notable compatibilizers, effectively decreasing domain sizes

and increasing modulus[5]. In our study, graphene, which has proven to be a viable compatibilizer in the form of graphene oxide [1], is used to compatibilized EVA and PP, who immiscible polymers to form a copolymer utilizing the chemical resistance of PP and the flexibility of EVA. Previous research in the group has shown that GNP is an effective compatibilizer for blends such as Polystyrene (PS)/PMMA(poly(methyl methacrylate)) and EVA/ High Density Polyethylene(HDPE). Various copolymers composed of different composition of EVA and PP, by weight, and increasing weight percent of GNP were tested both mechanically and morphologically to calculate the change in mechanical properties and observe the change in morphology as more GNPs were introduced to the melt mix. Adhering to previous research in the group, an increase impact and tensile strength with a reduction in domain size were observed with increasing loads of GNP.

2. Experiment

2.1. Materials

The graphene nanoplatelets (GNP), xGnP C750 with an average surface area of $750 m^2$/g, were supplied by

xGSciences. Polystyrene (PS) and polypropylene (PP) were supplied by Total S.A. while Ethylene Vinyl Acetate (EVA) copolymer resin was supplied by Muehlstein.

2.2. Nanocomposite Preparation

Two different blends of PP and EVA were mixing with increasing concentrations of graphene nanoplatelets by weight. Each nanocomposite is made with the polymer blend and 0, 1, 5, 10, or 15% of the total weight in GNP. The PP and EVA polymer composites with and without graphene nanoplatelets were prepared by melt mixing in a C.W. Brabender Intelli-Torque Plastic-Corder at 180 C. Initially, approximately half of the total mass of PP and all the EVA is added to the chamber at 20 rpm. After the pellets have melted, the graphene nanoplatelets and the rest of the PP were added. The speed was raised to 100 rpm and kept for 10 minutes. The polymer blend is then removed from the chamber and cut into small pieces for hot pressure molding to fit the requirements of the mechanical tests.

2.3. Characterization Methods

2.3.1. Mechanical Tests

Izod impact tests were performed using Testing Machines Inc. Impact Tester according to the ASTM D-256 test method. Tensile properties of the nanocomposites were obtained through Instron 5542 with an extention rate of 2.0 mm/min. The measurement value of each sample represents average tests of 5 specimens.

2.3.2. Contact Angle Measurements

Graphene nanoplatelets were dissolved in DMF creating a 1mg/mL solution which was then spin casted onto Si wafers. Small pieces of EVA and PP were placed on top of separate Si wafers and then placed into a vacuum oven for 24 hours to melt and form EVA and PP droplets. The contact angle of EVA and PP droplets were observed and measured using CAM 200 optical contact angle meter (KSV Instruments Ltd). The contact angle value represents the average of five left measurements and five right measurements between two droplets of polymer.

2.3.3. Scanning electron microscopy (SEM)

The fracture surface of the nanocomposites used in impact strength tests were viewed by JEOL JSM7600F with a Schottky electron gun.

2.3.4. Transmission electron microscopy (TEM)

Cross sections of EVA/PP/GNP nanocomposites were cut by Leica UC-7 at room temperature with diamond knife. The thin films with the thickness of 80-100 nm were floated on deionized water and transferred onto copper grids. The cross sections were viewed by a JEOL JEM 1400 Transmission Electron Microscope.

3. Results and Discussions

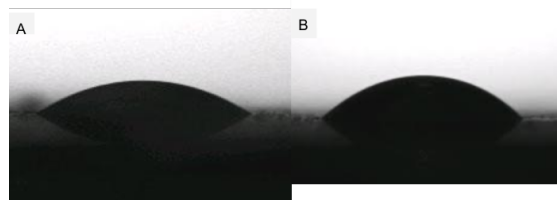### 3.1. Structure of nanocomposites

3.1.1. Graphene affinity

Figure 1: The optical images of polymer droplets on GNP: (A) EVA on GNP (B) PP on GNP.

	GNP	
Contact Angle	31.01°	23.63°
	± 4.19°	± 2.07°

Figure 2: Contact angle measurements of EVA and PP on GNP.

To determine the relative affinity of graphene to PP and EVA, contact angle measurements were performed. The contact angles of the PP and EVA droplets on GNP, shown in Figure 2, were relatively close to one another indicating that GNPs have a similar affinity for both polymers which led us to predict that the GNPs will be evenly dispersed throughout the nanocomposite. This is later confirmed by the TEM images.

3.1.2. SEM Images

Fig. 3A is of the 30/70 EVA/PP composite. The image showed distinct voids throughout the polymer matrix where the EVA domains formed and broke off during impact strength testing indicating clear phase separation between PP and EVA and a lack of interaction between the two. As the concentration of graphene is increased to 1%, the separation of EVA and PP is still distinct although the formation of linkages between the two polymers can be observed. The domain size has decreased significantly and distribution of EVA throughout the matrix became more uniform. The 15% graphene nanocomposite shown in Fig. 4C shows the covering of domain by graphene. At the same magnification in which other composites show distinct voids, these voids are no longer observable at 15% GNP and the surface seems to be one uniform phase. The lack of phase separation indicates significantly increased phase miscibility. From the 30 kX magnification of the samples in Fig. 2D and Fig. 3E, it is evident that domain size of EVA has decreased. From Fig. 3F, we see that the EVA domains we see in Fig. 3D and Fig. 3E have been eliminated and been filled with graphene. From

these observations made about SEM images, we can conclude that the presence of graphene in EVA/PP copolymer decrease domain size and phase separation between the two co-polymers.
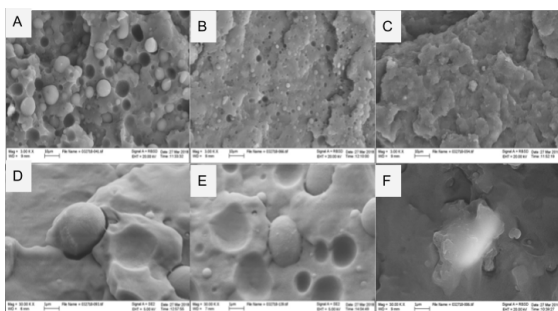

Figure 3: SEM images taken on the fracture surfaces of EVA/PP with and without graphene: (A) 20/80 EVA/PP (B) 20/80/1 EVA/PP/GNP (C) 20/80/15 EVA/PP/GNP (D) 30/70 EVA/PP (E) 30/70/1 EVA/PP/GNP (F) 30/70/15 EVA/PP/GNP)

3.1.3. TEM Images

From the TEM images, increasing phase miscibility is observed with increasing GNP concentration. When we look at the control sample of Fig. 4A, it had clear phase separation where the matrix, polypropylene and EVA acts as the domain are easily identified. As we increase the concentration of graphene, we decrease the phase separation.

Fig. 4B has concentration of 1% graphene and it shows the dispersion of graphene throughout the nanocomposite. As we increase the concentration of graphene to 15%, we can see from the TEM images, that phase separation has decreased drastically. Instead of the domains we see in 1% graphene samples, we see areas of black in 15% graphene samples which we can assume to be graphene filled domain as SEM suggested. Therefore, we can assume from the image that the sample is becoming miscible which is supported by the impact data since miscible blends exhibit mechanical properties proportional to ratio of constituents[4].

3.2. Mechanical Properties

3.2.1. Impact Resistance

From the Fig. 5, we can see with the addition of GNP, both the polymer blends suffered an initial decrease in impact strength and then increases with increasing GNP concentration. The initial drop in impact strength can be attributed to the fact that at lower GNP concentrations, the GNP were mainly dispersed in the two polymers rather than at the interface, contributing little to improving the mechanical strength of the blend. It is also possible that at low GNPs concentrations, the GNPs are not fully exfoliated inside the polymer matrix leading to the formation of cracks and micro-voids between the graphene layers, reducing mechanical strength. At 10 wt% graphene, the
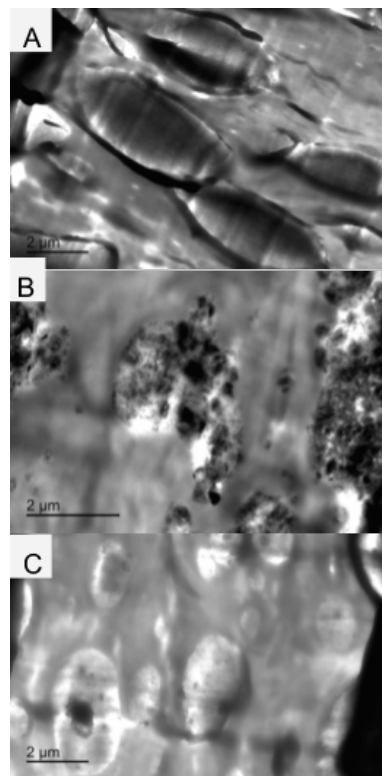

Figure 4: TEM images of the nanocomposites: (A) 30/70 EVA/PP (B) 30/70/1 EVA/PP/GNP (C) 30/70/15 EVA/PP/GNP
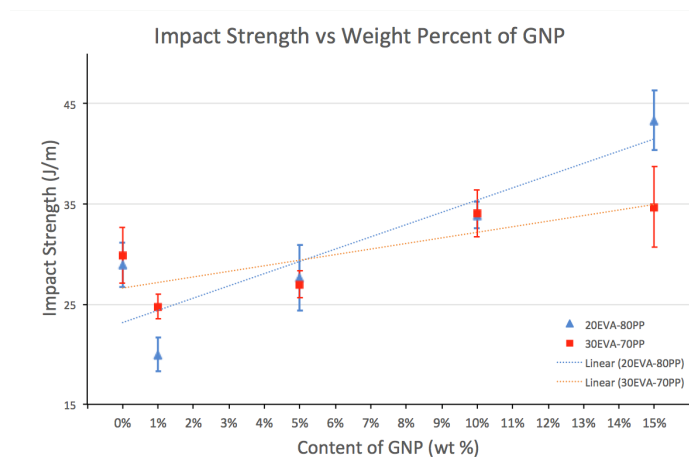
Figure 5: Impact strength of the nanocomposites with both polymer blends.

nanocomposite begins to exhibit a higher impact strength than the polymer blend without graphene.

The overall increase in impact strength can be attributed to the change in morphology of the nanocomposite with increasing graphene concentration. From Fig. 7 it can be seen that some of the graphene nanoplatelets at the interface are oriented perpendicular to the interface. Similarly, this occurred in Guos study with RDP

Material	Impact strength (J/m)	Tensile modulus (GPa)
PVC	40	1.93
20EVA/80PP	28.9 ± 2.4	1.09 ± 0.02
20EVA/80PP/1GNP	20.0 ± 1.9	1.63 ± 0.04
20EVA/80PP/15GNP	43.3 ± 3.3	1.49 ± 0.04
30EVA/70PP	29.9 ± 2.8	0.98 ± 0.02
30EVA/70PP/1GNP	24.7 ± 1.2	1.70 ± 0.04
30EVA/70PP/15GNP	34.7 ± 4.0	1.37 ± 0.12

Figure 6: Mechanical properties of nanocomposites compared to ASTM standard specifications for rigid PVC.

coated halloysite nanotubes at interface of a PLA/PBAT blend. The perpendicular orientation of the nanoparticles increases interfacial adhesion by reinforcing the interface with minimal disturbance to the chain entanglement between the two polymers[2].
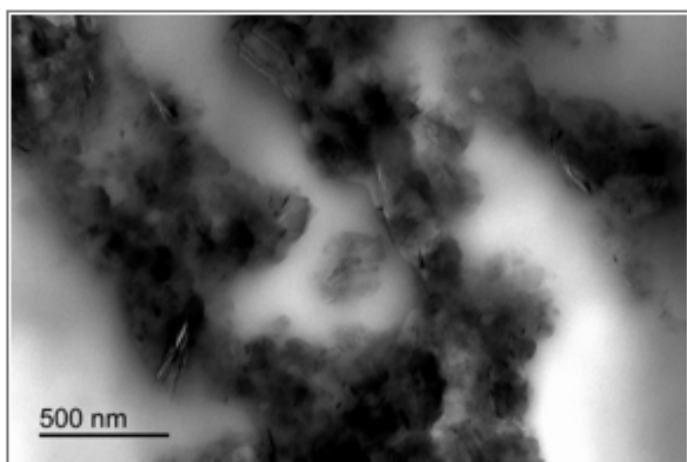

Figure 7: TEM image of the 20/80/15 EVA/PP/GNP blend.

3.2.2. Tensile Modulus

From Fig. 9, there was no observable correlation between tensile modulus and increasing concentration. However, all samples with the addition of graphene had a higher tensile modulus than without therefore we can conclude that the addition of graphene improved the tensile modulus. The lack of correlation in the tensile modulus to increasing GNP concentration can be attributed to varied breaking location of the sample. The breaking points of the testing samples varied from the neck to the center

as shown in Fig. 7. Breaks closer to the neck indicated brittleness resulting in non-correlation.
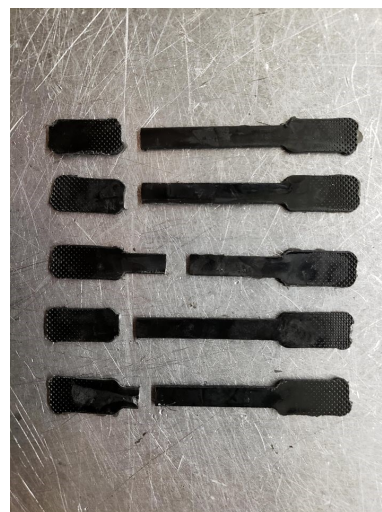

Figure 8: Various breaking points of testing samples in tensile strength tests.
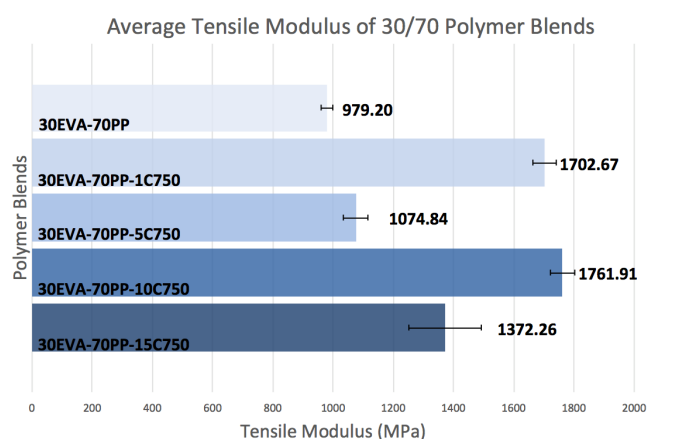
Figure 9: Average tensile modulus for nanocomposites made with the 30/70 EVA/PP polymer blend.

3.2.3. Comparison to PVC

Fig. 6 shows the impact strength and tensile modulus of various nanocomposites compared to the ASTM standard specification for rigid PVC. With the addition of GNP to the polymer blend impact strength and tensile modulus becomes comparable to PVC. The nanocomposite made from 20/80 EVA/PP and 15wt% GNP even exhibits at higher impact strength at $43.3 J/m \pm 3.3 J/m$. The mechanical properties of the nanocomposite have the potential to be altered for various purposes through change of the polymer blend composition.

4. Conclusion

We have shown with contact angle of PP/GNP and EVA/GNP that the affinity for graphene is similar between the two polymers which signifies the role of graphene as a compatibilizer in the blend. From our impact data, it is shown that impact strength increases with increasing graphene content. The highest impact strength was from the 20/80/15 EVA/PP/GNP composite, which is in agreement with the impact strength of PVC. From the tensile data, we determined that graphene enhances the tensile modulus of the composite with an error of 10%-30% to PVC in regard to the 20/80 EVA/PP blend. The TEM and SEM images show a similar trend where the addition of graphene decreases the domain size of EVA in the blend. The reduction in size of the domain is attributed to the decrease in phase separation between PP and EVA. The reduction and eventual elimination of phase separation suggests graphene increases phase miscibility of the blend. We believe that graphene is a good compatibilizer in the blend of PP and EVA because it improved the mechanical properties of the blend such as impact strength and the phase miscibility of the two polymers. Not only does it exhibit mechanical properties competitive with PVC, the composition of our polymer blend can also be altered to desired mechanical properties providing an environmentally friendly alternative to PVC.

5. Acknowledgments

6. References

[1] Cao, Y., Zhang, J., Feng, J., & Wu, P. (2011). Compatibilization of immiscible polymer blends using graphene oxide sheets. *ACS Nano*, *5*, 59205927. doi:10.1021/nn201717a.

[2] Guo, Y., He, S., Yang, K., Xue, Y., Zuo, X., Yu, Y., Liu, Y., Chang, C.-C., & Rafailovich, M. H. (2016). Enhancing the mechanical properties of biodegradable polymer blends using tubular nanoparticle stitching of the interfaces. *ACS Applied Materials & Interfaces*, *8*, 1756517573. doi:10.1021/acsami.6b05698.

[3] Higgins, J. (1990). Polymer alloys and blends: Thermodynamics and rheology. *Polymer*, *31*, 2220. doi:10.1016/0032-3861(90)90099-k.

[4] Ning, P., & Ko, T.-M. (1997). Influence of miscibility on the morphology and properties of polycarbonate/(maleic anhydride)-grafted-polypropylene blend. *Polymer Engineering & Science*, *37*, 12261237. doi:10.1002/pen.11767.

[5] Si, M., Araki, T., Ade, H., Kilcoyne, A. L. D., Fisher, R., Sokolov, J. C., & Rafailovich, M. H. (2006). Compatibilizing bulk polymer blends by using organoclays. *Macromolecules*, *39*, 47934801. doi:10.1021/ma060125.

JUCER

Fabrication of 3-Dimensional Electrospun Nanofibers with a Surfactant and its Applications in Cimex Lectularius Traps

Timothy J. Hart[a], Saeyeon Jeong[a], Justin Seetaram[a], Xianxian Chen[a], Aravindh Nirmalan[a], Shan He[a,b], Miriam Rafailovich[a]

[a]Department of Materials Science and Chemical Engineering, Stony Brook, NY 11794, USA
[b]Fibertrap LLC, Holbrook, NY 11741, USA

Abstract

Electrospinning, an electrostatic fiber fabrication technique, has evinced greater attention in recent years due to its versatility and potential for applications in diverse fields [1]. Hence, many attempts to manipulate the properties of electrospun fibers to gain beneficial effects have been made. One such property is the presence of three-dimensional structures which have been proven to be useful in targeting features on cimex lectularius, commonly known as bed bugs, by immobilizing them. Unfortunately, electrospinning solutions of neat polystyrene produces two-dimensional, flat fiber mats which are unsatisfactory for this application as it lacks entangling features [2]. However, it has been discovered that electrospinning solutions of recycled expanded polystyrene, such as foam coffee cups and boxes, produces three-dimensional fibers desirable for this application [3]. Herein, the effect of a particular additive in an otherwise pure polystyrene solution has on fiber properties is shown. This additive, a surfactant, was chosen because it is commonly used as an expanding agent in the production of expanded polystyrene. In this report it has been discovered that fibers produced using solutions of polystyrene with 0.15% (w/v) of this surfactant exhibit similar properties to those produced using solutions of recycled polystyrene. These results demonstrate how certain additives, such as this surfactant, may be useful in the production of fibers with 3-D features. In addition, a brief investigation into the use of a simplified bed bug attractant and optimal trap properties is discussed.

Keywords: Electrospinning, polystyrene, nanofibers, Cimex Lectularius, bed bug

1. Introduction

Since 2000, a resurgence of bed bug infestations in homes, hospitals, hotels, and offices has been observed [4, 5]. Accordingly, there has been an increased interest in new and effective methods of their elimination. Modern methods of bed bug eradication are notoriously challenging as insecticide resistance has been demonstrated [6]. Thus, the use of a physical trap developed herein, may be useful in the prevention and elimination of such infestations.

Electrospinning has been a longstanding method for nanofiber production. It is a simple and versatile technique that relies on the electrostatic repulsion between surface charges to continuously draw nanofibers from a viscoelastic fluid [7]. The fibers that are produced are often flat and two-dimensional. However, fluffy three-dimensional fibers are of considerable interest as their exceptional surface area to volume ratio and porosity makes them a robust and advantageous candidate for many applications including bed bug traps [8, 9]. New strides have been made in the implementation of electrospun nanofiber technology in bed bug traps where is has been demonstrated that microscopic protrusions on bed bugs legs become entangled in the three-dimensional nanofiber network.

It is known that electrospinning neat polystyrene (PS) results in flat, two-dimensional fibers [2]. However, it has demonstrated that nanofibers spun from solutions made of recycled polystyrene foam (RPS) produce three-dimensional and porous fibers [3]. When observed with the naked eye, these fibers resemble candy floss. It is hypothesized that there is a residual chemical additive used in the production of expanded polystyrene products responsible for the unique nature of nanofibers produced from such recycled products. Furthermore, this study includes the process for the optimization of trap parameters such as trap design and the selection of trap lures.

2. Experimental

2.1. Materials

Two sources of polystyrene were used in this study: polystyrene (PS) from Sigma Aldrich (typical MW = 280,000 g/mol) and recycled polystyrene foam (RPS). An undisclosed surfactant was incorporated into neat solutions of polystyrene at various concentrations.

2.2. Solution Preparation

A summary of the solutions prepared in this study are shown in Table 1. The corresponding amount of surfactant

and polystyrene were measured using a digital balance and placed into a glass vial. Next, a 50:50 mixture of tetrahydrofuran (THF) obtained from Fisher Chemical and N,N-dimethylformamide (DMF) obtained from Sigma Aldrich was added to the vial to create a 15% (w/v) polystyrene solution. Solutions were stirred using a magnetic stir plate for 30 minutes. After stirring, the vial was sealed with a plastic paraffin film to prevent evaporation. Solutions were left to sit in a warm environment (approximately 40 °C) for 24 hours after which the solutions would appear homogeneous.

Table 1: Summary of solutions prepared.

Sample	PS Type	Surfactant Conc. (w/v) (%)
A	PS	0.00%
B	RPS	0.00%
C	PS	0.10%
D	PS	0.15%
E	PS	0.50%
F	PS	0.75%
G	PS	1.50%

2.3. Electrospinning

The electrospinning apparatus is schematically shown in Figure 1. For the electrospinning process, polymer solutions were loaded into a syringe equipped to a 14 gauge stainless steel needle with a nominal inner diameter of 1.6 mm. Randomly oriented nanofibers were electrospun by applying a voltage of 15 kV between the needle and the aluminum foil plate collector using a high voltage power supply (Gamma High Voltage Research). The grounded plate collector was located at a distance of 15 cm and the polymer solution was pumped at a rate of 15 mL/h by a syringe pump (Scientific Lab Supply). Electrospun fibers were collected and stored in sealed petri dishes.
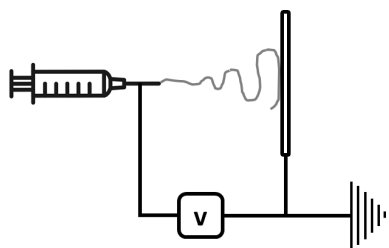

Figure 1: Schematic of electrospinning process.

2.4. Optical Microscopy

Optical microscopy was performed using an Olympus BH2 equipped with an Olympus BH2-UMA illuminator and Omax A35180U3 digital camera. Images of nanofibers made with solution samples A-G were taken at 5x and 50x magnification.

2.5. Scanning Electron Microscopy

Scanning Electron Microscopy (SEM) was carried out using a LEO-1550 SPEG Gemini microscope equipped with a high energy Robinson Backscatter detector (RBSD).

To aid in the identification of a possible chemical additive present in RPS responsible for the observed difference in nanofiber structure, the elemental composition of a PS and RPS films created by spin coating solutions on a silicon wafer was determined by energy dispersive X-ray spectroscopy (EDX) (EDAX company) equipped in the same SEM system. Samples were captured at 5kV and analyzed using software from IXRF systems.

2.6. Curvature Study

It is theorized that a high degree of fiber curvature corelates to the three-dimensionality observed in RPS nanofiber networks. Due to the inability of electrospun nanofibers to discharge quickly, electrical charges present are believed to cause a slight repulsion between strands, thus giving the nanofibers a fluffy and 3-dimensional curved structure. The bending energy, or the energy stored in a fiber's shape, plays a prominent role in determining the modulus of the electrospun fiber. To quantify this, the parameter stiffness ratio (SR) is used. Stiffness ratio is defined as the ratio of Youngs moduli for a single curved fiber (E_{cf}) to that of a straight fiber (E_f). Stiffness ratio can be calculated trivially if R (fiber radius) and r_0 (average distance between junctions) are assumed to be independent to d (fiber diameter) [10]. Equation 1 shows how to calculate stiffness ratio.

$$\frac{1}{SR} = \frac{E_f}{E_{cf}} = A \times \frac{1}{d^2} + B \tag{1}$$

Where,

$$A = \frac{8R^3}{\frac{r_0}{2}} \arcsin\left(\frac{\frac{r_0}{2}}{R}\right) - 24R\sqrt{R^2 - (\frac{r_0}{2})^2}$$
$$+ \frac{16(R^2 - (\frac{r_0}{2})^2)R}{\frac{r_0}{2}} \arcsin\left(\frac{\frac{r_0}{2}}{R}\right)$$

$$B = \frac{R}{2(\frac{r_0}{2})} \arcsin\left(\frac{\frac{r_0}{2}}{R}\right) + \frac{\sqrt{R^2 - (\frac{r_0}{2})^2}}{2R}$$

Using this method, it is expected that three-dimensional fiber networks would exhibit a smaller stiffness ratio compared to two-dimensional fiber networks.

2.7. Zeta Potential

Zeta potential analysis was performed using a Nanobrook Omni with a precision of ±3%. Nanofibers were pulverized in a pestle and mortar until a fine powder was formed. This powder was well-mixed with deionized water and placed in a cuvette. By using the Positron Annihilation Lifetime Spectroscopy (PALS) technique, electric fields as small as 1 or 2 V/cm produced enough solids movement to register a reading [11].

2.8. Bed Bug Experiments

Several live bed bug tests were performed to optimize trap parameters including trap design, trap color, attractant used, and attractant concentration. Attractants used are not disclosed in this report. All traps used in these experiments were of the same dimensions (3 in x 3 in x 0.5 in). One trial per experiment was performed, thus an estimation of observational error was used.

Experiment 1 was designed to determine if bed bugs would have a preference for one of two available cardstock trap colors: brown or black. 10 bed bugs each were dropped into individual one-quart plastic containers into which a trap without fibers or attractants was placed. The number of times a bed bug entered the trap was tallied for one hour. The parameters for this experiment are summarized in Table 2.

Table 2: Summary of experiment 1 parameters used to determine best trap color.

Group	Trap Color
I	Brown
II	Black

Experiment 2 was designed to determine effective attractants for use in the trap. For each group, a total of 2 mg of each attractant was placed on top of the trap. 10 bed bugs each were dropped into individual one-quart plastic containers into which a brown trap loaded with nanofibers created from RPS was placed. At the end of three hours, the number of bed bugs trapped in the fibers was recorded. Bed bugs were considered trapped if they were completely entangled and and immobilized by the fibers.

Table 3: Summary of experiment 2 parameters used to determine best attractants.

Group	Attractant
III	None
IV	Attractant #1
V	Attractant #2
VI	Attractant #3

Lastly, experiment 3 was designed to determine optimal concentrations of attractants. First, 2 mg of Attractant #1 was placed on top of each trap. Varying amounts of Attractant #3 was then also placed on the top of each trap as summarized in Table 4. 10 bed bugs each were dropped into one-quart plastic containers into which a brown trap loaded with nanofibers created from RPS was placed. At the end of three hours, the number of bed bugs trapped in the fibers was recorded. Bed bugs were considered trapped if they were completely entangled and and immobilized by the fibers.

Table 4: Summary of experiment 3 parameters used to determine optimal attractant concentration.

Group	Attractant #3 Dosage
VII	1 mg
VIII	2 mg
IX	3 mg
X	4 mg

3. Results and Discussion

3.1. Nanofiber Characterization

3.1.1. Energy dispersive X-ray spectroscopy

Results for RPS and PS films observed using energy dispersive X-ray spectroscopy are displayed in Figure 2. The silicon (Si) peaks are a result of the silicon wafer substrate and the carbon (C) peaks are caused by the presence of polystyrene. Thus, no abnormal elemental peaks were observed. From this came the conclusion that the presence of a residual chemical additive in RPS may be in such low concentrations that it was undetectable using this equipment.
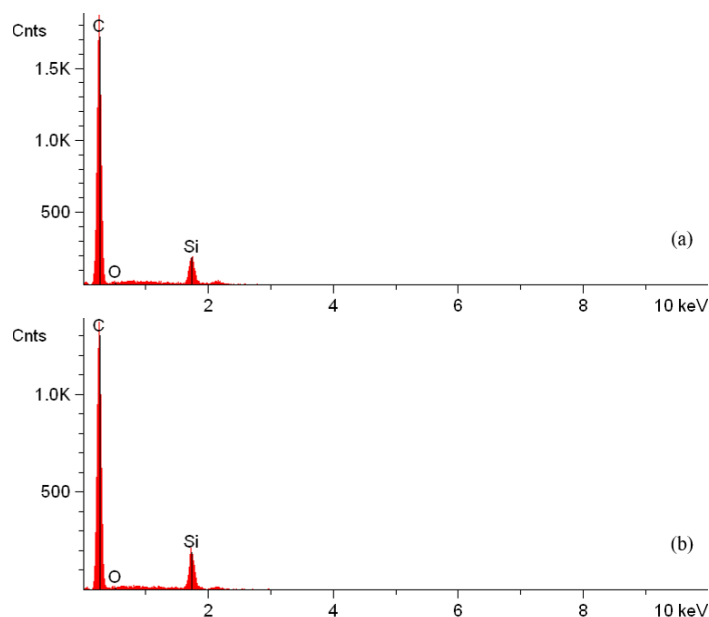

Figure 2: (a) RPS and (b) neat PS film EDX 5kV.

3.1.2. Optical Microscopy

Figures 3 and 4 show nanofiber samples A-G under an optical microscope at 5x and 50x magnification, respectively. From figures 3 and 4 it can be observed that fibers were formed for all electrospun samples. However, only PS with 0.15% surfactant exhibited the fluffy three-dimensional appearance as the RPS did with 0.00% surfactant. PS with 0.10%, 0.50%, 0.75%, and 1.50% surfactant produced fibers which appeared to melt into the aluminum

substrate. For the remainder of this study, only solutions of neat PS, RPS, and PS with 0.15% surfactant were analyzed.
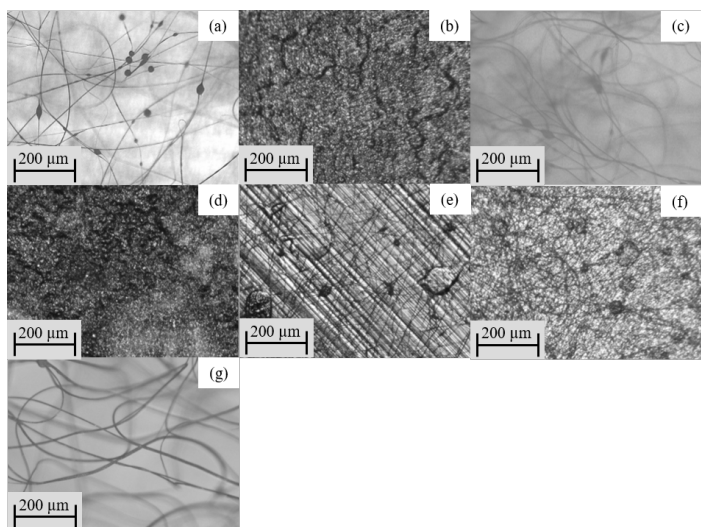

Figure 3: Optical microscope images (x5 magnification) of 15% PS with: (a) 0.00%, (b) 0.10%, (c) 0.15%, (d) 0.50%, (e) 0.75%, and (f) 1.5% surfactant; (g) shows 15% RPS with 0.00% surfactant.
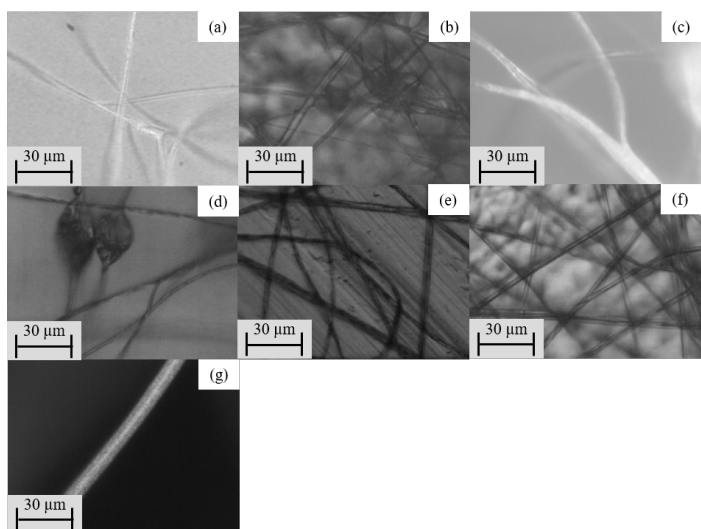

Figure 4: Optical microscope images (x50 magnification) of 15% PS with: (a) 0.00%, (b) 0.10%, (c) 0.15%, (d) 0.50%, (e) 0.75%, and (f) 1.5% surfactant; (g) shows 15% RPS with 0.00% surfactant.

3.1.3. Scanning Electron Microscopy

Fibers electrospun with neat PS, RPS, and PS with 0.15% surfactant were analyzed under a scanning electron microscope. Figure 5 and 6 shows these results for 1000x and 3000x magnification, respectively. Electrospun solutions of (a) neat PS produced fibers with many large bead structures. In contrast, solutions of (b) RPS and (c) PS with 0.15% surfactant produced significantly less bead

structures. Compared to the other solutions, solutions of PS with 0.15% surfactant appear wavy. Notice that fibers in (b) and (c) are considerably more curved compared to (a). From figures 5 and 6, average fiber diameter and junction distance was determined. Figure 7 shows the average fiber diameter for fibers analyzed under SEM.
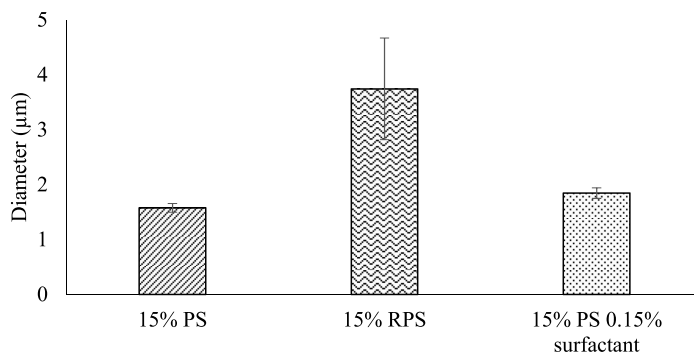

Figure 7: Average diameter of fibers.

It is observed that fibers made with RPS posses a significantly larger diameter compared to fibers made with neat PS and PS with 0.15% surfactant. Fibers made with neat PS and PS with 0.15% surfactant exhibit similar fiber diameters. Figure 8 shows the average junction distance for fibers analyzed under SEM.
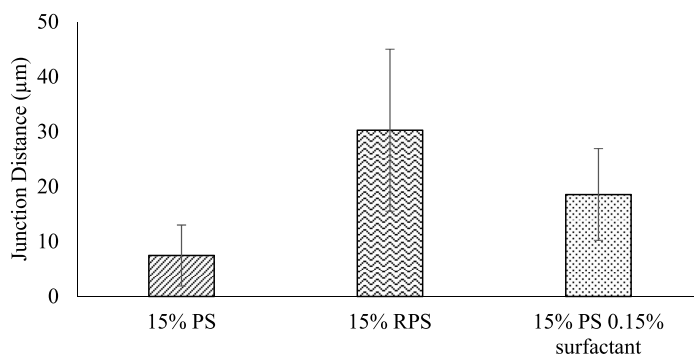

Figure 8: Average junction distance of fibers.

From figure 8 it is observed that fibers made from PS with 0.15% surfactant exhibit a statistically similar average junction to fibers made from PS and RPS. Furthermore, fibers made from RPS are statistically larger than fibers made from PS.

3.1.4. Curvature Study

As mentioned in §2.6, the degree and nature of the curvature observed in these fibers is believed to be correlated to a nanofiber networks' three-dimensional structure. To measure the stiffness ratio of nanofibers, average fiber diameter (d), fiber radius (R) and distance between junctions (r_0) was measured using SEM images. Figure
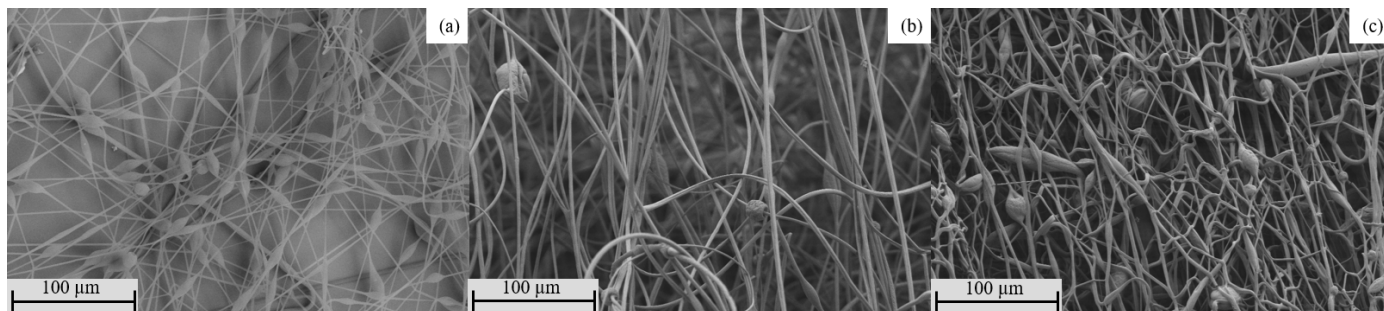
45

Figure 5: SEM images captured using RBSD of: (a) neat PS, (b) RPS, and (c) PS with 0.15% surfactant at 1000x magnification.
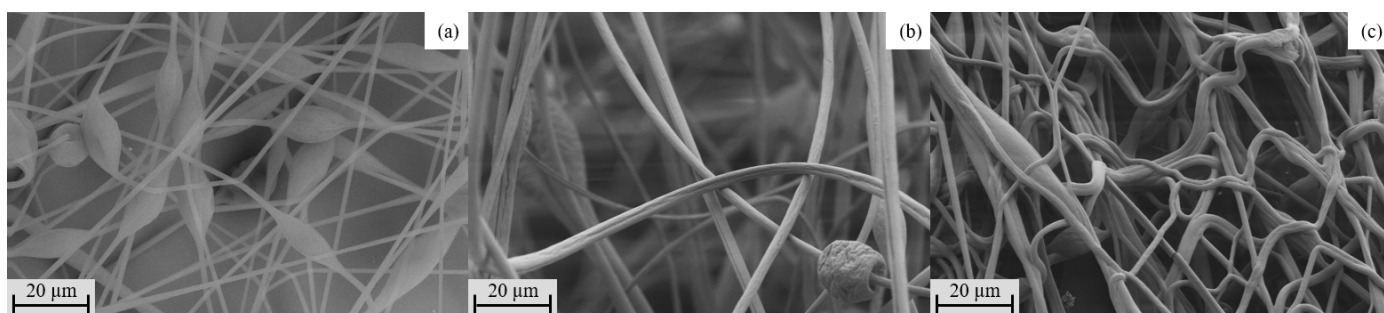

Figure 6: SEM images captured using RBSD of: (a) neat PS, (b) RPS, and (c) PS with 0.15% surfactant at 3000x magnification.

9 compares the calculated stiffness ratio for fibers electrospun from solutions of neat PS, RPS, and PS with 0.15% surfactant.
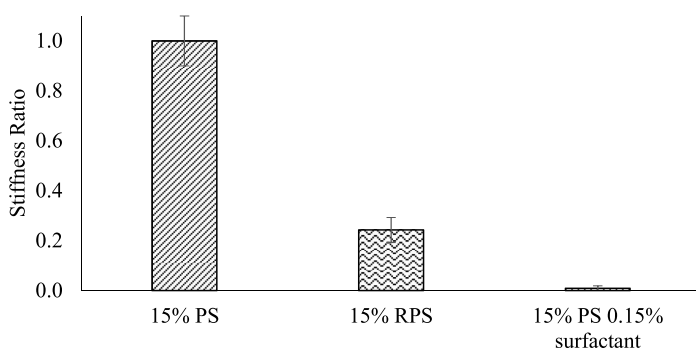

Figure 9: Stiffness ratio of fibers.

The stiffness ratio of fibers made from RPS and PS with 0.15% surfactant are significantly lower compared to fibers made from neat PS. Fibers made from PS with 0.15% surfactant posses a stiffness ratio close to zero—many times less than that of fibers made with RPS.

3.1.5. Zeta Potential

To quantify the presence of surface charges, zeta potential was measured for fibers electrospun with RPS and PS with 0.15% surfactant. Fiber particles have a small surface charge that attracts a thin layer of ions of opposite charge to the particle surface, enabling for a small reading. This double layer of ions travels with the particles as it diffuses throughout the solution. The electric potential at the boundary of the double layer was determined and the results are shown in figure 10.
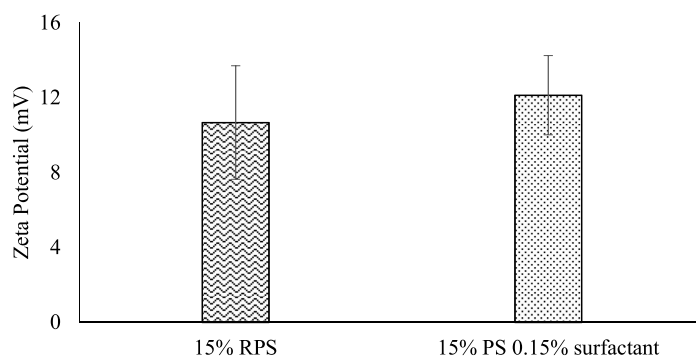

Figure 10: Zeta potential of 15% RPS and 15% PS 0.15% surfactant.

The zeta potential results indicate that fibers made from PS with 0.15% surfactant have a similar level of surface charges compared to fibers made from RPS.

3.2. Bed Bug Trap Optimization

3.2.1. Trap Color

Experiment 1 was conducted to determine if bed bugs would have a preference for one of two available cardstock

trap colors: brown or black. Figure 11 displays the results of experiment this experiment.
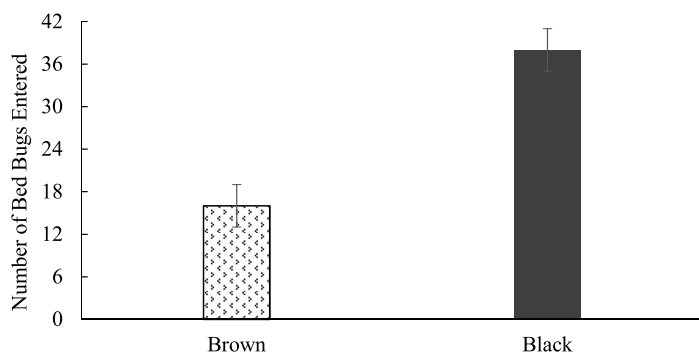

Figure 11: Number of bed bugs entering each trap color.

Between the black and brown colored boxes, the black colored box was found to be the more effective candidate as it exhibited two times more activity compared to the brown trap over a period of one hour.

3.2.2. Attractant Used

Results from experiment 2 (figure 12) confirm the value of investing in attractants for luring bed bugs. After an hour of testing, the control trap caught zero bed bugs. The addition of attractants successfully lured bed bugs to the trap causing them to become entangled within the nanofiber networks. Attractant #3 exhibited the best capture rate among all 3 chemical lures used.
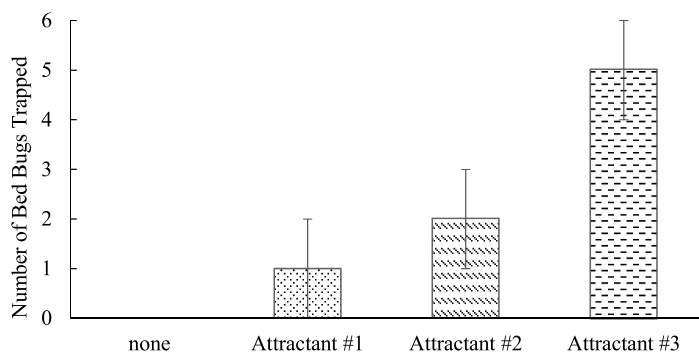

Figure 12: Number of bed bug caught in traps loaded with attractants.

3.2.3. Attractant Concentration

The best candidate from the previous experiment (Attractant #3) was then tested to determine its optimal concentration in a trap. The results for experiment 3 are shown in figure 13. Out of the four dosages used, 2 mg, 3 mg and 5 mg of Attractant #3 trapped the same number of bed bugs. After 2 mg of Attractant #3, the effectiveness appears to level off.
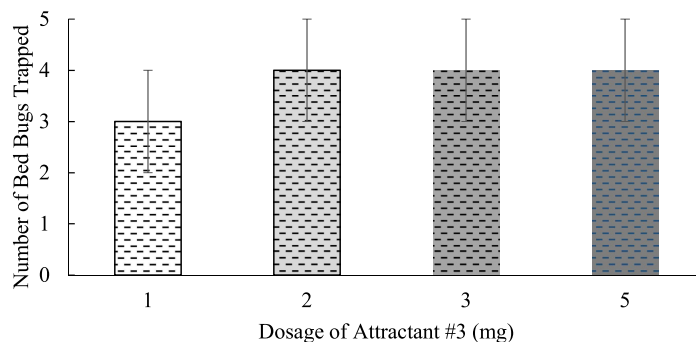

Figure 13: Number of bed bugs trapped in traps loaded with varying concentration of attractant #3.

4. Conclusion

The surfactant used in this study, when added to a solution of neat PS, produced a solution that when electrospun, would generate fluffy three-dimensional fibers successfully resembling fibers electrospun with RPS. Specifically, such fibers were produced with the surfactant concentration of 0.15%. When solutions of PS with surfactant were electrospun at other concentrations, fiber quality was poor. This indicates that the optimal concentration range of this surfactant to produce such fibers is narrow. Additional work is required to identify this range. Additionally, while fibers made with 0.15% surfactant and fibers made from RPS shared similar structures, rendering both fibers of identical properties requires further study. With regards to the bed bug experiments, results indicate that a black cardstock trap using Attractant #3 at 2 mg as the main lure proves to be most effective.

This study brings electrospinning of nanofibers for the purposes of producing effective bed bug traps a step closer to commercialization by eliminating reliance on expanded polystyrene products made with trade secrets.

5. Acknowledgments

6. References

[1] Nandana Bhardwaj and Subhas C. Kundu. Electrospinning: A fascinating fiber fabrication technique. *Biotechnology Advances*, 28(3):325 − 347, 2010.

[2] Nele Daels, Sander De Vrieze, Bjorge Decostere, Pascal Dejans, Ann Dumoulin, Karen De Clerck, Philippe Westbroek, and Stijn W.h. Van Hulle. The use of electrospun flat sheet nanofibre membranes in mbr applications. *Desalination*, 257(1-3):170176, 2010.

[3] Changyun Shin and George G. Chase. Nanofibers from recycle waste expanded polystyrene using natural solvent. *Polymer Bulletin*, 55(3):209215, 2005.

[4] S. L. Doggett, D. E. Dwyer, P. F. Penas, and R. C. Russell. Bed bugs: Clinical relevance and control options. *Clinical Microbiology Reviews*, 25(1):164192, Jan 2012.

[5] Changlu Wang, Wan-Tien Tsai, Richard Cooper, and Jeffrey White. Effectiveness of bed bug monitors for detecting and trapping bed bugs in apartments. *Journal of Economic Entomology*, 104(1):274278, Jan 2011.

[6] Alvaro Romero, Michael F. Potter, Daniel A. Potter, and Kenneth F. Haynes. Insecticide resistance in the bed bug: A factor in the pests sudden resurgence? *Journal of Medical Entomology*, 44(2):175178, Jan 2007.

[7] Jayesh Doshi and Darrell H. Reneker. Electrospinning process and applications of electrospun fibers. *Journal of Electrostatics*, 35(2):151 – 160, 1995.

[8] Yanzhong Zhang, Hongwei Ouyang, Chwee Teck Lim, Seeram Ramakrishna, and Zheng-Ming Huang. Electrospinning of gelatin fibers and gelatin/pcl composite fibrous scaffolds. *Journal of Biomedical Materials Research*, 72B(1):156165, 2004.

[9] Andreas Greiner and Joachim H. Wendroff. Electrospinning: A fascinating method for the preparation of ultrathin fibers. *ChemInform*, 38(42), 2007.

[10] Chia-Ling Pai, Mary C. Boyce, and Gregory C. Rutledge. On the importance of fiber curvature to the elastic moduli of electrospun nonwoven fiber meshes. *Polymer*, 52(26):61266133, 2011.

[11] Brian J. Kirby and Ernest F. Hasselbrink. Zeta potential of microfluidic substrates: 2. data for polymers. *Electrophoresis*, 25(2):203213, 2004.

JUCER

Investigation of mTG Crosslinked Gelatin Pluronic F127 Hydrogels for Use in a Novel Vascular Graft

Samantha Blaine[a], Jenna Mallon[a], Denny Wang[a], Arthur Ronne[a], Juyi Li[b], Gurtej Singh[b]

[a]*Department of Materials Science and Chemical Engineering, Stony Brook, NY, 11794, USA*
[b]*Department of Plastic Surgery, Stony Brook University School of Medicine, NY, 11794, USA*

Abstract

The current optimal method for long-term revascularization of blood vessels experiencing stenosis or occlusion is a vascular grafting surgery. Research into developing tissue-engineered vascular grafts that have patency rates meeting or exceeding that of autologous vessels is important for decreasing dependency on the harvest of autologous vessels. Gelatin alone does not display the necessary mechanical properties to be used in a vascular graft, but through both chemical and physical crosslinking these properties can be improved. When mixed with gelatin, microbial transglutaminase (mTG), a common enzymatic crosslinker, forms covalent bonds between the gelatin molecules. Physical crosslinking can be achieved through the addition of Pluronic F127, which exhibits reverse thermal gelation. This study aims to investigate the mechanical properties of hydrogels made from varying concentrations of gelatin, mTG, and Pluronic F127, with hopes of finding a material suitable for use in a vascular graft. Gels were prepared with either 9.0 %w/v or 13.5 %w/v Type A gelatin, varying concentrations of Pluronic F127, and were subsequently crosslinked over a 24-hour period with mTG concentrations ranging from 0.1 %w/v to 1 %w/v. Gel samples were tested for various mechanical properties including Young's modulus and suture retention strength. Statistical T tests were performed, and linear regression models were created to determine a relationship between the concentrations of gelatin, Pluronic F127, and mTG and their effect on the mechanical properties. Results indicate that the addition of Pluronic F127 had mixed effects on the mechanical properties, increasing both Young's modulus and suture retention strength at lower concentrations of gelatin while having minimal to negative effects at higher concentrations of gelatin. A gel composed of 13.5 %w/v gelatin with no Pluronic F127 crosslinked with 1 %w/v mTG exhibited the best mechanical strength out of all the gels tested. Investigation into the surface roughness of the gels and results from preliminary cell culture work indicate that proliferation of cells is possible on all concentrations of Pluronic F127 tested. From these results, we do not believe that the addition of Pluronic F127 is an optimal choice for a hydrogel to be used in a vascular graft.

Keywords: Pluronic F127, Gelatin, Microbial Transglutaminase, Hydrogel, Rheology, Vascular Graft, Suture Retention, Cell Adhesion

1. Introduction

Hydrogels are hydrophilic polymer networks that have been investigated widely for their use in tissue engineering, and, more specifically, vascular grafts. There are two main varieties of hydrogels: physical or reversible hydrogels that are held together by physical interlocking of materials, and chemical or permanent hydrogels that result from covalent crosslinking of materials. Hydrogels also have the unique capability to absorb quantities of water equivalent to thousands of times their dry weight [1]. Gelatin is formed from the hydrolysis of collagen and can form hydrogels when it is mixed in water below 30 °C. At temperatures above 30 °C, gelatin molecules are random coils, but once cooled the coils arrange into triple helices and stabilizing hydrogen bonds form between chains of molecules. This phenomenon results in the formation of a gel.

Due to the fact that these hydrogen bonds break down once heated, gelatin hydrogels alone do not display sta-

bility or sufficient mechanical strength, therefore chemical crosslinking is usually employed to improve the strength of the gels [2]. Microbial transglutaminase (mTG) is a non-cytotoxic enzyme found naturally in many plants and animals. It is also approved by the US Food and Drug Administration (FDA) for human consumption [3]. mTG is an enzymatic crosslinker that catalyzes an acyl-transfer reaction between the side chains of glutamine residues and lysine residues in gelatin to form chemical bonds between molecules of gelatin in the form of ϵ-(λ-glutaminyl) lysine [4]. Thus, the action of mTG creates a covalently linked network of gelatin which can remain stable at physiological temperatures.

Triblock copolymers of poly(ethylene oxide)-poly(propylene oxide) -poly(ethylene oxide), also known as Pluronics, exhibit reverse thermal gelation. At room temperature, Pluronics form micelles in the aqueous phase, but once heated to biological temperatures the materials tend to form gels. There are numerous va-

rieties of Pluronics available depending on the chain lengths, molecular weight, and ratio of ethylene oxide and propylene oxide [5]. Pluronic F127 is a variety which consists of 70% ethylene oxide and 30% propylene oxide [6]. When combined with gelatin, Pluronic F127 forms a physically crosslinked structure that has the ability to slow the transition of gelatin to a solution at physiological temperatures [7].

Cardiovascular diseases are the leading cause of death worldwide, resulting in a widespread desire to research artificial vascular grafts. In order to be suitable for *in vivo* transplant, grafts must be able to withstand the pressure of blood flow without bursting or experiencing significant damage or deformation, and they should be resistant to thrombosis. Thrombosis promotion may be reduced by minimizing pressure drop of the blood through the graft, increasing elasticity, and by the presence of endothelial cells on the interior surface of the graft. Additionally, the graft should not trigger an immune response such as inflammation and should be non-cytotoxic. In order to be marketable, the graft should have the mechanical strength to be manipulated and sutured by surgeons, and it should be able to be produced in large quantities in a reasonable timeframe and at a reasonable cost [8].
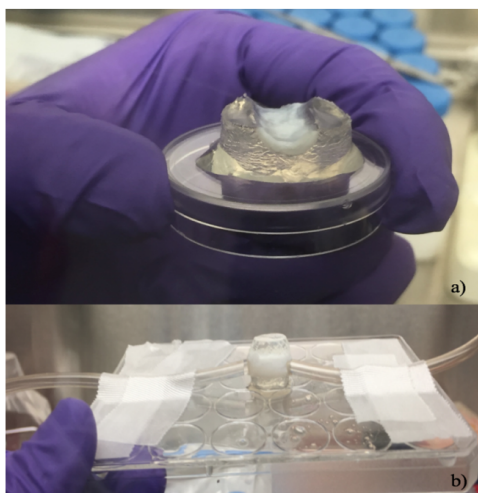

Figure 1: a) A half lumen composed of gelatin with a fibrin coating. b) Two half lumens connected to form a vascular graft.

Previous work has been done to develop a novel method of creating a graft by creating two half lumens composed of gelatin and joining them together with a fibrin sealant. This method allows cells to be seeded more easily onto the half lumens and allows for layering of different materials. Figure 1 shows a half lumen made from gelatin with a fibrin layer on top, and then the subsequent graft constructed by connecting the two half lumens.

Due to its previously described poor mechanical properties, gelatin alone is not strong enough to be employed as a vascular graft. We propose that the combination of physical and chemical crosslinking by the addition of both mTG and Pluronic F127 will lead to a material that is viable for use in a vascular graft. In order to explore this proposal, we plan to produce hydrogels in varying concentrations of gelatin, Pluronic F127, and mTG, and test the mechanical properties of the gels. Rheology will be performed to determine the Young's modulus and failure stress, while an Instron will be used to determine the suture retention strength. Additionally, we will investigate the ability of the gels to foster cell growth and proliferation by both analyzing the surface roughness and performing cell culture studies. Our goal is to determine if varying the ratios of the materials has an effect on the previously stated properties, and if so, to derive relationships between the materials and their respective effects.

2. Methodology

2.1. Chemicals and Materials

Pluronic® F127 and Type A Bloom 300 Gelatin were acquired from Sigma Aldrich, mTG was acquired from Ajinomoto Food, and deionized (DI) water was obtained by autoclave. All weighing was done using a Sartorius Quintix 313-1S Analytical Balance (Max = 310 g, d = 0.001 g) and the incubator was a Sanyo Incu Safe MCO-5M O_2/CO_2 incubator. Stock solutions of gelatin, mTG, and Pluronic F127 were made by measuring out the required amount of the material, in order to get the required percent weight/volume and mixing it with DI water. Gelatin stock solutions were made in advance and allowed to homogenize in a water bath at 65 °C for one hour. mTG stock solutions were made fresh each time they were required and placed in a water bath at 37 °C for 10 minutes prior to use in order to bring the enzyme within its optimal range of activity. Pluronic F127 must be made the previous day and be refrigerated overnight in order for the solution to homogenize.

2.2. Making Hybrid Gels

All gel compositions were made by weight/volume percentages. mTG crosslinked gelatin Pluronic F127 hydrogels were made by first mixing the required proportion of gelatin stock solution (at 63 °C) and Pluronic F127 stock solution (at 4 °C) and placing the mixture in a hot water bath at 63 °C for 10 minutes so that a homogeneous solution forms. Next, the solution was cooled to 37 °C so that mTG can be added without risk of denaturing the enzyme. Once a temperature of 37 °C was achieved, mTG stock solution was added and 2 ml of the mixture was immediately transferred to wells of a 12 well plate. The gels were then incubated at 37 °C for approximately 24 hours so that crosslinking may occur. After 24 hours have passed, the gels were heated at 65 °C for 10 minutes in an oven in order to denature the mTG enzyme. Gels were then swelled with DI water and covered with parafilm wrap until tests were ready to be performed. Table 1 reflects the different types of gels that were made. For samples that did not

Table 1: Compositions of the different gel samples made for our study.

Gel Name	%w/v Gelatin	%w/v Pluronic F127	%w/v mTG
1	13.5	0	0
2	13.5	0	1
3	13.5	5	0
4	13.5	7	0
5	13.5	5	0.1
6	13.5	7	0.1
7	13.5	5	1
8	13.5	7	1
9	9	0	0.67
10	9	3.33	0.67
11	9	5	0.67
12	9	6.67	0.67

Figure 2: The above image shows a sutured gel being tested using the Instron 5542. The white arrows point to the sutures attached to each end of the gel which are held by the clamps. As the Instron pulls on the sutures, the gel begins to break.

contain mTG, the same procedure was followed, except the gels were not incubated or swelled with DI water.

2.3. Rheological Testing

Rheological testing of the hybrid gel samples was conducted on a Bohlin Gemini HR nano Rotonetic Drive Z Rheometer at a frequency of 1 Hz. Samples crosslinked with mTG were run at a constant temperature of 37 °C, while the other samples not crosslinked with mTG were run at a constant temperature of 23 °C to prevent the gelatin from liquifying. Each sample was loaded into the machine, and the gap distance was adjusted such that the thrust on the gels was positive. Measurements of displacement, stress, and elastic modulus were taken. The measurements of stress were plotted against displacement in order to determine the Young's modulus of the gels. Five to six gels of each composition were tested, and the results were compared.

2.4. Mechanical and Suture Retention Testing

Suture retention strength was tested on the gel samples using an Instron 5542. Gels were sutured on each end using an Ethilon size 6-0 needle with a polypropylene suture. The sutures were made by inserting a suture-threaded needle approximately 3-5 mm from the outer edge of the gel, pulling through, and then making a loop large enough to be held by the clasps of the Instron. The loop is secured through instrument tying with at least three alternating throws of the surgeon's knot. It was not possible to perform this test with only one side sutured because the pressure clasp of the Instron compressed the gels, damaging them in the process. This setup is shown in Figure 2. Force was applied in the upward direction until the suture was pulled through the gel.

2.5. Surface Roughness Testing

Surface roughness of the samples was analyzed using a Keyence VK-X100 series laser scanning confocal microscope. The gels were loaded into the microscope and then scanned with the microscope's lasers in order to obtain pictures of their surfaces. Values, including the arithmetic mean height and maximum height, were also determined from micrographs.

2.6. Cell Adhesion and Proliferation Testing

Sterile gels were made in order to perform cell adhesion and proliferation testing. In order to be sterilized, the stock solutions and autoclaved DI water were filtered using a 0.22 μm mesh filter. Instead of swelling the gels in DI water, the gels were placed in EGM-2 Bulletkit media (acquired from Lonza), and the medium was replaced every 30 minutes for 3 hours. The endothelial cells were plated on the gels after 24 hours of swelling in the media. After 5 days of incubation in a 37 °C/5% CO_2 incubator, the cells were fixed with 10% formalin. Images were taken using a Nikon Upright Confocal Microscope.

3. Results and Discussion

3.1. Rheology Results

Testing on the Bohlin Gemini HR nano Rotonetic Drive Z Rheometer was done on each of the samples in order to determine elastic modulus. Elastic modulus, or Young's modulus, is an indicator of a material's elasticity and is calculated by the slope of the stress vs. strain graph [9]. A higher Young's modulus is favorable in mimicking the properties of an autologous blood vessel. Gels were tested at 37 °C in order to simulate physiological temperatures. A statistical T test was performed on groups of samples for which only one variable was manipulated in order to determine if there was a significant difference in the elastic modulus as a result of the manipulation.

Gels without mTG crosslinking were unable to remain in a solid phase and transitioned to a liquid when warmed to 37 °C. Therefore, rheology was performed on gels 1, 3, and 4 at a room temperature of 23 °C. This lack of stability at higher temperatures is likely due to the lack

of chemical bonds between strands of gelatin. These gels liquefy at the physiological temperature of 37 °C, therefore these materials cannot be used *in vivo*.

The mTG enzyme is responsible for creating the covalently linked network of gelatin which can remain stable at physiological temperatures. In the absence of mTG, these chemical bonds are not formed, and gelatin solutions are less stable at increasing temperatures.
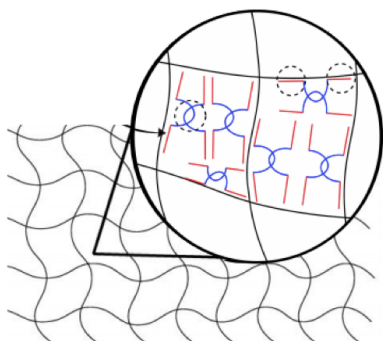

Figure 3: A proposed arrangement of gelatin and Pluronic F127 in a hydrogel, reprinted from Li, et al. [10]. The crosslinked gelatin matrix is represented in black, the PEO chains of Pluronic F127 are represented in red, and the PPO regions of Pluronic F127 are represented in blue.

Pluronic F127 lacks the λ-carboxamide group of glutamine and the ϵ-amino group of lysine that would make it a substrate of mTG. It is likely then that mTG does not catalyze the formation of chemical bonds between gelatin and Pluronic F127 or between two or more molecules of Pluronic F127. The increased stability that resulted from the addition of Pluronic F127 to hydrogels with lower concentrations of gelatin and mTG is likely due to the physical arrangement of Pluronic F127 within the gelatin scaffolding.

This effect can be seen for gels 9, 10, 11, and 12 in Figure 4. Gel 9, which had 9 %w/v gelatin crosslinked with 0.67 %w/v mTG, had a significantly lower elastic modulus than the comparable gel 10, 11, and 12 (p-value = 1.34 x 10^{-9}, 1.20 x 10^{-8}, 1.88 x 10^{-4}), which had 3.33, 5, and 6.67 %w/v Pluronic F127, respectively. Gel 12 contained more Pluronic F127 than gel 10, but the difference in the elastic modulus was not significant (p-value = 0.177). In these gels, the presence of Pluronic F127 adds stability by means of interaction between the hydrophilic polyethylene oxide chains and the network of crosslinked gelatin [10]. The insignificant increase in elastic modulus from 3.33 %w/v to 5 %w/v and 6.67 %w/v (p-value = 0.177, 0.270) may be because we have reached a threshold in the amount of physical crosslinking that can occur with Pluronic F127. The Pluronic F127's polyethylene oxide chains have made a sufficient amount of physical interactions with the gelatin network such that addition of more Pluronic F127 does not have a significant impact.

Using gels 1, 3, and 4, the effects of the addition of

Pluronic F127 in gels containing 13.5 %w/v gelatin and not crosslinked with mTG was determined. As it can be seen in Figure 4, increasing Pluronic F127 did have a mild increase in the elastic modulus of the gels. This is likely due to physical arrangements of the Pluronic F127 molecules in between the gelatin helices. It should be noted that dilute Pluronic F127 solutions (those with concentrations less than 15%) gel at temperatures above 30 °C, and these gels were analyzed at a temperature of 23 °C [5]. It is unlikely that the gelation of Pluronic F127 contributed to increased stability at this temperature.

For gels at the higher concentration of 13.5 %w/v gelatin and crosslinked with mTG, the addition of Pluronic F127 has a negative impact on the elastic modulus. This can be seen when comparing gels 5 and 6. Both gels 5 and 6 have 13.5 %w/v gelatin and were crosslinked with 0.1 %w/v mTG, but gel 5 with 5 %w/v Pluronic F127 had a higher elastic modulus than gel 6 with 7 %w/v Pluronic F127 (p-value = 0.00522).

The same behavior was observed in gels 2, 7 and 8, which all have high concentration of 13.5 %w/v gelatin and 1 %w/v mTG. Gel 2, which does not contain Pluronic F127, has a significantly higher elastic modulus than gels 7 and 8 which have 5 and 7 %w/v Pluronic F127, respectively (p-value = 6.93 x 10^{-6}, 3.35 x 10^{-6}).
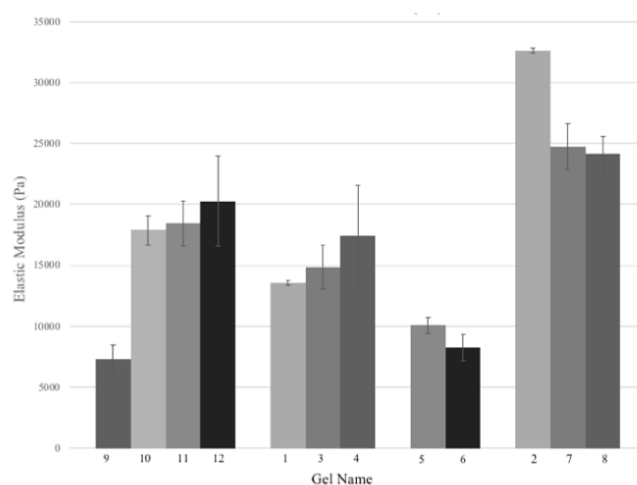

Figure 4: The above graph shows the elastic modulus for each gel sample. As can be seen by the trends between samples 9, 10, 11, and 12, which were formulated at a smaller concentration of gelatin, the addition of Pluronic F127 increased the elastic modulus. However, in samples where the gelatin concentration was increased to 13.5% wt/v, addition of Pluronic F127 decreased the elastic modulus or had no significant effect.

It is proposed that at concentrations of 13.5 %w/v gelatin, such a high amount of chemical crosslinking with mTG has occurred that the physical presence of Pluronic F127 no longer adds stability by filling in the gaps of the network. In fact, the presence of Pluronic F127 may obstruct the action of the mTG enzyme such that it is not

possible to form as many covalent bonds within the hydrogel.

A linear regression model was developed that relates the concentrations of gelatin, Pluronic F127, and mTG to the value of the elastic modulus. This model accounts for varying concentrations of gelatin, Pluronic F127, and mTG at a temperature of 37 °C. For means of determining this regression, data for the elastic moduli of gels 1, 3, and 4 were not included in the data set. These gels were analyzed at a temperature of 23 °C, and the effect of temperature on the moduli of the gel compositions was not investigated in this study. The model yields:

$$E_{Mod} = -8658 + 974x + 423y + 21306z \qquad (1)$$

where E_{Mod} is the elastic modulus of the gel in units of Pa, x is the concentration of gelatin in %w/v, y is the concentration of Pluronic F127 in %w/v, and z is the concentration of mTG in %w/v. The error in each of the coefficients is ±10796, ±803, ±814, and ±5925 respectively. The model shows that the coefficient of z is an order of magnitude larger than the coefficients of x and y. This suggests that changing the concentration of mTG has the greatest effect on the elastic modulus of a gel, while the addition of Pluronic F127 and gelatin have a smaller effect.

The ultimate failure stresses displayed in Figure 5 show similar trends to the elastic modulus values but have some notable differences. Gel 2 achieved the highest failure stress of 2482.29 $\pm$ 387.04 Pa, with the next best gel, gel 7, obtaining 1756.71 $\pm$ 435.05 Pa (p-value = 0.0630). An average 340% increase in failure stress was found when increasing the mTG concentration from 0.1 to 1 %w/v, as shown in the differences between gel 5 and 7 (p-value = 3.52 x 10^{-5}), and between gel 6 and 8 (p-value = 6.25 x 10^{-5}). The higher mTG concentration provided a greater amount of chemical crosslinking which lead to a higher failure stress. Overall, additional Pluronic F127 decreases failure stress as shown in gel groups 2, 7, 8; 1, 3, 4; and 10, 11, 12. This may be due to the incorporation of Pluronic F127 into the matrix which inhibits the rearrangement of the crosslinked gelatin in the direction of applied stress. This may increase rigidity and decrease the amount of stress required to cause breakage.

A linear regression model is also developed to relate the concentration of gelatin, Pluronic F127, and mTG to the failure stress. Data for gels 1, 3, and 4 were not considered in the model as these gels transitioned back to a liquid state at 37 °C. The model yields:

$$S_{Failure} = -2814 + 255x - 67y + 1583z \qquad (2)$$

where $S_{failure}$ is the failure stress of the gel in units of Pa, x is the concentration of gelatin in %w/v, y is the concentration of Pluronic F127 in %w/v, and z is the concentration of mTG in %w/v. The error in each of the coefficients is ±447, ±35, ±32, and ±243 respectively. The model shows the most dominating factor in determining
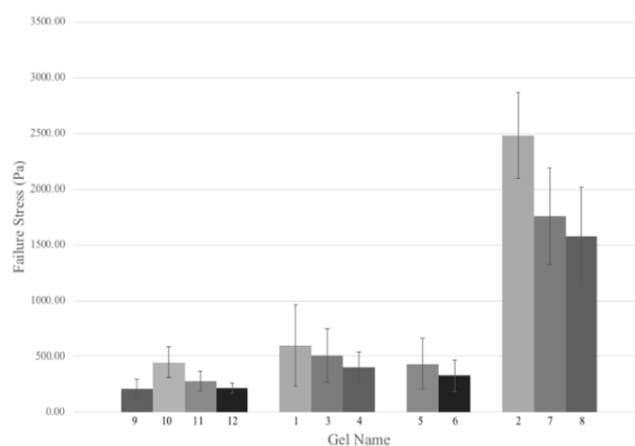

Figure 5: The above graph shows the failure stress for each gel. There is a general trend that as the concentration of Pluronic F127 increases, the failure stress of the gels decrease.

failure stress is the concentration of mTG as the coefficient of z is larger than the coefficient of x and y. This is consistent with the fact that a greater concentration of mTG results in more crosslinking which would strengthen the gel. The coefficient of y is negative which also suggest the addition of Pluronic F127 decreases the failure stress.
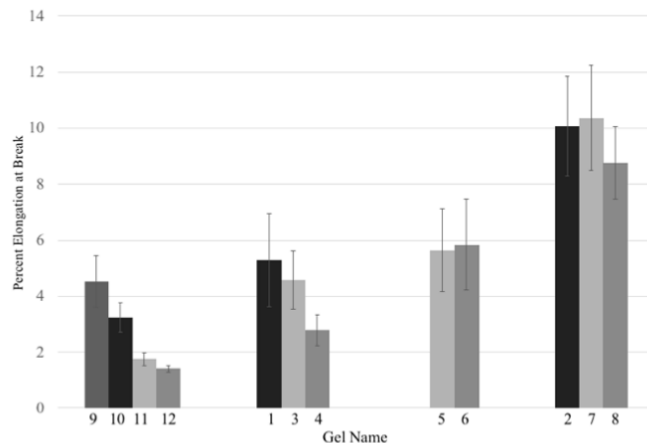

Figure 6: The above graph shows the percent elongation at break for each gel. It was observed for all varied gel compositions that as the concentration of Pluronic F127 increases, there is less percent elongation of the gels before breakage.

Percent elongation at break is a quantitative way to examine and compare the ductility of different materials, with more ductile materials having a higher elongation at break. As shown in Figure 6 the gels with the largest elongation at break were the 13.5% gelatin and 1% mTG group (gels 2, 7, 8) with gel 7 having the greatest elongation with 10.4 $\pm$ 3.8%. Gels 11 and 12 had the lowest elongation with gel 12 only achieving 1.4 $\pm$ 0.3%. The general trend

of increasing Pluronic F127 concentration leading to lower elongation at break can be seen from Figure 6 as well.

3.2. Suture Retention Testing Results

Gels 10, 11, and 12 are composed of 9 %w/v gelatin, 3.33, 5, and 6.67 %w/v Pluronic F127, and crosslinked with 0.67 %w/v mTG. The suture retention strength tests using the Instron 5542 showed that increasing Pluronic F127 concentration caused no significant difference between the max stress of gels 10 and 11 (p-value = 0.217) and between gels 10 and 12 (p-value = 0.676).

Table 2: Max stress reached on suture retention test.

Gel Name	Number of Samples	Max Stress (MPa)
2	5	0.040 ± 0.013
10	4	0.021 ± 0.006
11	5	0.016 ± 0.005
12	6	0.022 ± 0.005

The max stress experienced by gel 2 with 13.5 %w/v gelatin crosslinked with 1 %w/v mTG was significantly higher when compared to gels 10, 11 and 12 (p-value = 0.0292, 0.00401, 0.0324) as shown in Table 2.

The data suggest that the reason gel 2 had a higher max stress is either the removal of Pluronic F127 or the increased concentration of mTG. This conclusion follows the relationship described in Equation (2), derived from the rheology results, which states both factors have an effect on the max stress, but it is the higher concentrations of mTG that has the dominating effect. Further investigation into the suture retention strength of a wider variety of gel samples will hopefully confirm this and allow us to expand our conclusions.

3.3. Surface Roughness Analysis

From the laser scanning confocal microscope, parameters relating to the surface roughness, as well as topographical maps of the surfaces of the gels were obtained. Studies have found that surface roughness directly impacts the ability of cells to adhere to and proliferate on a surface and that surfaces exhibiting microroughness showed increased cell proliferation. Surface roughness can be broken down into three categories: macrorough (100 μm - millimeters), microrough (100 nm - 100 μm), and nanorough (less than 100 nm). Different cell types adhere and proliferate better on surfaces of different levels of surface roughness [11].

Table 3: Sa values for various hydrogels.

Gel Name	Sa (μm)
2	3.606
10	4.529
11	5.690
12	14.024

Table 3 shows the values of the arithmetic mean height (Sa), which is generally a good gauge of surface roughness, of the gels. Sa is calculated by the microscope by taking the absolute value of the difference between each point on the surface and the arithmetic mean of the surface. All data were taken at a magnification of 200x. As shown in Table 3, the surface roughness of the gels increased with increasing concentration of Pluronic F127. All surface roughness was in the microscale range. The topographical images found in Figure 7 display a visual representation of the gels' surface roughness.
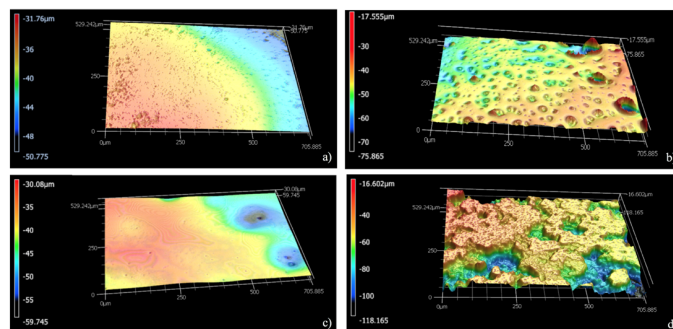

Figure 7: Topographical images of the surfaces of the gels with a) representing gel 2, b) representing gel 10, c) representing gel 11, and d) representing gel 12. Areas of lower elevation are represented by blues and greens, while areas of higher elevation are represented by reds, yellows, and oranges.

According to a study done by Chung et al., human vein endothelial cells demonstrated increased adhesion and growth on nanorough materials. Other studies have suggested that microrough materials provide an ideal surface for cell growth and proliferation [12]. These results are dependent on numerous factors include the material makeup and the type of cells tested. While our gels did not demonstrate nanoroughness, we still believe that their surfaces will allow for cell growth and proliferation due to the fact that microroughness has shown positive results during the testing of other materials. Images and surface data were only obtained for gels 2, 10, 11, and 12 but they provide a good baseline for further research into the other gel compositions that will hopefully confirm these conclusions.

3.4. Preliminary Cell Testing

Although in-depth cell adhesion and growth testing was not able to be performed due to time constraints, preliminary testing shows encouraging results. Cell plating attempts on samples 2, 10, and 12 showed positive results that can be seen in Figure 8. The observation of cell growth and proliferation on these samples further supports the claim that the microroughness of the gel surfaces will have a positive effect on the ability of cells to adhere to and proliferate on our gels. Further testing will need to be done to confirm these results, but endothelial cells appear to be able to adhere and proliferate on the hybrid gels.
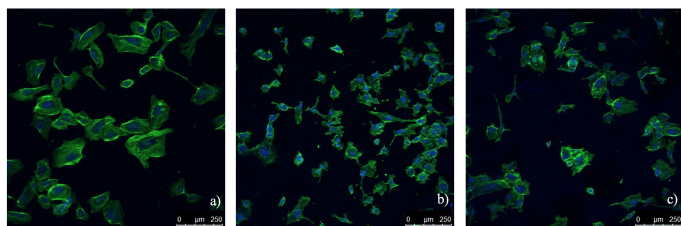
54

Figure 8: Images showing cell proliferation on gel 2 (a), gel 10 (b), and gel 12 (c). F-actin is visualized in the green channel, and cell nuclei are visualized in the blue channel.

4. Conclusion

The addition of Pluronic F127 has a mixed effect on the properties of gelatin mTG crosslinked hydrogels. At the lower concentrations of 9 %w/v gelatin or if the gel has no mTG crosslinking, adding Pluronic F127 improved the elastic modulus. At the higher concentration of 13.5 %w/v gelatin, adding Pluronic F127 either had no effect or decreased the elastic modulus. It is believed that the decreased elastic modulus at these higher concentrations of gelatin and mTG is caused by limited covalent crosslinking within the gelatin matrix itself such that the presence of Pluronic F127 obstructs the action of the mTG enzyme. In such a case, the physical crosslinking between gelatin and Pluronic F127 would be weaker than if covalent crosslinking was allowed to occur.

The failure stress for all compositions of gels tested either remains unchanged or decreases with the addition of Pluronic F127. We propose that Pluronic F127 interferes with mTG crosslinking at high concentrations of gelatin, thereby decreasing the overall strength of the gel. This behavior is shown in the rheology test and the suture retention test.

Although the hydrogels had promising results with respect to cell growth and proliferation, we believe that the addition of Pluronic F127 to gelatin hydrogels may not be an optimal choice for vascular grafts. At physiological temperatures of 37 °C the addition of Pluronic F127 to gelatin hydrogels crosslinked with mTG did not improve the mechanical properties, and in some cases it even decreased them.

5. Acknowledgments

6. References

[1] Allen S. Hoffman. Hydrogels for biomedical applications. *Advanced Drug Delivery Reviews*, 64(Supplement):18–23, 2012.

[2] Qi Xing, Keegan Yates, Caleb Vogt, Zichen Qian, Megan C. Frost, and Feng Zhao. Increasing mechanical strength of gelatin hydrogels by divalent metal ion removal. *Scientific Reports*, 4(1), 2014.

[3] CW Yung, L Wu, JA Tullman, GF Payne, WE Bently, and TA Barbari. Transglutaminase crosslinked gelatin as a tissue engineering scaffold. *Journal of Biomedical Materials Research*, 83A(4):1039–1046, 2007.

[4] Grad S Stoddart M Dockery P Alini M Pandit AS Halloran, DO. An injectable cross-linked scaffold for nucleus pulposus regeneration. *Biomaterials*, 29(4):438–447, 2008.

[5] Emilia Gioffredi, Monica Boffito, Stefano Calzone, Sara MAria Giannitelli, Alberto Rainer, Marcella Trombett, Pamela Mozetic, and Valera Chiono. Pluronic f127 hydrogel characterization and biofabrication in cellularized constructs for tissue engineering applications. *Procedia CIRP*, 49:125–132, 2016.

[6] AH El-Kamel. In vitro and in vivo evaluation of pluronic f127-based ocular delivery system for timolol maleate. *International Journal of Pharmaceuticals*, 241(1), 2002.

[7] Mei-Yu Yeh, Jiong-Yao Zhao, Yi-Ru Hsieh, Jhong-Hua Lin, Fang-Yi Chen, Rajan Deepan Chakravarthy, Pei-Chun Chung, Hsin-Chieh Lin, and Shih-Chieh Hung. Reverse thermo-responsive hydrogels prepared from pluronic f127 and gelatin composite materials. *RSC Advances*, 7(34):21252–21257, 2017.

[8] S. Pashneh-Tala, S. MacNeil, and F. Claeyssens. The tissue-engineered vascular graftpast, present, and future. *Tissue Engineering*, 22(1):68–100, 2016.

[9] CR Clayton. Materials science and engineering: An introduction: by wd callister jr. *Wiley*, 1987.

[10] R. Li, J. Sutaria, and C. Wang. Synthesizing and characterizing novel gelatin and pluronic f127 hybrid hydrogels as a barrier membrane for guided bone regeneration following periodontitis. *Private Communications*.

[11] H. Chang and Y. Wang. Cell responses to surface and architecture of tissue engineering scaffolds. *Regenerative Medicine and Tissue Engineering - Cells and Biomaterials*, pages 569–588, 2011.

[12] T. Chung, D. Liu, S. Wang, and S. Wang. Enhancement of the growth of human endothelial cells by surface roughness at nanometer scale. *Biomaterials*, 24(25):4655–4661, 2003.

JUCER

Atomic Layer Deposition of TiO$_2$ support on PEM to Increase Fuel Cell Electrode Durability by CO Oxidation Enhancement

Simon Lin[a], Ryan Kerr[a], Landen Kwan[a], Chengchao Xu[a], Tak Kit Yeung[a], Christopher Zambito[a], Likun Wang[a], Miriam Rafailovich[a]

[a]*Department of Materials Science and Chemical Engineering , Stony Brook, NY 11794, USA*

Abstract

The demand for clean alternative energy sources are becoming increasingly relevant as greenhouse gas emissions steadily increase. A potential clean energy source to meet this demand is the proton exchange membrane fuel cell (PEMFC) which produces water as its major by product. The issues preventing these PEMFC systems from succeeding are the high costs associated with using precious platinum (Pt) metals to catalyze hydrogen ions, integrating an efficient yet cost effective performance system, and increasing the overall life expectancy of the fuel cell for prolonged usage. Our study focuses particularly on increasing the durability of the fuel cell by protecting the Pt catalysts from carbon monoxide (CO) poisoning with enhanced CO oxidation to carbon dioxide (CO$_2$). We found the support modification of the PEMFC system to be significant for preventing the carbon monoxide poisoning of the precious Pt metal electrodes thus increasing the durability of the fuel cell. The support used is titanium dioxide (TiO$_2$) coated by atomic layer deposition (ALD). Since gold (Au) to TiO$_2$ interfaces are also known to enhance CO oxidation, we used a Langmuir-Blodgett (LB) trough to coat Au on various thicknesses of TiO$_2$ to examine the performance trend in correlation to only TiO$_2$ coatings. The membranes were characterized using Energy Dispersive X-Ray (EDX) and Ellipsometry to confirm the successful ALD coatings of TiO$_2$ and to measure the specific thickness for each coated sample. The performance data trend of TiO$_2$ and Au-TiO$_2$ was obtained by averaging 5 data sets of the power density using a fuel cell testing station. The performance data trend showed an increase in power density from thickening the TiO$_2$film until a drop off point, from which an increase of thickness would be detrimental towards the PEMFC performance. Using the best performing sample, we analyzed the durability enhancement in comparison to a standard control 117 Nafion membrane.
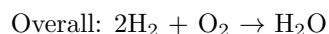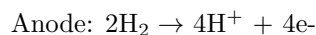
Keywords: PEM fuel cell, Atomic layer deposition, Langmuir-Blodgett method

1. Introduction

Currently, the most common source of energy used around the world is fossil fuel. The use of fossil fuels causes multiple issues such as the limited supply of fuel and the amount of greenhouse gases emissions. There is interest to find a renewable energy source that can supplement and possibly replace fossil fuel technology in the future. One of these renewable energy technologies being researched is the fuel cell. Fuel cells are devices that can convert chemical energy into electricity. Fuel cells are an attractive energy technology as they have a high energy density, a low operating temperature and does not emit greenhouse gases [1].

One of the most common types of fuel cells is a proton exchange membrane (PEM) fuel cell. In PEM fuel cells, a membrane is placed between the anode and cathode. This membrane allows protons to flow through while not allowing electrons. The best membranes are those that have good proton conductivity, poor electron conductivity and low reactant permeability. The membrane most commonly used that meets these characteristics is known as Nafion [2].

In PEM fuel cells, hydrogen is fed to the anode and oxygen is fed to the cathode. A catalyst is placed on the electrode to facilitate the reactions. On the anode side, hydrogen dissociates into protons and electrons. The protons flow through the membrane while the electrons are moved through an external circuit to the cathode. At the cathode, the protons and electrons combine with oxygen to create water and heat [2].

Anode: $2H_2 \rightarrow 4H^+ + 4e\text{-}$

Cathode: $O_2 + 4H^+ + 4e\text{-} \rightarrow 2H_2O$

Overall: $2H_2 + O_2 \rightarrow H_2O$

The catalyst is a very important factor in the performance and the durability of a fuel cell. There are many factors that must be considered when selecting a catalyst, including activity, selectivity, and poisoning resistance. Platinum (Pt) is currently the most widely used catalyst for PEM fuel cells [3]. However, there are issues involving Pt catalysts, the main issue being carbon monoxide (CO)

accumulation. One of the byproducts of any carbon dioxide present in a fuel cell is CO. This CO accumulates on the electrodes, which poisons the Pt catalysts and reduces the power output by about 50% [1].

Many different types of catalysts have been researched to supplement Pt and deal with the issue of CO poisoning. One promising catalyst is gold (Au) nanoparticles. Au nanoparticles with diameters of 25 nm have been shown to have high CO oxidation at low temperatures, which helps to overcome the main hurdle with using Pt. Furthermore, it is known that Au nanoparticles deposited on metal oxide supports have an enhanced CO oxidation effect. Many supports have been researched, including titanium dioxide (TiO_2), iron oxide (Fe_2O_3), and cobalt oxide (Co_3O_4) [4]. For fuel cell purposes, a good support should have good proton conductivity, ability to stabilize nanoparticle dispersion, poor electron conduction, and no conduction of H2 [5].

An important factor affecting the metal oxide support is the method that is used to layer it on the membrane. There are many different methods used to layer the metal oxide support, one of the most prominent being chemical vapor deposition (CVD). The main drawback of CVD is that it is a non-self-limiting reaction. This means that the method those not give adequate control over the thickness or uniformity of the metal oxide support. An alternative method to CVD that is gaining prominence is atomic layer deposition (ALD). The ALD method is a multi-step gas phase chemical process that allows for layer-by-layer deposition of the metal oxide. ALD is the only method that allow for greater control over the thickness of the metal oxide layer at a low temperature [6].

In our research, we used ALD to layer TiO_2 onto Nafion to create membranes with different thicknesses of TiO_2. We then used a Langmuir Blodgett (LB) trough to disperse our Au nanoparticles onto the membranes. The completed membranes were then tested on the hydrogen fuel cell test station at Stony Brook University to determine the power output of the fuel cell with the varied TiO_2 thicknesses compared to a control. We hypothesize the catalysts with thicker layers of TiO_2 will have a better performance. If successful, this research could be used to increase the performance and durability of fuel cell catalysts.

2. Methodologies

2.1. Materials

Both Nafion 117 membrane and 0.1 mg/cm^2 Pt loading electrode catalyst paper were purchased from The Fuel Cell Store. Au nanoparticles were synthesized at Stony Brook University. TiO_2 was acquired from Brookhaven National Laboratorys Center for Functional Nanomaterials and deposited using ALD with titanium isopropoxide (TTiP) and H2O as precursors. The fuel cell demonstration kit uses 99.99% pure hydrogen as reactant.

2.2. Experimental Methods
2.2.1. ALD Coating

Our group used ALD because the temperature of operation is ideal in preserving the structure of Nafion membrane. The Cambridge NanoTech, Model Savannah 100 was the deposition medium. Titanium isopropoxide (TTiP) and H_2O were the precursors for TiO_2. The chamber temperature was set as 85 °C, which is a relatively low temperature. Every cycle includes following steps: (1) Pulsing TTiP for 0.5s, resting for 6s, then purged with nitrogen flow for 12s; (2) Pulsing H_2O for 0.4s, resting for 6s, then purged with nitrogen flow for 12s. We placed a Nafion 117 membrane and a silicon wafer as the substrates for TiO_2 coating each time. Glass strips were used to fix the position of membranes to avoid uneven coating of the membrane due to curving. The silicon wafer was used to gather the same deposit sample to measure the characteristics of that specific deposition run. We repeated the coating for 10, 20, and 30 cycles.

2.2.2. LB Trough Coating

A Langmuir-Blodgett trough was used to coat gold nanoparticles onto the TiO_2 coating on the membrane. The trough was controlled by using KSV Instruments Ltd software. After the membranes were clamped to the dipper, they were lowered into the water until the dipper rested just above the water surface. A 250 μL syringe was used to spread 150 μL of Au nanoparticle solution to the water surface of both sides of the trough. The target pressure was set to 3.0 mN/m with pushing rate of 10 mm/min. Once the surface pressure reached 3.0 mN/m, the membranes were lifted from the water while maintaining the target pressure.

2.2.3. Fuel Cell Demonstration Kit

The Fuel Cell Demonstration Kit was operated at room temperature (25 °C) to test the performances of different samples (membranes coated with 10, 20, or 30 cycles of TiO_2 and with or without Au coating). To carry out a performance test, we hydrated the Nafion 117 membrane with deionized water and placed it in a prefabricated membrane electrode assembly (MEA). A constant flow of 78 ccm 99.99% pure hydrogen gas and the air were the reactants of the anode and cathode, respectively. The Demonstration Kit was connected to a BK PRECISION 8601 direct current electronic load. We have pre-programmed it to constant currents with the increment of 0.5A every 30 seconds for each sample. At least five tests were performed for each sample. The maximum power output of the samples was used to analyze each MEA performance.

2.3. Analytical Methods
2.3.1. Scanning Electron Microscope (SEM) and Energy-Dispersive X-ray Spectroscopy (EDX) Spectroscopy Imaging

TiO_2 mapping was subjected to SEM observations using the ZEISS Crossbeam 340. The TiO_2 deposited silicon

wafer sample obtained from ALD, was fixed in place in the sample holder of the SEM for analysis. EDX results and elemental mapping were also generated for further analysis.

2.3.2. Transmission Electron Microscope

To analyze the Au nanoparticle samples, we dipped the TEM grid in the compressed LB trough. Using JEOL JEM 1400 we observed the sample.

3. Results and Discussion

3.1. Characterization

The TEM image of LB trough Au particle monolayer is shown in Figure 1. The Au nanoparticles diameter average at 1.64 nm, with the particle size distribution showing relatively concentrated distribution around 1.5 and 2.0 nm in Figure 2. Figure 3 shows that the ALD film thickness and number of cycles fit well into the linear relationship, exhibiting the overall growth rate of 0.069 nm per cycle.
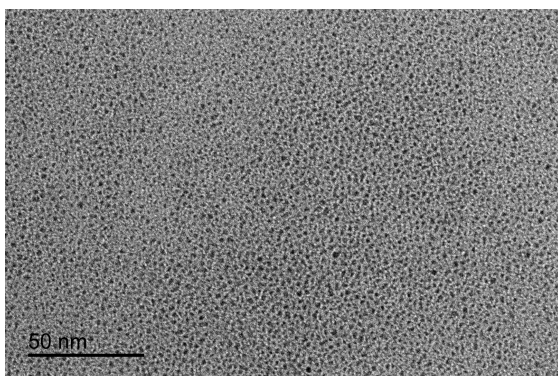
Figure 1: TEM images of Au nanoparticles

The SEM images of ALD deposited TiO_2 film on Si wafer are shown in Figure 4. The surface image (Figure. 4(a)) shows that the deposited film has a mirror-like, flat surface, indicating the uniformity of the film. EDX measurements were carried out to evaluate the chemical composition of ALD films and the distribution of TiO_2. The EDX elemental spectrum (Figure. 4(c)) confirms the existence of Ti and shows the relative concentration of Ti atoms. The elemental mapping image of Ti showing the even distribution of Ti atoms is presented in Figure 4(d), indicating a successful deposition of uniform TiO_2 film on the substrates.

3.2. Performance Test

Figure 5 shows the decrease of fuel cell performance with the layering of a uniform TiO_2 film on Nafion membrane. The performance drop suggests an inhibition of proton transfer at the TiO_2 layer. The slight performance increase between 10 and 20 cycles could be due to an increase of proton conductivity at higher TiO_2 thicknesses
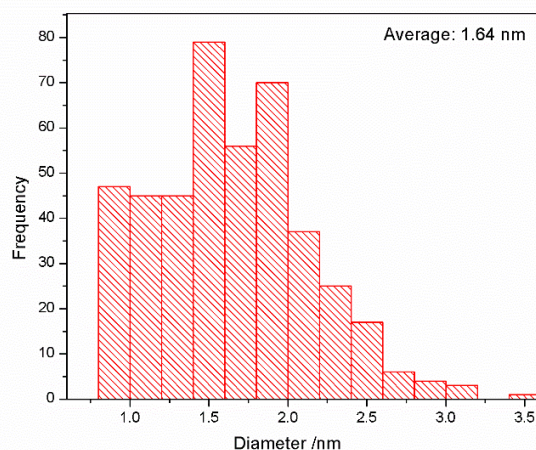

Figure 2: AuNPs size distribution

[5]. The optimal fuel cell performance from varying TiO_2 thicknesses was not determined since our focus is to use TiO_2 as a CO oxidizing support for protecting the Pt electrode.
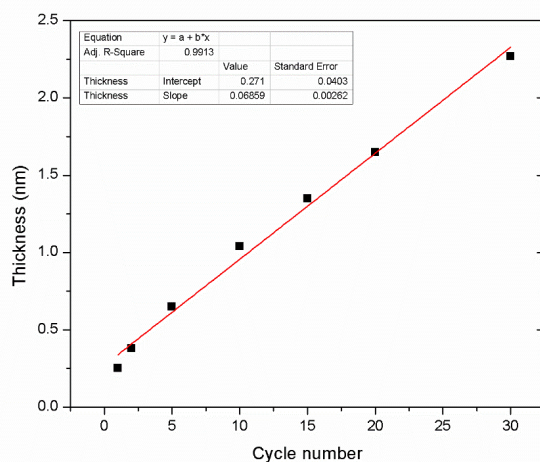

Figure 3: The linear relationship between TiO2 thickness on Si and the number of deposition cycles.

The performance of gold coated on the TiO_2 support is shown in Figure 6. All samples were tested using a new set of electrodes due to the performance test contamination of the previous electrodes. The graph shows a 22% performance increase from coating Au on 20 cycles TiO_2. This suggests that Au/TiO_2 can be a cost effective coating for enhancing PEMFC performance. Assuming the enhanced CO oxidation effects as depicted in Harutas work [4], the coating of Au/TiO_2 on PEMFC is shown to be an effective performance enhancer while
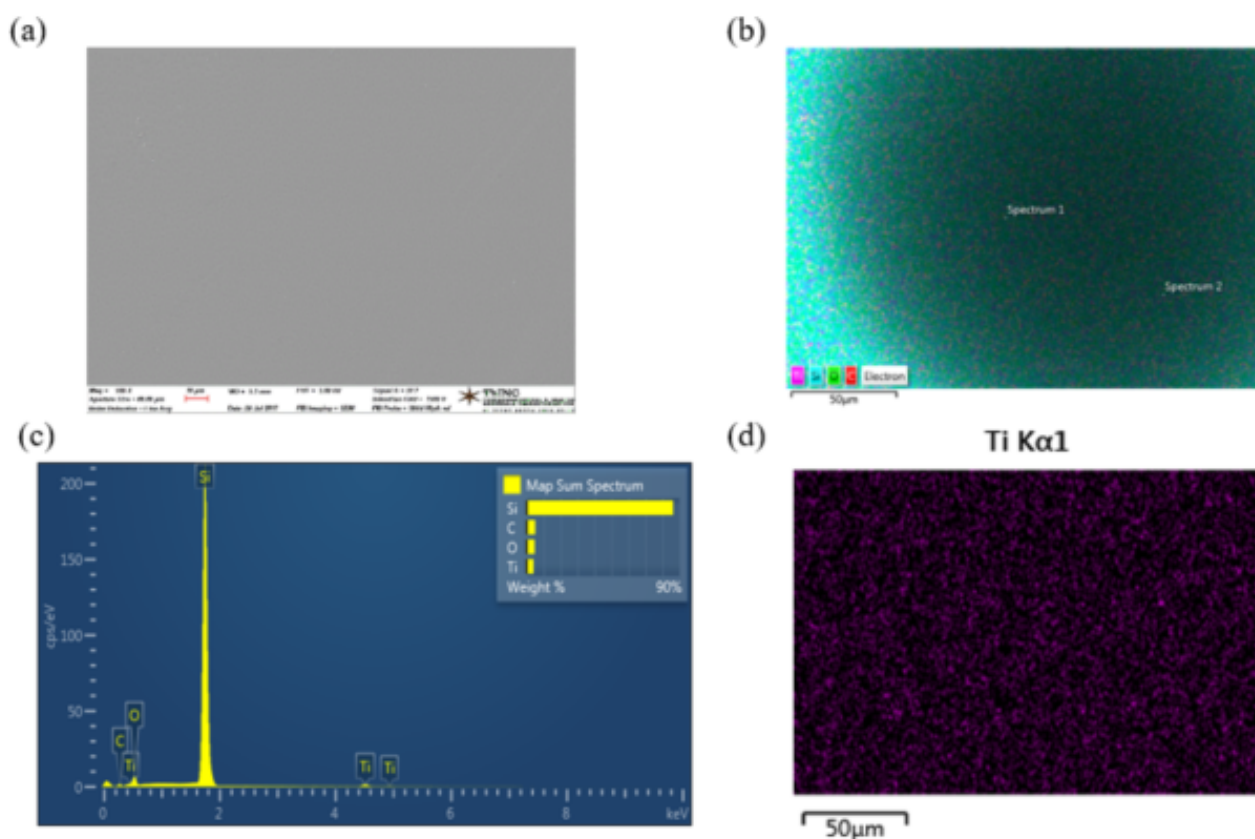
Figure 4: (a) SEM image of ALD TiO2 film on Si wafer (b) Elemental mapping of Si wafer surface after 50 ALD cycles (c) EDX Spectrum of ALD film surface (d) Elemental mapping of Ti on ALD film surface.
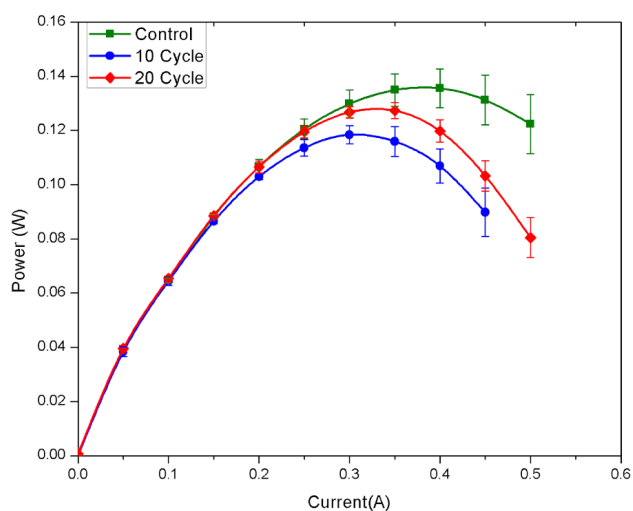

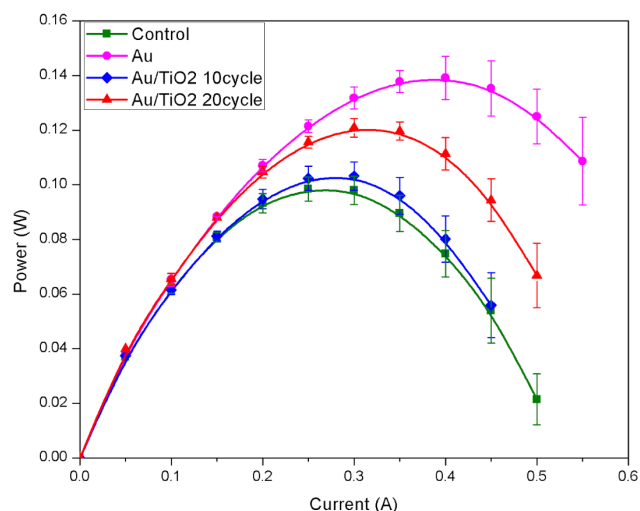Figure 5: Performance Effect of 10, 20 cycle TiO_2 on Nafion 117 membrane

Figure 6: Performance of Au on TiO2 support versus control using new electrodes for all samples

providing significant protection of the Pt electrodes. More research is needed to find the optimal TiO_2 thickness and its relative performance, but we have shown that Au/TiO_2 can provide a good performance enhancement while protecting the Pt electrodes by enhancing CO oxidation.

4. Conclusion

Long term durability is a significant concern when considering a PEM fuel cell for real-world applications. Existing research demonstrates that Au nanoparticles supported by TiO_2 provides significant resistance against CO poisoning by providing enhanced CO oxidation to CO_2 [4][7].

Using ALD, we applied TiO_2 coatings to Nafion 117 membranes. These membranes underwent PEM fuel cell performance tests which showed decreased power output when compared to an uncoated control membrane. The membranes were then coated with Au nanoparticles using the LangmuirBlodgett method. These Au/TiO_2 membranes underwent performance tests and exhibited significantly greater performance, up to a 22% greater power output, when compared to an uncoated control. We hypothesize that Au/TiO_2 coatings on a Nafion membrane can provide viable long term protection against CO poisoning, thus enhancing the durability of the Pt electrodes while improving performance capabilities throughout the lifecycle of the fuel cell.

5. Acknowledgments

6. References

[1] Hongfei Li, Cheng Pan, Sijia Zhao, Ping Liu, Yimei Zhu, and Miriam H Rafailovich. Enhancing performance of pem fuel cells: Using the au nanoplatelet/nafion interface to enable co oxidation under ambient conditions. *Journal of Catalysis*, 339:31–37, 2016.

[2] Ram Devanathan. Recent developments in proton exchange membranes for fuel cells. *Energy & Environmental Science*, 1(1):101–119, 2008.

[3] Oliver T Holton and Joseph W Stevenson. The role of platinum in proton exchange membrane fuel cells. *Platinum Metals Review*, 57(4):259–271, 2013.

[4] Tamao Ishida, Hiroaki Koga, Mitsutaka Okumura, and Masatake Haruta. Advances in gold catalysis and understanding the catalytic mechanism. *The Chemical Record*, 16(5):2278–2293, 2016.

[5] Marie Gustavsson, Henrik Ekström, Per Hanarp, Lisa Eurenius, Göran Lindbergh, Eva Olsson, and Bengt Kasemo. Thin film pt/tio2 catalysts for the polymer electrolyte fuel cell. *Journal of Power Sources*, 163(2):671–678, 2007.

[6] Hao Feng, Junling Lu, Peter C Stair, and Jeffrey W Elam. Alumina over-coating on pd nanoparticle catalysts by atomic layer deposition: Enhanced stability and reactivity. *Catalysis Letters*, 141(4):512–517, 2011.

[7] Tadahiro Fujitani and Isao Nakamura. Mechanism and active sites of the oxidation of co over au/tio2. *Angewandte Chemie International Edition*, 50(43):10144–10147, 2011.

Micro-Cellulose Based Water Filtration System

Richard Antoine[a], Jayson Woodbine[a], Kevin Osadiaye[a], Nigel Stanford[a], Vincent Orcullo[a], Visal Thalawe Arachchilage[a], Benjamin Hsiao[b], Priyanka Sharma[b]

[a]*Department of Material Science and Chemical Engineering, Stony Brook, NY 11794, USA*
[b]*Department of Chemistry, Stony Brook, NY 11794, USA*

Abstract

Water contamination has always been an issue in many places around the world, causing harmful consequences in developing countries where modern water infrastructure is infeasible due to population growth, increasing urbanization, and climate change. This creates a need for a low cost and easily accessible water purification system capable of removing contaminants such as bacteria, viruses, and heavy metals. Cellulose is a cheap, abundant natural polymer that can be easily functionalized. Microcellulose fibers were synthesized performing nitro oxidation on agave and phosphoric acid treatment on jute and wood pulp. This study presents a two-phase water filtration system utilizing nanocellulose fibers. The microcellulose fibers are placed into lead concentrated water where it is hypothesized that the fibers will adsorb lead ions, removing metal ions from water. An interface between the water and the coagulated cellulose was created with the adsorbed lead (Pb) ions. A silica sand filter is then used for further purification of water in addition to retaining cellulose fibers and other solid contaminants, thus aiding in the production of clean drinking water. The cellulose fibers demonstrated an efficient adsorption capacity for lead ions. The research shows cellulose fiber coagulation and sand filtration are sustainable and efficient water treatment technologies for heavy metal remediation.

Keywords: Water Treatment, Microfibrillated Cellulose, Heavy Metal Ions, Lead

1. Introduction

Clean water is a basic necessity for life. Aside from being essential to healthy biological functioning, clean water is important for cooking, cleaning, and overall sanitation. Unfortunately, it is estimated that up to 780 million people lack access to this valuable resource and worldwide, nearly 2 billion people drink contaminated water that could be harmful to their health [1, 2].

For populations where access to water presents a daily toil to simply continue living, the solution is not always as simple as going to the well or stream if one even exists. This is because in many parts of the world even the local water sources have been contaminated by poisonous elements and chemicals from agricultural runoff, dumping by local industry, or local geology.

Water containing heavy metals, including lead, from any of these sources poses a major risk to anyone who drinks it. This is even more true for children who may be exposed to these elements.

We have developed a two-step cellulose water filtration system to combat water pollution. This water filtration system is an inexpensive alternative source for purifying contaminated water. A key component in this filtration system is silica sand. The presence of silica sand plays a role in water treatment processes. It stems from quartz, which is then broken down by water and wind into tiny granules. In this experiment, silica interactions will be examined by tracking the composition of lead in the prepared sample in the presence and absence of sand. The water filtration system consists of a filtration unit made up of silica sand and a coagulation adsorption process set to purify water containing lead ions as well as other water contaminants.

2. Materials and Methods

2.1. Materials

Sodium hydroxide pellets and sodium hypochlorite were obtained from Sigma Aldrich, Phosphoric Acid (≥ 85 wt %) ACS Reagent from Sigma-Aldrich, nitric acid and sodium nitrite from Fisher Scientific, and denatured alcohol from VWR Amresco Life Sciences. All materials were used without further purification unless otherwise noted.

2.1.1. Silica Sand

For the purpose of this study, silica sand was chosen for addition remediation and adsorption of lead ions. Silica sand is one of the worlds most common sands and holds many applications in water treatment and other industrial processes. Sand filtration is regarded as the oldest wastewater treatment technology known. With a proper design and construction, sand produces a very high quality of effluent [3]. The heavy metal-sand adsorption phenomena can be illustrated on the basis of the interaction between surface functional group of silicates (sand) and the metal

ions. Silica sand is used in filtration, chemical adsorption, and assimilation [3]. It is deduced that sand can be used as a low-cost adsorbent for the removal of heavy metal from wastewater, especially in developing countries [2].

2.2. Experimental Methods

2.2.1. Preliminary Tests

For preliminary tests the group chose to use a commercially based filter to measure the filtration systems efficiency for lead concentrated water. The filter used was a BRITA Stream Filter, which is composed of activated carbon in addition to other advanced technologies and parameters meant to remove up to 99% of lead and other contaminants in water.

XRF analysis was used to measure lead concentration before and after filtration. The analysis showed that the BRITA filter did in fact remove most, if not all of the lead in the water samples prepared. In this experiment we will try to imitate similar filtration efficiency. However, we realize the technologies used in our filtration system may not remove 99% of lead. Our goal is to remove enough lead to meet the standards for acceptable drinking water quality.

2.2.2. Water Sample Preparation

Water samples were made using lead (II) acetate as a source for lead (II) ions. Two sets of three samples were prepared with concentrations of 50, 250, and 500 ppm. Sample concentrations were confirmed using X-ray fluorescence (XRF) in addition to inductively coupled plasma mass spectrometry (ICP-MS), which allows for the detection of metals in solution. These spectroscopy techniques were also used post-filtration to test filtration efficiency in the remediation of lead ions in water.

2.2.3. Microfibrillated Cellulose Preparation

Microfibrillated cellulose (MFC) fibers were synthesized using two methods from two kinds of biomass: phosphoric acid treatment using jute and nitro oxidation using agave.

MFC from raw jute fibers were prepared using a pretreatment process of 2% sodium hydroxide solution at 80 °C for six hours. The fibers where then washed with distilled water and placed in the oven for drying. These fibers were subsequently soaked in 1% sodium chlorite solution adjusted to a pH of 4 with acetic acid and the entire mixture was heated to 70 °C for three hours. This step was repeated five times. The resulting fibers were soft with a slippery texture and had a bright white color.

The pretreated jute fibers were added to a round bottom flask which was preheated in an oil bath to 70 °C and covered with 15 mL of phosphoric acid per gram of fiber. The acid was allowed to penetrate the fibers under mild stirring. After thirty minutes the reaction was quenched using 100 mL of anhydrous denatured ethanol per gram of fiber. The entire contents of the flask were placed in

the freezer to cool and allow the fibers to settle. After one hour, the supernatant was decanted, and the fibers were solvent exchanged to water. This was then placed for dialysis with periodic replacement of the water bath until the bath possessed a low conductivity, leaving an aqueous suspension of fibers.

The process for nitro oxidizing the agave fibers required no pretreatment. Raw biomass was cut into small pieces and rinsed with deionized water several times to remove impurities. The biomass was then combined with 14 grams of nitric acid per gram of untreated biomass in a round bottom flask. The acid was allowed to completely soak the sample. After this soaking, 0.96 grams of sodium nitrite per gram of biomass were added to the reaction flask under continuous stirring (note: this creates red fumes which must be contained by using a stopper on the flask after the addition of sodium nitrite. This step must be performed in a fume hood while using personal protective equipment). The reaction was sustained at 50 °C in an oil bath for 12 hours. Afterwards the reaction was quenched by 250 mL of distilled water. The reaction was allowed to reach equilibrium and the supernatant liquid was removed. More distilled water was added, and this step was repeated until the cellulose fibers began to suspend in the water. The product was recovered then rinsed with water until the pH of the upper suspension was greater than or equal to 2.5. At this point the mixture was placed for dialysis and the water bath was changed regularly until the bath had a low conductivity.

2.2.4. Cellulose Coagulation Adsorption

All three forms of cellulose fibers were placed in the various lead concentrations prepared: 50, 250, and 500 ppm. The mixture was left to adsorb overnight. The next day we observed cellulose settled at the bottom, creating a clear separation between the cellulose and water. The water looked much clearer than the lead concentrated solutions before the cellulose was placed in solution. We hypothesized that this means most of the lead ions in the solution did in fact adsorb into the coagulated cellulose. We also observed a crystalline structure on the surface of the coagulated cellulose fibers, which led us to believe adsorption of lead ions did occur.

2.2.5. Water Filtration Unit

The water filtration unit was constructed using 50 ml centrifuge tubes. The end of each tube was cut and a VWR Grade 454 Quantitative Filter Paper was taped to one end as support for the sand. This end went into the tube (Fig. 1). Silica sand was washed with distilled water and placed into the filtration unit. The distilled water ran through the filter to compact and clean the sand. The pore size of the filter paper was 12 μm, allowing for the retention of both sand and cellulose fibers. However, the filter paper is permeable to water. The result is purified water.
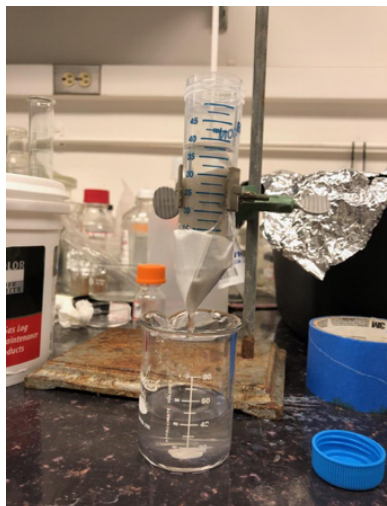
Figure 1: Filtration unit set up.

3. Results

Scanning Electron Microscopy (SEM) imaging was used to confirm the size of the Microcellulose fibers synthesized, in addition to any other surface properties that may be seen on the surface of the cellulose fibers such as structure and arrangement of fibers.
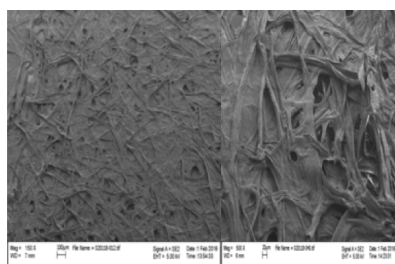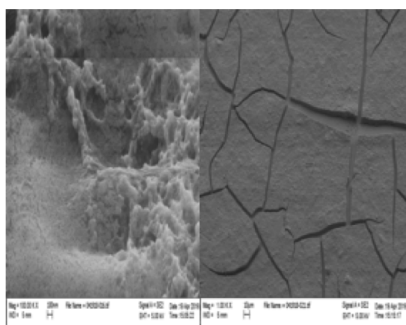

Figure 2: SEM images of nitro-oxidized agave fibers.

Figure 3: SEM images of phosphoric acid treated jute fibers.

The FTIR spectra of untreated jute fibers and agave fibers in Figures 5 and 6 show several distinctive peaks:
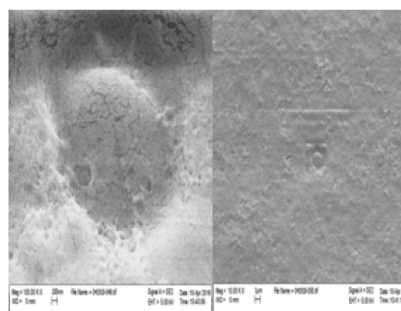
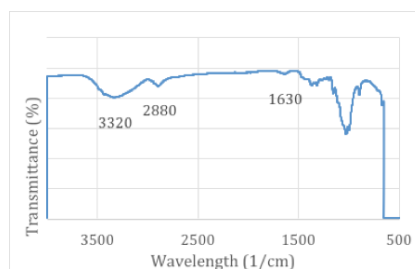Figure 4: SEM images of phosphoric acid treated wood pulp fibers.

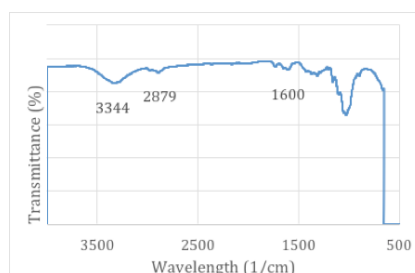Figure 5: FTIR spectra of treated jute fiber.

Figure 6: FTIR spectra of treated agave fiber.

3320 and 3344 cm^{-1} (OH stretching) and 2880 and 2879 cm^{-1} (CH symmetrical stretching), 1600 and 1630 cm^{-1} (C=C aromatic symmetrical stretching) in the lignin unit. The peaks around 1600 cm^{-1} confirm the presence of the carbonate bond and that the bicarbonate treatment was successful.
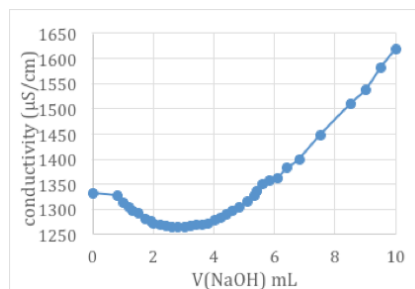

Figure 7: Conductometric titration curve of nitro oxidized agave cellulose sample.

The carboxyl content of oxidized cellulose samples was determined by conductometric titrations. The cellulose samples were suspended into 15 mL of 0.01 M hydrochloric acid solution. After 10 min of stirring, the suspensions were titrated with 0.01 M NaOH. The titration curves showed the presence of strong acid, corresponding with HCl excess and weak acid corresponding to the carboxyl content, as shown in Figure 7. The carboxyl groups content or degree of oxidation (DO) is given by the following equation below:

$$DO = 162(V_1 - V_2)c[w - 36(V_2 - V_1)c]^{-1} \qquad (1)$$

where V_1 and V_2 are the amount of NaOH (L) which are 2 mL and 4 mL respectively, c is the NaOH concentration (mol/L), and w is the weight of oven-dried sample (g) [4].

3.1. Adsorption

All samples prepared were mixed with different concentrations of Pb contaminated water. The samples were immersed for 24 hrs, with a 1:1 volume distribution of the water and the cellulose sample.
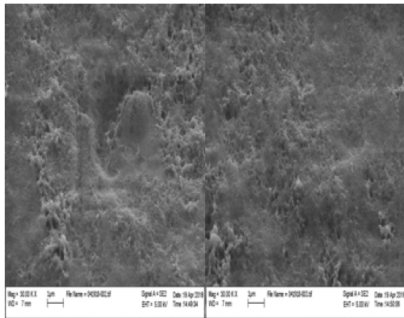

Figure 8: SEM image of phosphoric acid treated jute fibers suspended in 500 ppm of PB water.
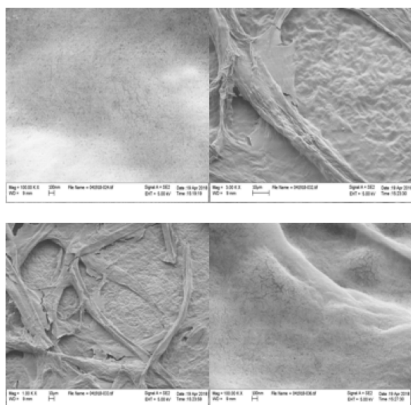

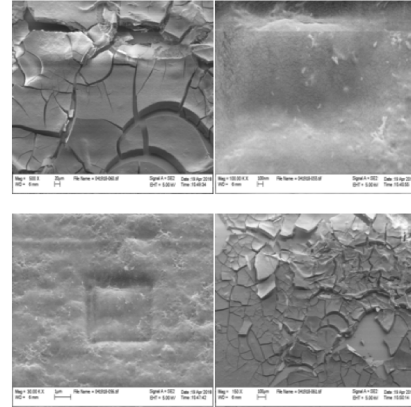Figure 9: SEM image of nitro-oxidized agave fibers suspended in 500 ppm of Pb water.

Figure 10: SEM image of phosphoric acid treated wood pulp fibers suspended in 500 ppm of Pb water.

Table 1: XRF analysis.

Materials	Concentration (parts per million)	
	Before Treatment	After Treatment
Jute	50	LOD
	250	13.722
	500	19.354
Nitro Oxidized Agave	50	LOD
	250	7.012
	500	18.905
Sand	50	LOD
	250	15.09
	500	12.474
Wood Pulp	50	LOD
	250	4.287
	500	7.462

3.2. XRF Analysis

XRF spectroscopy was performed on a Niton XL3t GOLDD+ hand held XRF (Thermo Scientific) using Niton data Transfer Software Version 8.4.1.1. All samples were testing in mining mode to get a wide spectrum of the chemical makeup of the materials including possible impurities. Spectra were analyzed using the Niton Software version DEV 8.4.1.1. Note: The 50 ppm sample was below the instrument's detectable limit

4. Conclusion

Conclusively, microcellulose is a great adsorbent of heavy metal ions. The ability to synthesize it cheaply using raw bio materials, make it more attractive and commercially viable. Using lead as the water contaminant and preparing different samples of different concentrations mixed with synthesized, functionalized micro-cellulose, X-ray fluorescence (XRF) and varian inductively coupled plasma mass spectrometry (ICP-MS) successfully tested the adsorbance, yielding significantly positive results. The addition of sand filtration showed promising results when

coupled with the cellulose adsorption. The water filtration system was assembled using VWR grade 454 quantitative filter paper as the support for the micro-cellulose, producing a flow rate of 27 mL/min.

For future work, focus should be placed on a better design for the water filtration system. Based on our results, it is evident that the design of the water filtration system affects the filtration time. In addition, further experimentation could be done on the biomass - in our case jute, agave, and wood pulp - to produce nanocellulose. This can then be used to combine both micro and nanocellulose, increasing the efficiency of adsorption of heavy metal ions. To completely ensure that the filtered water is free from protozoan cyst and bacteria, additional experimentation could be done in order to analyze and combine the bacteriostatic properties, dye adsorption properties, etc. along with heavy metal ion adsorption in creating a more efficient water filter.

5. Acknowledgments

6. References

[1] A. Pruss-Ustun, R Bos, F Gore, and J Bartram. Safer water, better health: cost, benefits and sustainability of interventions to protect and promote health. *World Health Organization, Geneva*, pages 170–176, 2008.

[2] NIH. Water pollution. 2018.

[3] MA Awan, IA Qazi, and I Khalid. Removal of heavy metals through adsorption using sand. *Journal of Environmental Science*, 15(3):413–416, 2003.

[4] Denilson da Silva Perez, Suzelei Montanari, and Michel R. Vignon. Tempo-mediated oxidation of cellulose iii. *Biomacromolecules*, 4(5):1417–1425, 2003.

JUCER

Application of ASTM Test Methods to Analyze the Oxidation Properties of Automotive Gasoline in Various Test Conditions

Tahseen Tabassum[a], Hyun Tak Tyler Cho[a]

[a]Department of Materials Science and Chemical Engineering, Stony Brook, NY 11794, USA

Abstract

Determination of oxidation properties of petroleum products is important to determine their reactivity in the presence of air, moisture, and organic compounds. Petroleum products are unstable as they form gum upon aging in the presence of air which is directly related to oxidation of gasoline. As the oxidation occurs in the system, the molecules of oxygen decrease resulting in the pressure drop in the system. Additionally, the presence of sulfur and other organic molecules can accelerate the oxidation in gasoline. The current method ASTM D525 Standard test method for oxidation stability of gasoline (Induction Period Method) covers the determination of the stability of gasoline under accelerated oxidation conditions and ASTM D130 Standard Test Method for Corrosiveness to Copper from Petroleum Products by Copper Strip Test was applied to determine the oxidation condition of gasoline in the presence of sulfur contamination. In this study ASTM D130 and D525 was performed to determine the oxidation properties of gasoline sample in the presence of air, moisture and additives. Scanning Electron Microscopy (SEM) imaging techniques were used to compare the rust formed in the Cu-strips during the oxidation process.

Keywords: Copper corrosion, gum formation, gasoline, oxidation

1. Introduction

Crude petroleum oil needs to go under variety of testing before being used in the market since the oxidation properties of the petroleum products must be stable when used in internal combustion engines. Often times various organic molecules such as parafins, olefins and sulfur present in the crude petroleum products can initiate oxidation reaction that results in corrosion, gum formation in the heat-engines. These oxidation reactions can be caused by the sulfur, oxygen and other hydrocarbon molecules present in the petroleum oil. The sulfur compounds remaining in the petroleum products, some can have a corroding action on various metals [1]. The effect varies according to the presence of sulfur compounds present in the petroleum products. The Cu-strip corrosion test [1] is designed to test the relative degree of corrosivity of a petroleum product.

Petroleum products such as gasolines are unstable as they form gum upon aging in the presence of air, which is directly related to oxidation of gasoline. In previous studies [3], it was shown that the gum content correlates with the peroxide number of aged gasolines, indicating that gum formation takes place mainly by polymerization of peroxides. Oils that are used to lubricate equipment in the petroleum industry are hydrocarbon based which makes them susceptible to degradation in the presence of water. Oxidation results in the formation of polar compounds namely aldehydes, ketones, carboxylic acids and oxygenated polymers. The products after oxidation reaction are highly corrosive and results in formation of resin,
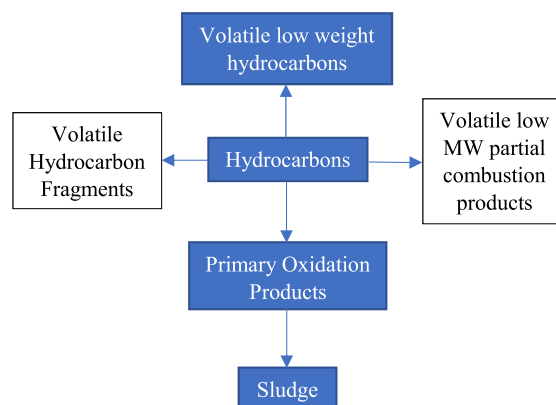

Figure 1: High temperature lubricant degradation model [2].

deposits, and sludge [2]. The presence of the by-products of degradation affects the proper functioning of the equipment. The deposits produced in the oxidation consists of materials of much higher molecular weight mixed with water, oil, and other contaminants [3, 4]. During the oxidation process, oxygen in the system readily reacts with labile hydrogens of the hydrocarbon structures that make up the lubricant. The oxidation of the hydrocarbons proceeds in three stages-initiation, propagation and termination. During the initiation stage, oxygen reacts with the fuel and lubricant forming alkyl radicals. During the propagation stage, these radicals react with oxygen and the lubricant to form peroxy radicals and hydroperoxides.

Hydroperoxides are mostly accumulated during the induction period after which autoacceleration of oxidation occurs (figure 2). The induction period in this case is used as an indication of the tendency of motor gasoline to form gum in storage [5].

This research focuses on applying ASTM test method ASTM D525 Standard Test Method for oxidation stability of gasoline (Induction Period Method) and ASTM D130 Standard Test Method for Corrosiveness to Copper from Petroleum Products by Copper Strip Test to evaluate the oxidative properties of automotive gasoline. ASTM D130 consists of immersing the Cu-strips in gasoline, maintaining the strip at 50°C in a bath. However, in this experiment we have used 100°C in the test bath and water as the heating media to see if the increase in temperature affects the oxidation process profoundly. The test was run for 5 hours instead of 3 hours for further investigation.

ASTM D525 was also applied to determine the oxidation stability of petroleum products specifically gasoline and improving the oxidation stability of gasoline by improving the additive levels, varying temperature and pressure, and applying catalysts. Following the Ideal gas law:

$$PV = nRT$$

for the reaction system, the induction period method of ASTM D525 was applied. Initially the system has free oxygen and this amount is fixed. As the oxidation occurs in the system the moles of oxygen decrease that results in the pressure drop. The system has excess amount of stoichiometric amount of oxygen (not equimolar) that continuous the free radical reaction of hydrocarbons forming different kinds of hydrocarbon products in the system.
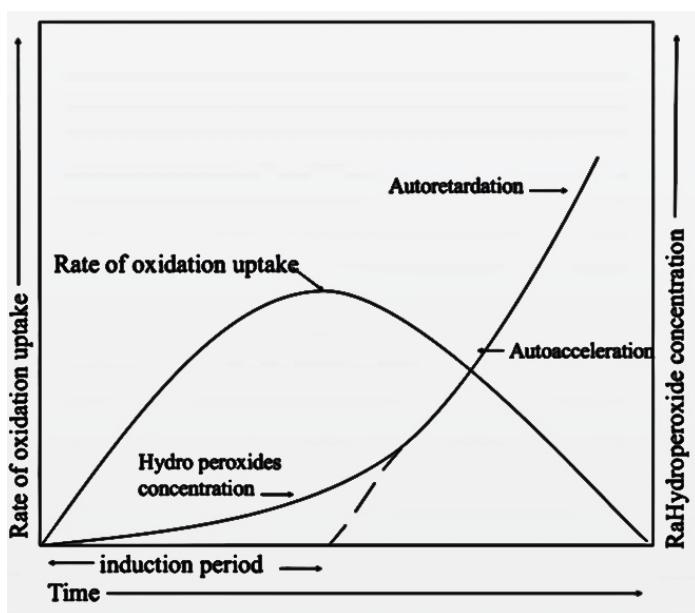

Figure 2: Effect of hydroperoxide concentration on the rate of oxidation [2].

One of the major problem that arises using ASTM D130 method is visual errors as the test results entirely depends on the testers subjectivity and high experience. Since Cu-strip corrosion originated by sulfur compounds in the petroleum gasoline causes very thin oxidation layers, often only a few micrometers (μm) thick, it is important to analyze the surface of the Cu-strips using surface analysis and micro-analysis methods. In this study, electron microscopy (SEM) technique was used to test the corrosion level on the strips.

2. Experimental

2.1. Materials

2.1.1. Gasoline
Briggs @ Stratton gasoline fuel can
Octane rate 87

2.1.2. Fuel Additive
Motor Medic Lead Substitute which was manufactured by RSC Chemical Solutions (part No. M5012) [6].

Table 1: Composition of Fuel Additive

Chemical Name	CAS Number	%
Petroleum Distillate Aliphatic	68476-34-6	80-90
Kerosene Hydrodesulfurized	64742-81-0	3-5
Naphthalene	91-20-3	<0.3
Other components below reportable level		10-20

2.1.3. Copper Strips Specification
Use strips that are 12.5 6 2-mm (1/2-in.) wide, 1.5 to 3.2-mm (1/16 to 1/8-in) thick and cut 75 6 5-mm (3-in) long from smooth-surfaced, hard-temper, cold-finished copper of 99.9%+ purity; electrical bus bar stock is generally suitable (see Annex A1). The strips may be used repeatedly but shall be discarded when the strips surface shows pitting or deep scratches that cannot be removed by the specified polishing procedure, or when the surface becomes deformed, or the dimensions for the copper strip fall outside the specified limits [1].

Figure 3: Copper Strip (Dimension 12.5mm X 1.5mm X 75.6mm)

Table 2: Copper Strip Classifications

Classification	Designation	Description
1	slight tarnish	a. Light orange, almost same as freshly polished strip b. Dark orange
2	moderate tarnish	a. Claret red b. Lavender c. Multicolored with lavender blue or silver, or both, overlaid on claret red d. Silvery e. Brassy or gold
3	dark tarnish	a. Magenta overcast on brassy strip b. Multicolored with red and green showing, but no gray
4	corrosion	a. Transparent black, dark gray or brown with peacock green barely showing b. Graphite or lustless black c. Glossy or jet black

2.1.4. Wash Solvent

Trimethylpentane (isooctane) of minimum 99.75% purity from Fisher Chemical. LOT 173733 [1].

2.1.5. Distilled Water

Laboratory reagent grade distilled water from Research Products International. LOT 48366-48873.

2.1.6. Surface preparation/Polishing Materials

Silicon carbide paper 220 grit FEPA grade Koehler Instrument Inc. 380-220-001.

Silicon carbide grain 150 grit FEPA grade Koehler Instrument Inc. 380-150-003 [1].

2.1.7. Oxygen

Commercially-available extra-dry oxygen of not less than 99.6% purity [5].

2.1.8. Hydrogen Sulfide Water Solution

LabChem LC154701 Water 99.6%, Hydrogen Sulfide 0.4% [7].

2.2. Experimental Methods

2.2.1. Standard Test Method for Corrosiveness to Copper from Petroleum Products by Copper Strip Test (ASTM D130)

This test method covers the determination of the corrosiveness to copper of automotive gasoline. A polished copper strip is immersed in a specific volume of the sample being tested and heated under conditions of temperature and time that are specific to the class of material being tested. At the end of the heating period, the copper strip is removed, washed, weighed and the color and tarnish level assessed against the ASTM Copper Strip Corrosion Standard.

Remove all surface blemishes from all six sides of the strip, with the 65-m (220-grit CAMI-grade or P220 FEPA-grade) silicon carbide paper or cloth, removing all marks.

Polish with the 105-m (120-grit to 150-grit CAMI-grade or P120 to P150 FEPA grade) silicon carbide grains.

Place 30 mL of sample in dry test tube and slide in the copper strip into the sample tube. Place the sample tube into the pressure vessel and screw the lid on tightly. Put in the pressure vessel in 100 ± 1 °C and for 5h ± 5 min.

Empty the contents of the test tube and withdraw the strip with forceps and immerse in wash solvent, trimethylpentane (isooctane) of minimum 99.75% purity. Dry and inspect for evidence of tarnishing or corrosion by comparison with the Copper Strip Corrosion Standards.

Figure 4: Test Bath Unit for ASTM D130.

2.2.2. Standard Test Method for oxidation stability of gasoline (Induction Period Method, ASTM D525)

This test method covers the determination of the stability of gasoline under accelerated oxidation conditions.

The sample is oxidized in a pressure vessel initially filled at 15 to 25°C with oxygen pressure to 690 to 705 kPa and heated at a temperature between 98 to 102°C. The pressure is recorded at stated intervals until the breakpoint is reached. The time required for the sample to reach this point is the observed induction period at the temperature of test, from which the induction period at 100°C can be calculated.

Figure 5: Test Bath Unit and Pressure Vessel for ASTM D525.

2.3. Analytical Methods

2.3.1. Scanning Electron Microscope (SEM)

Scanning Electron Microscopy was carried out using a LEO-1550 Gemini microscope.

3. Results and Discussion

3.1. Analysis of the test strips

3.1.1. Cu-Strip Characterization

Table 3: List of Samples

Sample ID	Contents
A	Gasoline 87
B	Gasoline 87 + 0.1% of Fuel Additive
C	Gasoline 87 + 0.1% of Water
D	Gasoline 87 (Aged for 6 months)
E	Gasoline 87 + Hydrogen Sulfide Water Solution
F	Gasoline 87 + Hydrogen Sulfide Water Solution + Fuel Additive

The results of the ASTM D130 copper strip test are shown in Figure 7. Specimen A, which is pure gasoline, is light orange in color, similar to a freshly polished strip
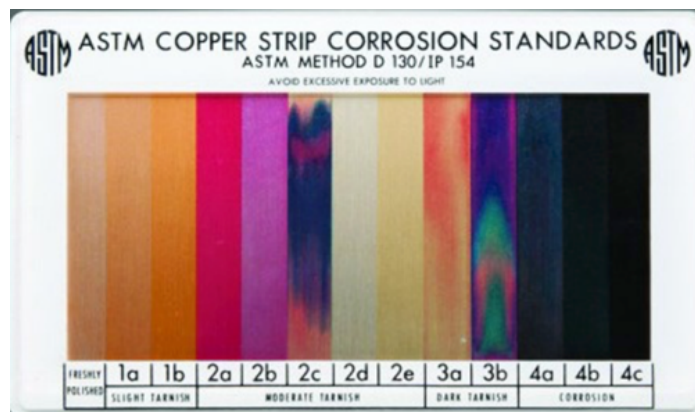

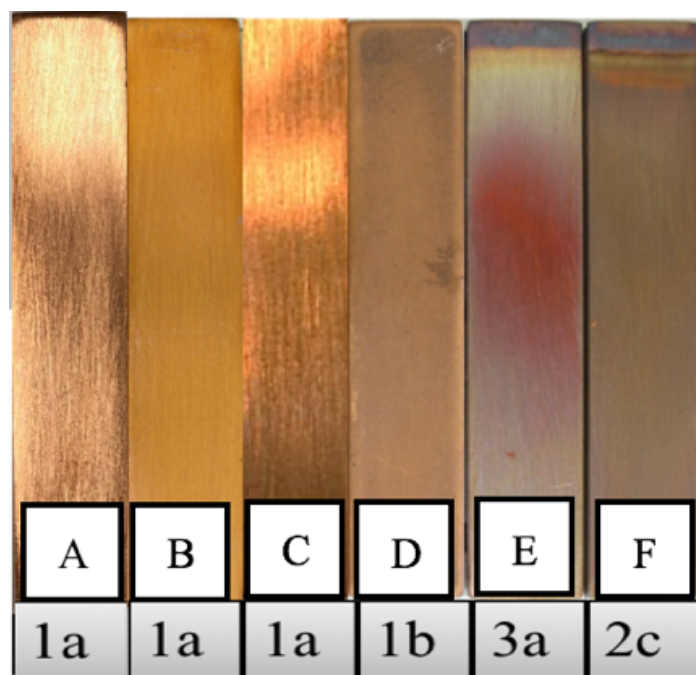Figure 6: ASTM D130 Corrosion standard for Copper strip.

Figure 7: Cu strip after D130 test in modified condition.

(Table 2). Following figure 6, Sample A it can be categorized into 1a group. Similarly, Sample B & C falls on to the same group 1a category as well. According ASTM D130 when a strip is in the obvious transition state between that indicated by any two adjacent strips, the strips should be rated into more tarnished category. Thus, Sample D can be identified as 1b (Table 2). Sample E shows magenta overcast on brassy strip making it fall under 3a category. In order to distinguish between group 3a and 2a, the strip was immersed into iso-octane solvent as mentioned in section 12.1.1 in ASTM D130 method. The strip didnt change its appearance; therefore, it falls into 3a category. The results can be interpreted using the following formula mentioned in ASTM D130:
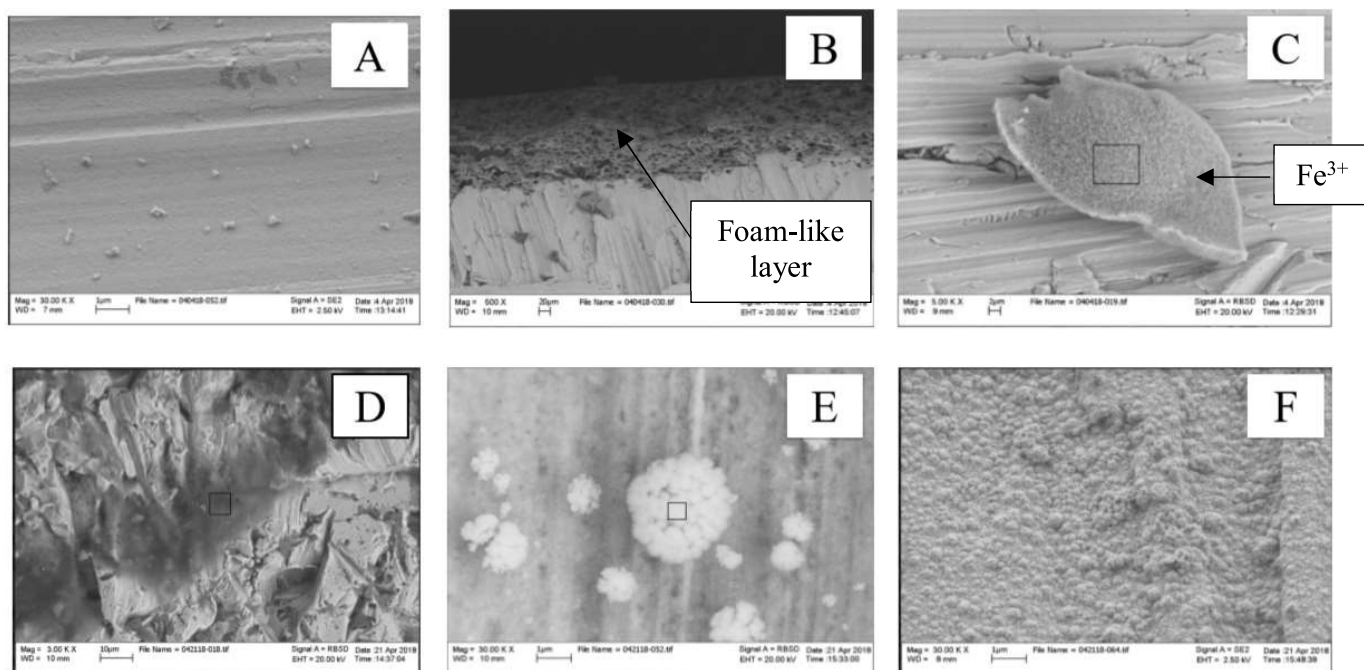
Figure 8: Scanning Electron Microscopy Images of Samples; (A) Surface of Cu-strip sample immersed in gasoline; (B) Cu-strip surface immersed in gasoline + fuel additive builds up passivation layer; (C) Traces of Fe^{3+} on the surface of Cu-strip after being exposed in gasoline and water mixture; (D) Cu-strip surface immersed in aged gasoline shows formation of salt rings; (E) Formation of salt particles on the Cu-strip surface as result of oxidation reaction in the gasoline + H_2S solution; (F) Accumulation of salt particles on the Cu-strip surface as result of oxidation reaction in the gasoline + H_2S solution + fuel additive.

$$Corrosion\ copper\ strip\left(\frac{Xh}{Y°C}\right),\ Classification\ Zp \quad (1)$$

Where,

$X = test\ duration,\ in\ hours$

$Y = test\ temperature,\ °C$

$Z = classification\ category\ (i.e.\ 1,\ 2,\ 3,\ 4)$

$p = classification\ description\ for\ the\ corresponding\ Z$
$\quad (i.e.\ a,\ b)$

Following the same format, the results are following:

  i Corrosion Sample A (5h/100°C), Classification 1a
 ii Corrosion Sample B (5h/100°C), Classification 1a
iii Corrosion Sample C (5h/100°C), Classification 1a
 iv Corrosion Sample D (5h/100°C), Classification 1b
  v Corrosion Sample A (5h/100°C), Classification 3a
 vi Corrosion Sample A (5h/100°C), Classification 2c

3.1.2. Scanning Electron Microscope (SEM)

In order to examine the surface of the Cu-strips, SEM imaging were taken. The SEM imaging shows variance in surface behavior.

The Images from Figure 8 are SEM images of Samples. Figure 8A shows smooth copper surface after the heating period. There were not any traces of significant oxidation reaction on the surface. Figure 8B shows accumulation of foam-like passivation layer. The foam-like passivation layer is further example of etching. Etching is a major problem since it can weaken the metal and accelerate wear. This type of additive can be worse than corrosion since it causes surface loss. The active ingredient in the fuel additive are proprietary secrets and their composition is unknown. However, this suggests that the use of this type of additive is not recommended with metals. Figure 8C demonstrates the effect of oxidation reaction in the presence of polar protic solvents such as water (H_2O). Water plays a vital role in the corrosion of metal alloys. The EDS spectra in Figure 9C shows traces of Iron (Fe) on the surface. In the case of aged gasoline Sample D the SEM image Figure 8D shows formation of salt-ring on the surface of the metal. The EDS data in Figure 9D also shows traces of metallic salt particles. This degradation is caused due to the presence of sulfur in the aged gasoline. As the gasoline was about 6+ months old, the sulfur in the gasoline started to initiate oxidation reaction under high temperature condition used in D130 method.

Figure 8E shows sample immersed in H_2S solution (10% H_2S). Theoretically, the presence of H_2S is highly corrosive for petroleum products such as gasoline [8]. It reacts with the Cu surface in the following way:
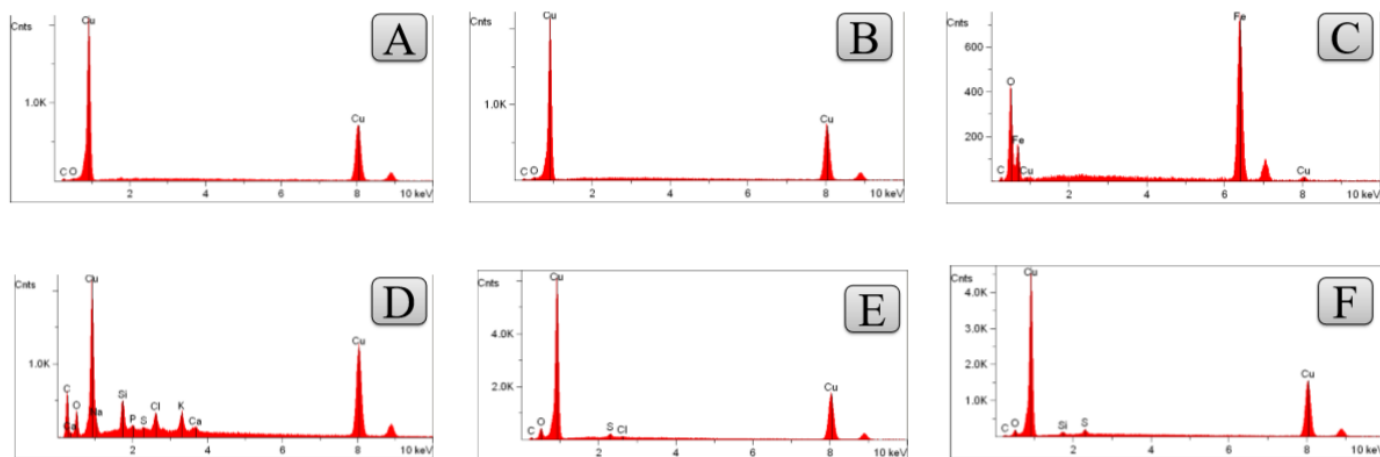
Figure 9: Energy Dissipative X-ray Spectroscopy (EDS) of Samples; (A) Cu-strip surface immersed in gasoline; (B) EDS of Cu-strip immersed in gasoline + fuel additive doesnt show any molecules other than Cu itself; (C) Presence of FeO formation on the Cu-strip surface; (D) Traces of several salt is detected due to contamination; (E) & (F) EDS do not show any salt traces, this could be related to Sulfurs small cross section area which is not detectable by EDS.

$$Cu_{(s)} + H_2S + \frac{1}{2}O_{2_{(g)}} = CuS_s + H_2O_{(l)} \qquad (2)$$
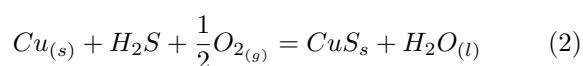
The equation (2) reaction [8] creates accumulation of metallic salt on the surface of Cu strip. Such precipitation can lead to the degradation of metals in automotive engine parts. For Sample 8F, gasoline was mixed with H_2S and fuel additive (Section 2.1.2) to demonstrate if addition of corrosion inhibitor would decelerate the oxidation process in gasoline. Even though the SEM image shows salt precipitates on the surface of Cu-strips, the EDS images could not identify the layer since sulfur has small very small cross section area which is harder to detect using EDS. Further testing is needed to demonstrate the theory.
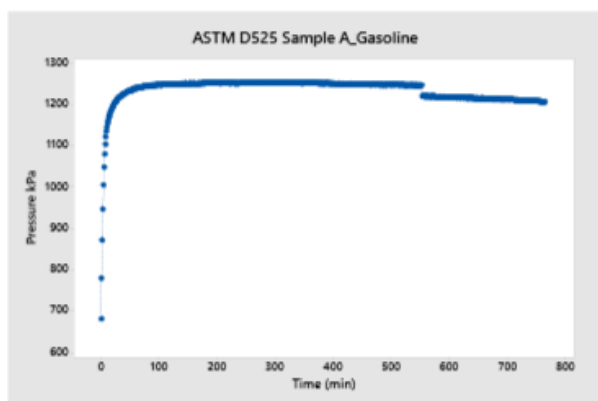
3.2. Analysis of the Gum Formation

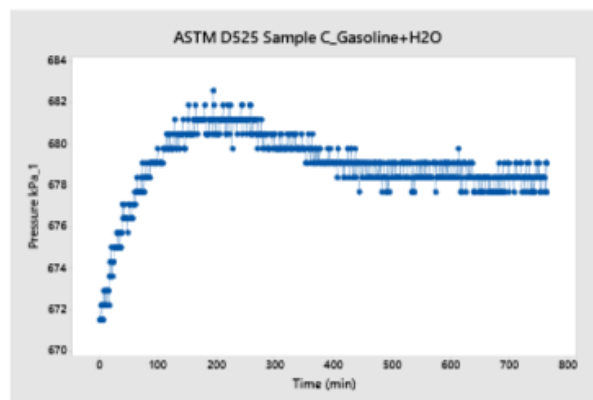Figure 10: ASTM D525 pressure vs time graph demonstrating the induction period of Sample C.

Figure 11: ASTM D525 pressure vs time graph demonstrating the induction period of Sample C.
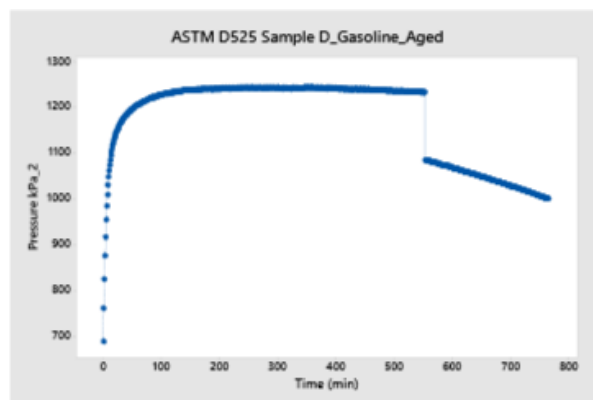

Figure 12: ASTM D525 pressure vs time graph demonstrating the induction period of Sample D.

In order to test the oxidation condition of gasoline, ASTM D525 was applied in the same batch of gasoline used for copper corrosion. The induction period in this method is used to indicate the formation of gum by motor

71

gasoline. Sample 8C (0.1% water + gasoline) and Sample 8B (aged gasoline) were also tested to examine the correlation between different condition of gasoline. For Sample A, Gasoline and Sample D, Gasoline aged, the induction period is almost in the same range. The break point in both samples occur at 1249 kPa. Since the motor gasoline that were tested in this case were from the same marketable source, they were expected to have similar and good oxidation stability in general. However, for Sample C_Gasoline+H$_2$O, the oxidation condition was highly unstable even before the heating period mentioned in ASTM D525 method. The presence of polar solvent accelerates the oxidation by forming hydroperoxides in the system. Therefore, the system has continuous pressure change. Since the system was already very unstable, the sample wasnt heated under accelerated condition as a safety measure in the lab.

4. Conclusion

The corrosiveness and oxidation stability of gasoline mixtures containing water and fuel additives was examined via ASTM D525 and D130 standard test methods. The effect was significant for the samples containing higher percentage of sulfur. In fact, sulfur corrosion has been a long existent problem in the petroleum industry. Addition of corrosion inhibitor in the presence of sulfur was not effective in the case of Sample F. Further test analysis is needed to observe the effect of corrosion inhibitor on Cu-strips. Addition of water as polar solvent accelerates the corrosion rate as seen in Sample C. Presence of water also initiates the hydro peroxide formation in the system in the case of D525 test. Therefore, traces of polar solvents and organic molecules in the motor gasoline can have negative effect on the fuel performance. Additionally, the current D130 method should be modified to avoid human error since the results completely depend on the observers judgment and experience.

5. Acknowledgements

6. References

[1] ASTM D130-12. Standard test method for corrosiveness to copper from petroleum products by copper strip test. Technical report, ASTM International, 2012.

[2] George Totten, S Westbrook, and R Shah. Fuels and lubricants handbook: Technology, properties, performance, and testing. Jan 2003.

[3] V. Voorhees and John O. Eisinger. The effect of gum in gasoline. 1929.

[4] Florian Pradelle, Sergio L. Braga, Ana Rosa F. A. Martins, Franck Turkovics, and Renata N. C. Pradelle. Gum formation in gasoline and its blends: A review. *Energy & Fuels*, 29(12):77537770, 2015.

[5] ASTM D525-12a. Standard test method for oxidation stability of gasoline (induction period method). Technical report, ASTM International, 2012.

[6] Motor Medic Lead Substitute. *MSDS No. M5012*. RSC Chemical Solutions: Indian Trial, NC, Jun 2016. (Accessed 21 Apr 2018).

[7] Hydrogen Sulfide Water. *MSDS No. LC15470*. LabChem: Jackson Township, PA, Oct 2017. (Accessed 21 Apr 2018).

[8] William Henry Brown, Brent L. Iverson, Eric V. Anslyn, and Christopher S. Foote. *Organic chemistry*. Wadsworth Cengage Learning, 2014.